Thermal Storage and Transport in Colloidal Nanocrystal-Based Materials

by

Minglu Liu

A Dissertation Presented in Partial Fulfillment
of the Requirements for the Degree
Doctor of Philosophy

Approved November 2015 by the
Graduate Supervisory Committee:

Robert Wang, Chair
Liping Wang
Konrad Rykaczewski
Patrick Phelan
Lenore Dai

ARIZONA STATE UNIVERSITY

December 2015

ABSTRACT

The rapid progress of solution-phase synthesis has led colloidal nanocrystals one of the most versatile nanoscale materials, provided opportunities to tailor material's properties, and boosted related technological innovations. Colloidal nanocrystal-based materials have been demonstrated success in a variety of applications, such as LEDs, electronics, solar cells and thermoelectrics. In each of these applications, the thermal transport property plays a big role. An undesirable temperature rise due to inefficient heat dissipation could lead to deleterious effects on devices' performance and lifetime. Hence, the first project is focused on investigating the thermal transport in colloidal nanocrystal solids. This study answers the question that how the molecular structure of nanocrystals affect the thermal transport, and provides insights for future device designs. In particular, PbS nanocrystals is used as a monitoring system, and the core diameter, ligand length and ligand binding group are systematically varied to study the corresponding effect on thermal transport.

Next, a fundamental study is presented on the phase stability and solid-liquid transformation of metallic (In, Sn and Bi) colloidal nanocrystals. Although the phase change of nanoparticles has been a long-standing research topic, the melting behavior of colloidal nanocrytstals is largely unexplored. In addition, this study is of practical importance to nanocrystal-based applications that operate at elevated temperatures. Embedding colloidal nanocrystals into thermally-stable polymer matrices allows preserving nanocrystal size throughout melt-freeze cycles, and therefore enabling observation of stable melting features. Size-dependent melting temperature, melting enthalpy and melting entropy have all been measured and discussed.

In the next two chapters, focus has been switched to developing colloidal nanocrystal-based phase change composites for thermal energy storage applications. In Chapter 4, a polymer matrix phase change nanocomposite has been created. In this composite, the melting temperature and energy density could be independently controlled by tuning nanocrystal diameter and volume fractions. In Chapter 5, a solution-phase synthesis on metal matrix-metal nanocrytal composite is presented. This approach enables excellent morphological control over nanocrystals and demonstrated a phase change composite with a thermal conductivity 2 - 3 orders of magnitude greater than typical phase change materials, such as organics and molten salts.

Dedicated to

my father Zhi Liu, my mother Xiaohui Wu

and my wife Xin Guan

ACKNOWLEDGMENTS

During the past four and half years, I have been very fortunate to work with many researchers at ASU. Without their support and help, it would be impossible for me to complete this dissertation. So, I would like to express my thanks to all of them.

First and foremost, I would like to acknowledge my research advisor, Robert Wang, for choosing me as his first Ph.D. student and offering me the opportunity to work in his lab. Throughout my Ph.D., Robert has been an excellent advisor, who not only inspired me with his insights and creativity on big pictures, but also taught me how to be a researcher. From him, I learned how to write clearly, how to present professionally, and how to behave like an experimentalist in the lab. His passion, optimism and diligence will influence me forever in my life.

I would also like to thank all my committee members for their kind help and constructive suggestions on my research: Prof. Patrick Phelan built my basic understanding in nanoscale heat transfer; Prof. Lenore Dai gave me insightful suggestions on my first project; Prof. Liping Wang shared his knowledge in radiative heat transfer with me; and Prof. Konrad Rykaczewski helped to review my manuscript.

Next, I'd like to thank all my collaborators in this lab, I thank Yuanyu for her help on a couple of my projects, and her feedbacks on my experiments; Abbas helped to build up the 3 omega station that I used for thermal conductivity measurements; Hsinwei helped me with transmission electron microscopy. I also thank all other members in Robert's group, Seid, Xiying, Andre, Kyle, Jason, Leah and Prathamesh. Also, I'd like to thank the

staff in CSSS and CSSER at ASU. They are all kind, patient and ready to help: Karl, Kenneth, Diana, Emmanuel, Barry, Carrie and Todd.

Lastly, I want to thank my farther Zhi Liu, my mother Xiaohui Wu and my wife Xin Guan. I am forever indebted to my parents, who have given me their deepest and endless love, support, and guidance. For the past four years, Xin has given me her love, support and understanding, for which I really appreciate.

TABLE OF CONTENTS

Page

CHAPTER

CHAPTER Page

LIST OF TABLES

Table Page

LIST OF FIGURES

Figure Page

Figure Page

CHAPTER 1

INTRODUCTION AND BACKGROUND

1.1 Colloidal Nanocrystals

Colloidal nanocrystals is an important class of nanomaterials that draws tremendous attention in the recent 30 years, starting with pioneering work by Brus et al,.[1, 2] Since then, relentless efforts have been devoted into modifying the synthesis, studying the properties and integrating them into devices.[3-12] Until now, successful nanocrystal synthesis have been demonstrated on a variety of compositions, such as metals, metal oxide, and semiconductors. Excellent morphological control over nanocrystal's size and shape have also been demonstrated.[6, 10, 11] In-situ techniques have been developed to visualize the growth of nanocrystals.[13, 14] Tons of nanocrystals have been produced for ultra-LED screen with enhanced displaying properties(Figure 1b). Consequently, colloidal nanocrysals is considered one of the most versatile nanoscale materials.

Colloidal nanocrystals consists of an inorganic core and organic ligands bound to its surface. The larger surface area and quantum confinement from the nanocrystal core is of both interest for fundamental studies and applications. The surface ligand plays a big role in controlling the nanocrystal's morphology during synthesis, passivating the high-energy surfaces and imparting them with solubility. The solubility of colloidal nanocrysals again supports low-cost solution-phase processing, allows deposition onto arbitrary substrates and embedding into various matrices. Based on this, solution-processed LEDs,[15, 16] photovoltaics,[17, 18] and electronics[19, 20] have all been reported.

The optical properties was firstly thoroughly studied on semiconductor colloidal nanocrystals (quantum dots). The quantum confinement of nanocrystal yields a tunable bandgap, which could be used to produce luminescence covering the entire visible spectrum.[21] Surface chemistry later has been found important to affect nanoparticle's transport properties and energy conversion efficiencies.[22-28] For example, it was found that the charge transport in nanocrystal solids could be greatly improved by replacing the native organic ligands with ligands that have compact structures.[29] A variety of short organic ligands, inorganic ligands have then been developed and applied to facilitate efficient electron transport.

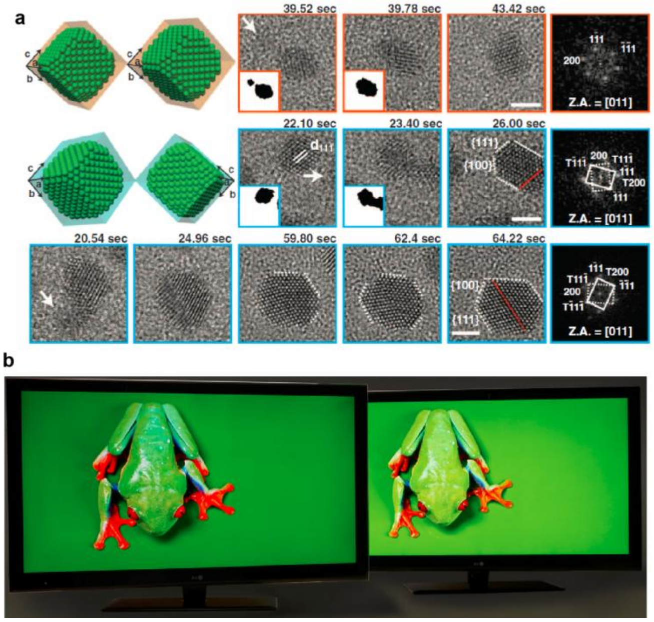

Figure 1.1 (a) In-situ observation of colloidal Pt nanocrytal growth using transmission electron microscopy [Ref 14], Ultra-LED display that exhibits enhanced brightness and sharpness using quantum dots technology.

1.2 Fundamentals of thermal transport

Heat in solids is conducted by diffusion of energy carriers. There are two types of carriers that participate in thermal transport, i.e., free electrons and phonons. In metallic materials, heat is predominantly conducted by electrons due to the large free electron density. In dielectrics and moderate doped semiconductors, heat is conducted primarily by lattice waves, which has quantized energy and momentum, and could be depicted using a phonon picture. Since this work will discuss the thermal transport in both metallic composites and semiconductor nanocrystal thin films, brief introductions of both electrons and phonons are given .

1.2.1 Phonons

Lattice waves and phonons

In a crystalline solid, atoms are connected together via chemical bonds in a periodic manner. At 0 K, all atoms freeze at the equilibrium position with no atomic vibrations. At a non-zero temperature, atoms start to vibrate and displace from the equilibrium position due to thermal energy. This energy, scales as $k_B T$, leads to thermal transport throughout the solid. The motion of atoms in solids could be described using a spring-mass system with atomic mass M, spring constant K and inter-atomic space A (Figure 1.2). A one-dimensional lattice model is often used to understand this process and it turns out the classical wave equation could be applied to described the lattice waves with minor modification:

$$\mathrm{M}\frac{\partial^2 \mathrm{u}}{\partial \mathrm{t}^2} = \mathrm{K}\mathrm{A}^2\frac{\partial^2 \mathrm{u}}{\partial \mathrm{x}^2}$$

Solve this equation, we can obtain the dispersion relation, which decribes the relation between the wavevector and frequency: (Figure 1.2)

$$\omega = 2\sqrt{\frac{K}{M}}\left|\sin\frac{kA}{2}\right|$$

Note that the wavevector k here is not arbitrary and it has to satisfy two requirements: 1). The largest allowable wavevector is $\frac{2\pi}{A}$, which limited by the inter-atomic distance. Because any wavevector larger than $\frac{2\pi}{A}$ will lead to a wavelength smaller than A, which is not physically meaningful for a real crystal;. 2). The smallest wavevector is $k = \frac{2\pi}{L}$ that limited by the dimension of the crystal, and the smallest increment of k is also $\frac{2\pi}{L}$.

$$k = \frac{2\pi n}{L} \text{ (n = 0, 1, 2, 3...)}$$

The dispersion relation is of great importance because it provides all the allowable vibration modes in the lattice. However, this treatment based on classical mechanics will give an incorrect answer to the energy of each oscillator. From quantum mechanics, if we solve Schrodinger equation, we will obtain the exact same formula of dispersion relation but with quantized oscillator energy.

$$E_n = h\upsilon\left(n + \frac{1}{2}\right) \text{ (n = 0, 1, 2, 3...)}$$

The energy quanta of lattice vibrations $h\upsilon$ has been named as phonon, which is a concept parallel to the quantized energy of electromagnetic waves - photon. This treatment significantly simplifies the transport picture, instead of considering all the wave propagation in a solid, we can then consider phonon particles travelling in a box.

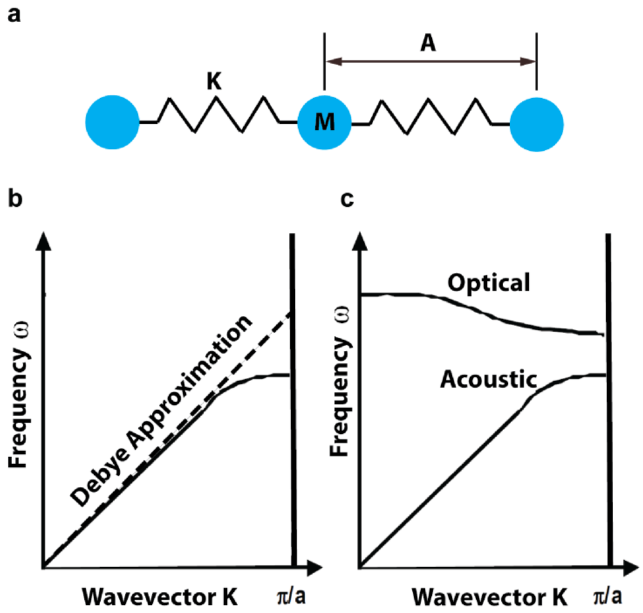

Figure 1.2 (a) Schematic of 1-dimensional mass-spring system with atomic mass M, spring constant K and interatomic distance A, Phonon dispersion of (b) mono-atomic chain and (c) diatomic chain.

Phonon branches and polarizations

In a lattice basis that consists of two types of atoms (different mass, different spring constant or different distances), there will be in-phase vibration modes (acoustic branch) and out of phase vibration modes (optical branch) as shown in Figure 1.2 (c). The optical phonons in general have higher energies but their contribution to thermal transport is very limited because of the low speed. The speed of phonon is determined by the group velocity, v_g.

$$v_g = d\omega/dk$$

As we can see, the acoustic branch of phonons have a larger slope (v_g), and hence dominates thermal transport. The optical phonons although have greater energies, its group velocity is small and leads to negligible contribution to thermal transport.

In one-dimensional atomic chain, atoms can only vibrate in the longitudinal direction, where the atomic displacement is same as wave propagation, hence only one longitudinal branch exist. In a three-dimensional crystal, the atoms can also displace in two directions that perpendicular to the wave propagation, hence there are two more transverse branches in typical band diagrams.

Density of states and Debye approximation

At each energy level, there can be more than one corresponding wavevector, which lead to degenerate phonons. A concept of density of states (DOS) is created to represent the energy degeneracy. We note that this concept is not unique for phonons but broadly used for other particles, such as photons and electrons. To obtain the DOS of phonons, we count how many phonon modes exist in a given *k* space. For example, in a three-dimensional cubic crystal with L as the length, the number of phonon modes within a sphere in *k* space is:

$$\mathrm{N} = \frac{\frac{4}{3}\pi \mathrm{k}^3}{(2\pi/\mathrm{L})^3}$$

The DOS of phonons *D(ω)* is defined as:

$$D(\omega) = \frac{dN}{d\omega} = \frac{dN}{dk}\frac{dk}{d\omega}$$

where we need to specify the relation between wavevector k and frequency ω. For acoustic phonons, Debye approximation is always used, which assumes a linear relationship between k and ω, i.e., $\omega = v_g k$, where v_g is the group velocity of phonons in the long wavelength limit (speed of sound). Hence, the DOS could then be represented as:

$$D(\omega) = \frac{4\pi(\omega/v_g)^2}{(2\pi/\mathrm{L})^3 v_g} = \frac{\omega^2 \mathrm{L}^3}{2\pi^2 v_g^3}$$

If we consider the per volume basis DOS and 3 polarizations of phonons, the DOS will be:

$$D(\omega) = \frac{3\,\frac{\omega^2 \mathrm{L}^3}{2\pi^2 v_g^3}}{\mathrm{L}^3} = \frac{3\omega^2}{2\pi^2 v_g^3}$$

We note that Debye approximation gives a reasonable estimation of acoustic phonons with small wavevectors, it overestimates the velocity close to the Brillion zone boundary. Also, it is not appropriate for optical phonons, which could be estimated using Einstein model.

Bose-Einstein distribution and Fermi-Dirac distribution

The DOS of phonons provides all the allowable energy states in materials, however it tells nothing about which and how many phonons will present at a given temperature. This question could be answered by statistical thermodynamics. According to statistical thermodynamics, phonons and photons are obeying the same distribution, i.e. Bose-Einstein distribution, and they are bosons.

$$\langle n \rangle = f(\omega) = \frac{1}{\exp\left(\frac{\hbar\omega}{k_B T}\right) - 1}$$

Electron on the other hand, obeys a different distribution, i.e. Fermi-Dirac distribution and thereby is a fermion. It only changes a sign in the denominator, but in fact, this is one of the fundamental differences between electrons and phonons.

$$\langle n \rangle = f(\omega) = \frac{1}{\exp\left(\frac{\hbar\omega}{k_B T}\right) + 1}$$

A simple picture could be used to illustrate these two distributions: Fermi-Dirac distribution is like a tall but narrow bottle, whereas Bose-Einstein distribution is like a big but shallow plate. When you fill electrons into the narrow bottle, only two electrons are allowed at the same height, i.e. the same energy level. In contrast, the big plate (Bose-Einstein distribution) allows many phonons filled at the same energy level. This difference determines that only the electrons at the highest level (near the Fermi level) can participate in heat or charge transport, while all phonons make contributions to heat transport.

Specific heat and thermal conductivity

Until now, we have discussed phonon energy, allowable energy states and statistical distribution, hence we are able to calculate the total energy of all lattice vibrations, which is just a summation of phonons over all wavevectors and polarizations:

$$E = \sum_{K,p} \langle n_{K,p} + \frac{1}{2} \rangle \hbar \omega$$

For bulk crystals, the discretization in K space is very small, and we can replace the summation with a integration.

$$E = \sum_{p} \int \langle n_{K,p} + \frac{1}{2} \rangle \hbar \omega \, D(\omega) d\omega$$

We then applied Debye approximation and take derivative with respect to temperature T to get phonon specific heat C_p, where the Debye frequency ω_D represents the cutoff frequency of phonons in solids.

$$C_p = \frac{dE}{dT} = \frac{3\hbar^2}{2\pi^2 v_g^3 k_B T^2} \int_0^{\omega_D} d\omega \frac{\omega^4 \exp\left(\frac{\hbar}{k_B T}\right)}{\left[\exp\left(\frac{\hbar\omega}{k_B T}\right) - 1\right]^2}$$

At low temperatures, this formula could be further simplified as following form:

$$C_p = \frac{36\pi^2 k_B}{15} \left(\frac{N}{V}\right) \left(\frac{T}{\theta_D}\right)^3$$

which says the phonon specific heat scales as T^3 at temperature lower than Debye temperature θ_D. The Debye temperature is the temperature that all phonons are excited in the solid, and can be related to Debye frequency as:

$$\theta_D = \frac{\hbar \omega_D}{k_B}$$

We have now established the formula of phonon specific heat C_p, and the phonon thermal conductivity k_p could be represented as $k_p = \frac{1}{3} C_p v_g l$ using kinetic theory. This simple form, originally used to describe the thermal conductivity of gas molecules is valid to predict the thermal conductivity of both electrons and phonons. This formula could also be derived directly from solving Boltzman transport equation (BTE) with relaxation time approximation. The mean free path *l* is an important concept that represent the average traveling distance of phonons between two scattering events.

Phonon scattering

In a perfect crystal with only harmonic interatomic potential, all lattice waves can be decomposed into normal modes and propagate without interaction. In this case, there is no resistance to thermal energy transport, which would lead to a infinite thermal conductivity. However, phonons in a real crystal are encountering all types of scatterings during transport, which leads to a finite thermal conductivity. The occurrence of phonon scattering could be roughly categorized into two reasons: a. The imperfections of crystals, including defects, impurities, and grain boundaries. These structural features in real crystals will lead to changes of mass and/or spring constant in the system, hence induces disturbance on phonon transport. b. The anharmonic interatomic potential. The harmonic assumption of interatomic potential is only true near the equilibrium point, where the displacements are small. As temperature increases, the atomic vibration intensifies, at which point anharmonic terms comes in. This will result in phonon-phonon scatterings.

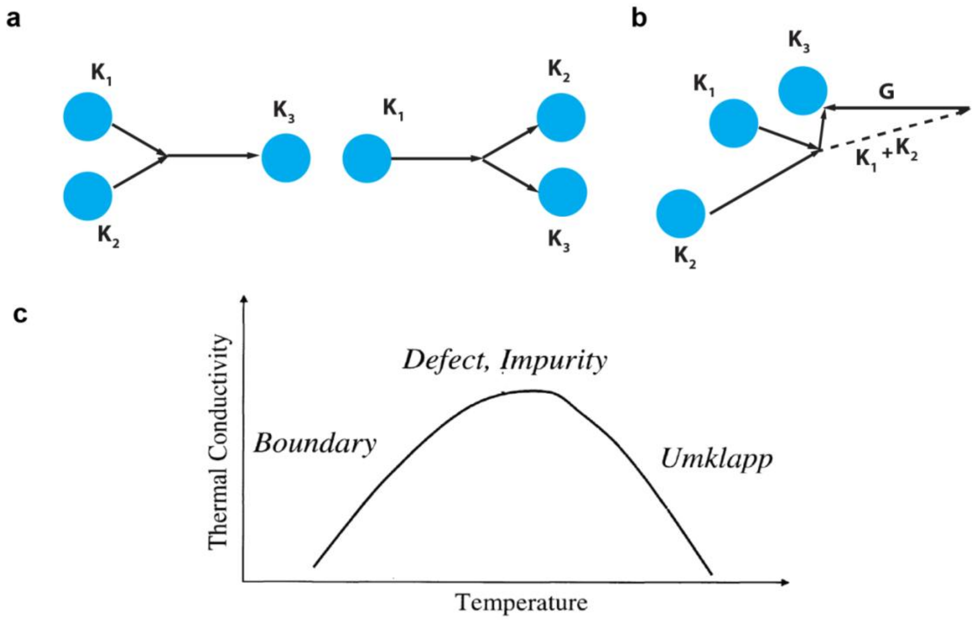

Figure 1.3 Illustration of different scattering mechanisms, (a) normal process, and (b) unclampp process. (c) Temperature-dependent thermal conductivity trend of a dielectric material and corresponding dominant scattering process at different temperatures.

Phonon-phonon scattering could be further classified into two categories: normal process (N process) and umclapp process (U process) The fundamental difference between these two mechanisms is: In N process, both energy and momentum are conserved, whereas in U process, momentum is no longer conservative. The U process is arising from the finite wavevector of lattice waves: For instance, the largest wavevector for a lattice wave is 2π/3a; If two lattice waves combines and each has a wavevector of π/2a, the produced lattice wave will have a wavevector of 7π/6a, which exceeds the wavevector limit and cannot exist. As a result, the third lattice wave lose some momentum and has a wavevector of π/6a. We note all the scattering mechanisms(defect, impurity, grain boundary and unclampp scattering) that cause momentum reduction will lead to resistance to thermal transport.

To consider all the different scattering mechanisms, Matthiessen rule is always used, which relates the overall relaxation time τ to the relaxation time of umclapp scattering, boundary scattering and impurity scattering. Relaxation time is the average time that phonon travels between two collisions, and mean free path l could be represented as $l = v_g\tau$ if we treat all phonons have the same velocity. [30]

$$\tau^{-1} = \tau_u^{-1} + \tau_b^{-1} + \tau_I^{-1}$$

$$\tau_u^{-1} = Be^{\frac{-\theta_D}{bT}}T^3\omega^2$$

$$\tau_I^{-1} = A\omega^4$$

$$\tau_b^{-1} = b_s\upsilon/L$$

We note that the relaxation time are all frequency dependent, and so does mean free path. Hence, we should modify the expression of thermal conductivity as:

$$k_p = \frac{1}{3}\int_0^{\omega_D} C(\omega)\, V_g(\omega) l(\omega)$$

In addition, among these scattering mechanisms, phonon-phonon scattering is a strong function of temperature, which indicates the thermal conductivity should also be a function of temperature. At low temperatures, low frequency phonons with long mean free path dominate thermal transport and phonons were majorly scattered by boundaries. At higher temperature, shorter wavelength phonons take it over, which is then scattered primarily by defects and impurities. As temperature increased to even higher, more phonons are "active", and umclapp scattering dominates. As a result, the thermal conductivity decreased with further increment in temperature due to the large number of phonon-phonon scattering.

1.2.2 Electrons

Electron is the primary heat carrier in metals but contributes very little to the thermal transport in dielectrics and semiconductors. This is dictated by its fermion nature, i.e. only the electrons closed to the Fermi level could participate in energy transport. Fermi level is the highest filled energy level at 0 K. In metals, the Fermi level is in the middle of conduction band, thereby a large population of electrons could participate in energy transport. For semiconductor and dielectrics however, the Fermi level locates in the bandgap between conduction band and valence band, which means there is no energy carrier at 0 K. The size of the bandgap determines if a solid is a semiconductor or a dielectric material. Semiconductor usually have a small bandgap, and some amount of electrons can be thermally excited as temperature increases and carry energy. Dielectric materials on the other hand have larger bandgaps, and hence there is negligible population of charge carriers even at room temperature.

Electronic thermal conductivity

Just like phonon thermal conductivity, the electronic thermal conductivity can be expressed as $k_{el} = \frac{1}{3} c_{el} v_{el} l_{el}$. Several comparisons of interest could be made here between phonon thermal conductivity and electric conductivity:

a) The specific heat of phonons and electrons are both a function of temperature. At low temperatures, phonon specific heat scales as T^3 and it will reach to a constant at Debye temperature as all modes of phonons have been excited. For electrons, it increases as T in the entire temperature range.

b) The velocity of free electrons is much greater than (2 - 3 orders of magnitude) the group velocity of phonons. The electron moves at a speed of ~ 10 e6 m/s, whereas the speed of sound is ~ 10 e3/s for most materials.

c) At room temperature, the electron mean free path is around 1e-8 m. For phonons, its mean free path also depends on frequency, but in general a good heat conductor should have a mean free path 2 - 3 orders of magnitude greater than that of electrons.

Electron Scattering

Electrons are predominantly scattered by phonons. That's why superconducting in general occurs at very low temperature, where not many phonons activated. The relaxation time of electron is inversely proportional to temperature, $\tau \sim T^{-1}$, and electronic thermal conductivity is 100 - 1000 times greater at low temperatures (<10 K) than that at room temperature.

Wiedemann-Franz law

Since electrons are both charge carriers and heat carriers in metals, it is a smart idea to compare the electrical conductivity and thermal conductivity of metals. Interestingly, it is found that the electrical conductivity σ and thermal conductivity k can be related by the famous Wiedemann-Franz law:

$$\frac{k}{\sigma} = LT$$

where L is called Lorenz number and it is a constant for most metals.

$$L = \frac{\pi^2}{3}\left(\frac{k_B}{e}\right)^2 = 2.44 \times 10^{-8}\ \mathrm{W\Omega K^{-2}}$$

This law presents the beauty of simplicity in science. In addition, it is practically useful to determine the thermal conductivity of metallic materials. Because the measurement of thermal conductivity is generally more complicated than measuring electrical conductivity.

1.2.3 Thermal transport in nanostructures

In nanostructures, thermal transport could be affected by classical size effect as well as quantum confinement. As the characteristic length reduces, the boundary scattering enhances as we discussed previously, which will lead to reduction of mean free path and in turn thermal conductivity (Classical size effect). Quantum confinement also occurs because the smallest increment of wavevector $\frac{2\pi}{L}$ increases as L decreases. The quasi-continuous dispersion for bulk materials becomes discrete and the DOS changes. We note that these size effects are true for electrons as well as phonons.[31]

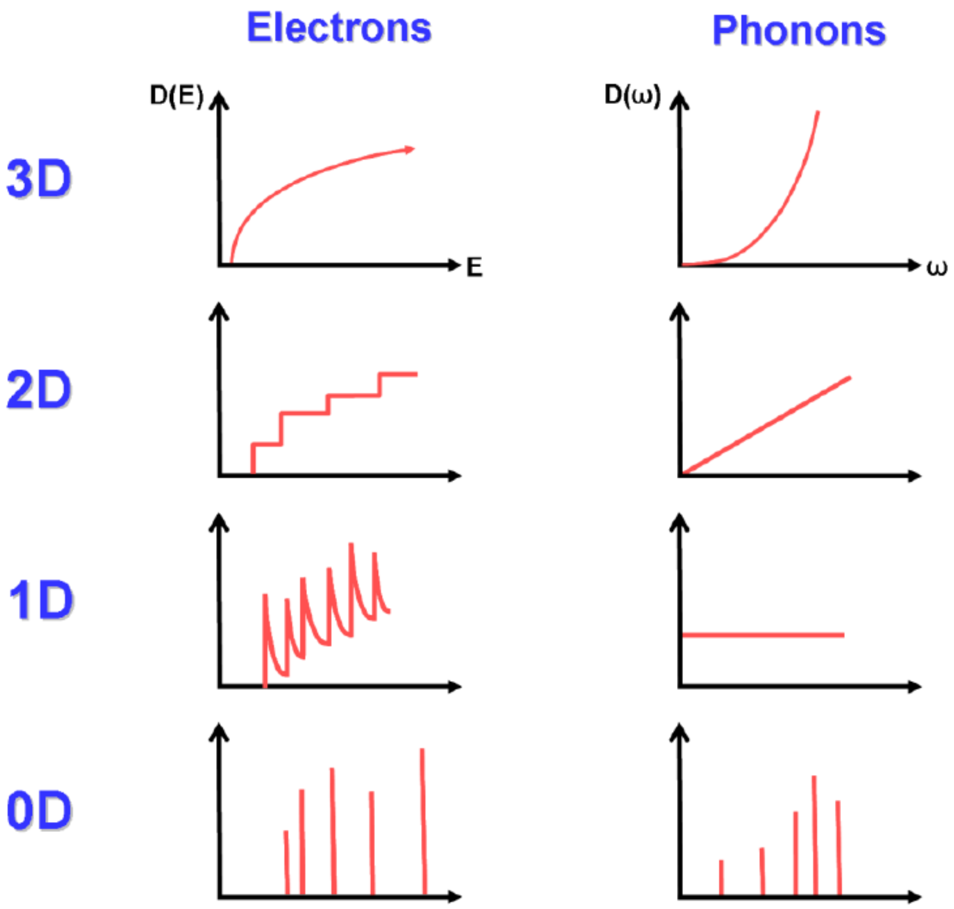

Figure 1.4 Electronic and phononic density of states in low dimensional materials due to quantum confinement [Ref 31].

1.3 Thermal conductivity measurement (3 omega technique)

1.3.1 Basic Principle and Experiment Setup

We used 3 omega technique to measure the thermal conductivity of the materials of interest. The 3 omega technique, originally developed by Cahill,[32] have been widely applied to thermal conductivity measurements for thin film geometries. In brief, 3 omega technique uses a metal line on top of the sample as a combined resistive heater and thermometer. During measurements, heat flux is generated by running an AC current, I(ω), through the metal line. The excited AC current leads to a temperature oscillation of the metal line at 2 ω, which in turn causes the oscillation of electrical resistance of the metal line R(2ω). Combined the 1ω current I(ω) and 2ω electrical resistance R(2ω) gives a 3ω voltage V(3ω) = I(ω)* R(2ω), which contains the temperature information.

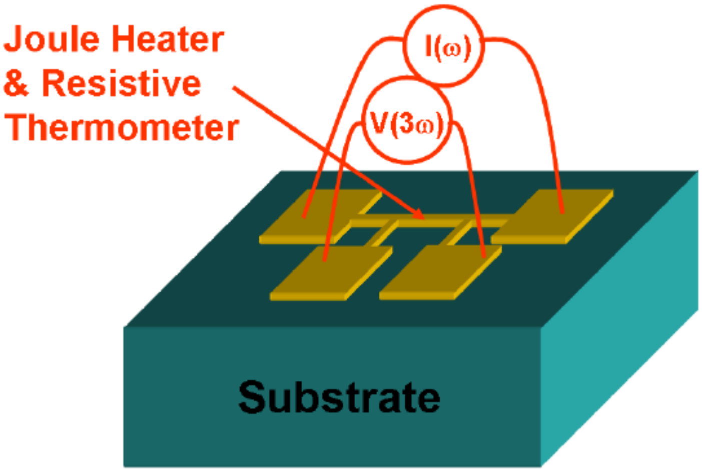

Figure 1.5 Schematic illustrates 3 ω technique

The instrumental of our 3 omega station strictly follows the modified design suggested by Feser[33]. Both current source (Keithley 6221) and the built-in voltage source of lock-in amplifier (Stanford Research Systems SR830) have been identified as appropriate power source. The lock-in amplifier is also used to measure the 3rd harmonic voltage signals V(3ω). A potentiometer with known resistance (R_{pot}) is placed in series with the sample's resistive heater. Prior to measurement, a small excitation DC current is running through the resistive heater and the potentiometer to determine the resistance of heater (R_s) by measuring the voltage drop, $R_s = R_{pot} \frac{V_S}{V_{pot}}$. Then, a larger AC current is excited and driven through the sample's heater, at which point the 3rd harmonic voltage signal is measured. As suggested by Dames[34], instead of directly measuring $V_{3w,s}$, we adjust the multiplying digital-to-analog (DAC) converter so that the multiplying constant is $\alpha = R_s/R_{pot}$, and then measure the differential 3rd voltage signal $V_{3w,diff} = V_{3w,s} - V_{3w,\alpha pot}$. This helps eliminate any undesired response and the signals only comes from the sample. The temperature fluctuation in heater could be determined by:

$$\Delta T = 2R_S \frac{dT}{dR} \frac{V_{3\omega,diff}}{V_{1\omega,S}}$$

To convert 3ω electrical signals into thermal responses, the temperature coefficient of resistance ($TCR = \frac{1}{R_S} \frac{dR_S}{dT}$) is measured using a home-built thermal stage. In this measurement, the resistances of the 3ω lines were measured at 5 different temperature points between 15°C and 30°C, and a linear fit was used to determine the slope.

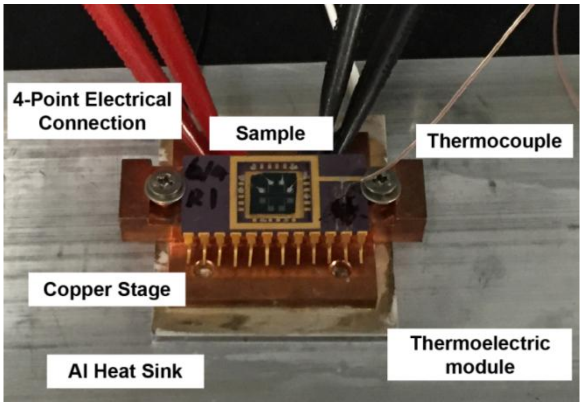

Figure 1.6 Home-built stage for temperature coefficient of resistance (TCR) measurement.

1.3.2 Data Reduction

For a multilayer-film-on-substrate system, an analytic solution for 2-D heat conduction was reported by Borca-Tasciuc.[35] The temperature change on the heater ΔT could be expressed as:

$$\Delta T = \frac{-P}{\pi l k_{y1}} \int_0^\infty \frac{1}{A_1 B_1} \frac{\sin^2(b\lambda)}{b^2 \lambda^2} d\lambda$$

where

$$A_{i-1} = \frac{A_i \frac{k_{yi} B_i}{k_{y,i-1} B_{i-1}} - \tanh(\varphi_{i-1})}{1 - A_i \frac{k_{yi} B_i}{k_{y,i-1} B_{i-1}} \tanh(\varphi_{i-1})}, \text{ i= 2,...n,}$$

$$B_i = (k_{xyi}\lambda^2 + \frac{i2\omega}{\alpha_{yi}})^{1/2} ,$$

$$\varphi_i = B_i d_i, \;\; k_{xy} = \frac{k_x}{k_y} .$$

In the above expressions, *n* is the total number of layers including substrate, and subscript *i* represents the *ith* layer from top to bottom. Other parameters are: k is thermal conductivity, α is thermal diffusivity, d is layer thickness, ω is angular frequency, P is heater power, *l* is heater length and *b* is the half heater width.

We note that the analytic solution in general needs iterative substitution to fit the temperature profile. As suggested by Cahill[32], a simpler formula of could be used to calculate the temperature change on substrate under two assumptions: a. Line heater assumption, which requires the penetration depth $q^{-1} = \sqrt{\alpha_s/2\omega}$ to be much larger than the heater half width b; b. Semi-infinite substrate assumption, which requires the penetration depth $q^{-1} = \sqrt{\alpha_s/2\omega}$ to be much smaller than substrate thickness.

$$\Delta T_s = \frac{P}{\pi l k_s}\left(0.5ln\left(\frac{\alpha_s}{b^2}\right) - 0.5ln(\omega) + \eta\right) - i\left(\frac{p}{4lk_s}\right)$$

where η is a constant and has been evaluated to be ~ 0.923. Importantly, using this formula, the thermal conductivity of substrate could be calculated as simple as:

$$k_s = -\frac{P}{2\pi l}\left(\frac{d(\Delta T_S)}{d(ln(2\omega))}\right)^{-1}$$

And the thermal conductivity of a thin film could then be derived using 1D heat conduction model if the thin film thickness (T_f) is much less than half heater width (b)

$$k_f = \frac{Pt_f}{L\omega\Delta T_f}$$

1.3.3 Calibration samples

To calibrate our 3 omega setup, a total of six control samples have been measured and the results are summarized in Table 2. Among these control samples, three of them are bulk samples (Si, GaAs and quartz) and three are thin film samples (amorphous Al_2O_3, amorphous SiO_2 and polystyrene) with thickness ranging from 50 - 200 nm. Our results are in excellent agreement with the suggested values in literature.

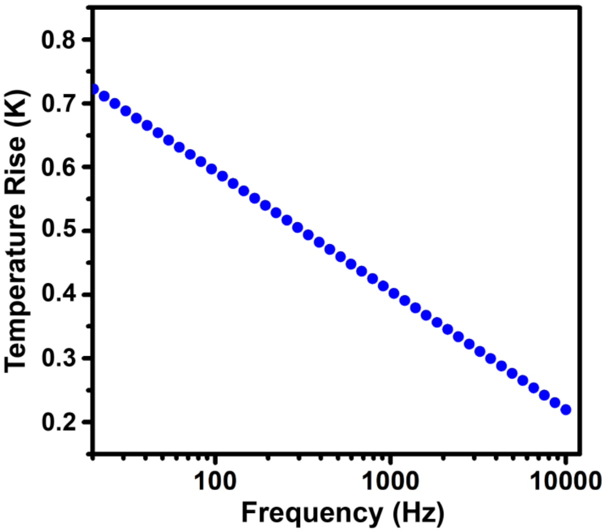

Figure 1.7 3 ω data of a bulk quartz sample. Temperature rise of the heater decreases as frequency increases.

Table 1.1 Summary of control samples that used for 3 ω station calibration

Sample	Sample Type	Thickness	Line Dimension	Measured Thermal Conductivity	Reference
Si	Bulk	~ 500 um	3 X 200 um 5 X 500 um 45 X 2600 um	148 ± 10 W/m-K	142 W/m-K[36]
Fused Quartz	Bulk	~ 500 um	3 X 300 um	1.4 ± 0.1 W/m-K	1.35 W/m-K[37]
GaAs	Bulk	~ 500 um	3 X 180 um	48.6 ± 2.0 W/m-K	55 W/m-K[38]
Amorphous Al_2O_3	Thin film	150 nm	45 X 2600 um	1.5 ± 0.1 W/m-K	1.6 W/m-K[39]
Amorphous SiO_2	Thin film	50 nm	3 X 300 um	1.4 ± 0.1 W/m-K	1.3 W/m-K[40]
Polystyrene	Thin film	200 nm	45 X 2600 um	0.14 ± 0.02 W/m-K	0.15 W/m-K[41]

1.4 Size dependent melting of nanostructures

Size-dependent melting is a phenomenon commonly observed in nanostructures. It originates from the large surface to volume ratio as the characteristic length falling into the nanometer range. Pawlow predicts this effect as early as 1909 by considering the equilibrium state between solid and liquid that have the same vapor pressure.[42] Buffet and Borel modified Pawlow's formula later, and their model is usually refer to homogeneous melting model (HMM).[43] As the name indicates, this model ignores the surface melting and considers the melting occurs suddenly throughout the crystal once the temperature reaches the melting point. Other two important thermodynamic models are liquid skin model (LSM) proposed by Couchman[44] and liquid growth model (LGM) proposed by Wronski.[45] In these three models, the relation between nanoparticle size and melting point can be written in a similar form as below: [46]

$$\frac{T}{T_b} = 1 - \frac{4V}{H}[\gamma_{sv} - \gamma_{lv}(\frac{\rho_s}{\rho_l})^{2/3}]\frac{1}{d} \quad (HMM)$$

$$\frac{T}{T_b} = 1 - \frac{4V}{H}\left[\frac{\gamma_{sl}}{(d-2\delta)}\right] \quad (LSM)$$

$$\frac{T}{T_b} = 1 - \frac{6V}{H}[\gamma_{sv} - \gamma_{lv}(\frac{\rho_s}{\rho_l})^{1/2}]\frac{1}{d} \quad (LGM)$$

where T and T_b represents the melting temperature of nanoparticle and bulk materials, respectively. Other parameters are: H stands for bulk enthalpy of fusion, V stands for molar volume, γ stands for interfacial energies between two states, ρ stands for density and d stands for the diameter of nanoparticle. Distinct from HMM, LSM proposes the existence of a liquid layer with constant thickness δ below the melting temperature, and this parameter is always used as a fitting factor. It should be noted that LSM predicts a nonlinear relations between T and d due to the parameter δ. As shown in the formulas, LGM has a very similar expression as HMM, and both models predict a linear relationship between T and d. Which differs from HMM is that LGM also takes surface melting into consideration, and thereby predicts a larger magnitude of melting point depression compared to HMM.

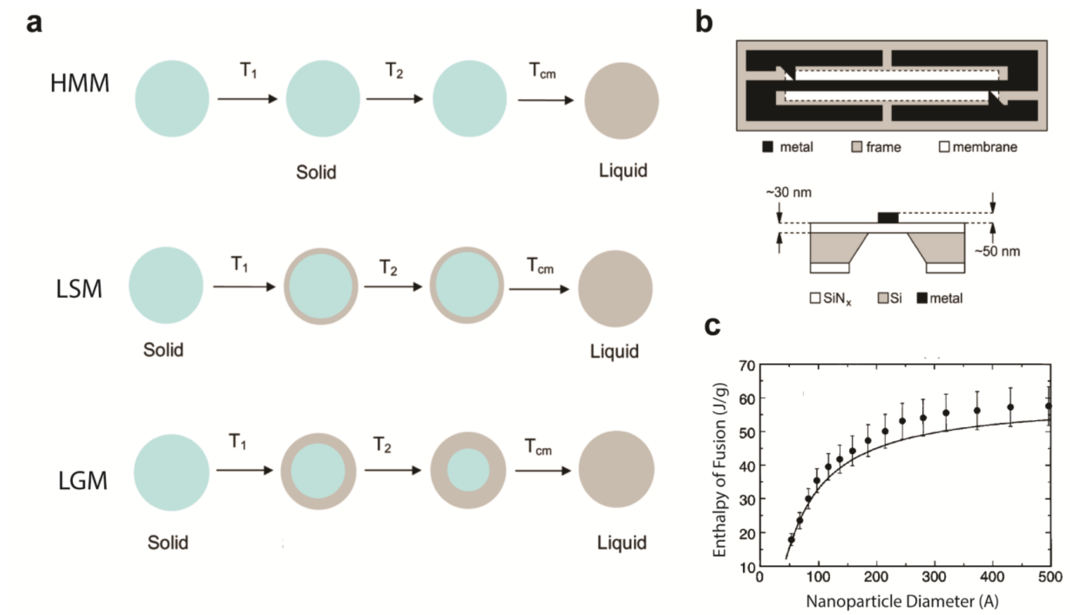

Figure 1.8 (a) Illustrative scheme of three thermodynamic model for size-dependent melting of nanoparticles, (b) Micro-fabricated nanocalorimetric platform for enthalpy of fusion measurements on nanoparticles [Ref 101]. (c) First experimental demonstration on size-dependent melting enthalpy of fusion on Sn nanoparticles by Lai et al. [Ref 48].

The first experimental observation on melting point depression of nanoparticles is made by Takagi using scanning diffraction method.[47] In this experiment, nanoparticles formed by evaporating low melting metals (Sn, Bi and Pb) on cleavage faces of silicon carbide single crystal. The diffraction pattern was then monitored by a electron diffraction camera at different temperatures. The melting temperature was determined by finding the right point when the diffraction pattern disappeared. A more comprehensive experimental study was later carried out by Buffet and Borel, which have shown that the melting temperature of gold nanoparticles could be varied as large as 500℃ as the diameter reduced from ~20 nm to ~3 nm.[43] This study motivates us to decouples the phase change material's melting temperature from its chemical composition.

Compared to melting temperature, the size-dependent enthalpy of fusion was not experimentally demonstrated until 1996. The difficulty of measuring this quantity lies on extracting the small amount of heat during nanoparticle melting. To solve this problem, Lai *et al.* [48] micro-fabricated a platform with very small thermal mass. As Figure 2b shows, a thin metal line was designed as a heater and a thermometer. As a support, the SiN_x membrane is fabricated with 50 nm in thickness, which in turn leads to small thermal mass. During measurements, a DC current is running through the heater, and the temperature change was determined by measuring the resistance change of the metal line. Given the temperature - resistance dependence, the temperature change was determined. To extract the amount of latent heat, the temperature profile was then compared to a control sample, which performs in a same condition but contains no nanoparticle. Figure 1.8c shows a size-dependent enthalpy of fusion of Sn nanoparticles as reducing the particle diameters.

1.5 Thermal Storage and Phase Change Materials

Thermal energy in solid could be stored in three different forms, sensible heat, latent heat and chemical bonds. Among these three mechanisms, sensible heat is the most common one, which utilizes material's specific heat to store energy. The drawback of this approach is the relative low energy density. Chemical thermal energy storage uses a chemical reaction to realize the energy absorption/release. Although an excellent energy density could be achieved in this manner, the control over the reaction and experimental condition have always been a challenge for practical applications. To accomplish thermal charging/discharging, the third approach utilizes the solid-liquid phase transformation of a thermal storage material as temperature increased/decreased. This mechanism is easy to implement and in general has a greater energy density compared to sensible heat storage. The thermal storage medium employed in a phase change system is often named as phase change material (PCM).

A proper PCM should have certain physical properties, among which three thermal properties are of the greatest importance. They are melting temperature, thermal energy density and thermal conductivity. [49, 50] The melting point of a PCM needs to be matched with a given working temperature in practical situations. This is the first requirement for selecting a suitable material. Once the melting temperature is satisfied, the next goal is to find a material with large energy density. Thermal energy density is a property describes how dense the energy can be stored in a material, and it could be evaluated by gravimetric basis or volumetric basis depending on working conditions. For mobile devices, gravimetric-based performance is of more importance, while for stationary storage purposes, volumetric energy density is more concerned. Accompany with these two, thermal conductivity is also important because it determines the energy transport rate in the system.

Thermal properties of typical phase change materials are listed in Table 1.2 [49-52] In general, PCMs can be classified into four categories: organics, hydrates, salts and metals. As the table shows, the employment of organics and hydrates are typically restricted to applications below 10 - 120 °C. At higher temperature, metallic materials and salts are two choices. Salts are more attractive due to the abundance and low cost, however they suffer from corrosion issues and slow charging/discharging rate, which could be attributed to the low thermal conductivity. In contrast, metals are in general excellent heat conductors and have similar energy densities as volumetric basis calculation is applied. Previous studies have not seriously considered metals primarily due to its poor gravimetric energy density. However, metals should find applications in high temperature stationary thermal storage systems.

Table 1.2 Thermal properties of typical phase change materials

	Melting Temperature range (℃)	Gravimetric latent heat (J/g)	Volumetric latent heat (J/cm^3)	Thermal Conductivity (W/m-K)
Organics	10-120	~ 100-300	~80-450	~0.1-0.5
Salt hydrates	10-120	~100-300	~150-500	~0.5-1
Salts/ Salt Mixtures	100-900	~100-1000	~200-2200	~0.5-5
Metals/ Metal alloys	100-900	~50-800	~ 500-2400	~10-430

1.6 Overview of this dissertation

This dissertation presents four studies on investigating thermal properties of colloidal nanocrystal assembles and composites. The first work (Chapter 2) examines how to manipulate the thermal transport in colloidal nanocrystal solids via structure modifications. This work is of significant importance because nanocrystal solids has been used for a variety of applications, and in each of these applications, the thermal transport property plays a big role. For example, a low thermal conductivity is desirable for thermoelectrics, and a high thermal conductivity is beneficial for electronics and LEDs.

In Chapter 3, the phase change behavior of several colloidal metallic nanocrystals (In, Sn, and Bi) is studied. This work is of interests from two aspects. First, the solid-liquid transformation of colloidal nanocrystals are largely unexplored and it could have distinct phase change behaviors than other type of nanoparticles. Secondly, the phase stability of nanocrystals is also important to applications operates at elevated temperatures, such as solar cells and catalyst.

Chapter 4 presents an example of applying metallic colloidal nanocrytasl for phase change thermal storage application. The use of nanocrystals provides flexibility to control phase change material's melting temperature via changing size. Hence, this material could a potential solution for thermal energy storage at the temperature region (200 - 300 ^{o}C) that inaccessible for organics.

In Chapter 5, a solution-phase synthesis on metal matrix-metal nanoparticle composite has been developed. This approach has the advantage over other techniques that it enables excellent control over nanoparticle's morphology. In addition, this metallic composite was demonstrated a phase change material with a thermal conductivity 2 - 3 orders of magnitude greater than typical phase change materials. This high thermal conductivity could facilitate fast thermal energy charging/discharging rates in thermal cycles.

CHAPTER 2

MODIFYING THMERMAL TRANSPORT IN NANOCRYSTAL SOLIDS USING SURFACE CHEMISTRY

ABSTRACT

We present a systematic study on the effect of surface chemistry on thermal transport in colloidal nanocrystal (NC) solids. Using PbS NCs as a model system, we vary ligand binding group (thiol, amine, and atomic halides), ligand length (ethanedithiol, butanedithiol, hexanedithiol, and octanedithiol), and NC diameter (3.3-8.2 nm). Our experiments reveal several findings: (i) The ligand choice can vary the NC solid thermal conductivity by up to a factor of 2.5. (ii) The ligand binding strength to the NC core does not significantly impact thermal conductivity. (iii) Reducing the ligand length can decrease the interparticle distance, which increases thermal conductivity. (iv) Increasing the NC diameter increases thermal conductivity. (v) The effect of surface chemistry can exceed the effect of NC diameter and becomes more pronounced as NC diameter decreases. By combining these trends, we demonstrate that the thermal conductivity of NC solids can be varied by an overall factor of 4, from ~ 0.1-0.4 W/m-K. We complement these findings with effective medium approximation modeling and identify thermal transport in the ligand matrix as the rate-limiter for thermal transport. By combining these modeling results with our experimental observations, we conclude that future efforts to increase thermal conductivity in NC solids should focus on the ligand-ligand interface between neighboring NCs.

Colloidal nanocrystals (NCs) are an important class of nanoparticle that can be synthesized with precise size, shape, and composition. This morphological control enables excellent control over NC properties and facilitates their use as building blocks for nanocomposites with novel and tunable properties that are unachievable in bulk materials.[53-55] One commonly studied NC-based material is the colloidal NC solid, which consists of a densely packed array of colloidal NCs. These colloidal NC solids have been employed across a wide range of applications including light emitting diodes (LEDs),[15, 16] photovoltaics,[17, 18] electronics,[19, 20] thermal storage,[55, 56] and thermoelectrics.[57, 58] In each of these applications, thermal transport properties play an important role. For example, a high thermal conductivity is desirable for LEDs, photovoltaics, and electronics because this minimizes temperature rise during operation, which improves both device performance and lifetime. A high thermal conductivity is also beneficial for thermal storage because it facilitates fast thermal charging/discharging. In contrast, a low thermal conductivity is ideal for thermoelectric applications because this improves efficiency in thermoelectric coolers and generators. Despite the importance of thermal conductivity in each of these applications, experimental data on thermal transport in NC solids is very limited.[59]

Colloidal NCs consist of an inorganic crystalline core with ligands bound to its surface. The native ligands on colloidal NCs are typically bulky organic molecules (e.g. oleic acid, trioctylphosphine oxide, alkanethiols, etc.). These native ligands help control the nucleation and growth of colloidal NCs during synthesis and are hence necessary from a synthetic perspective. However, these native ligands are generally undesirable from a functional materials perspective (e.g. electrically insulating). Previous studies have shown that the choice of ligands dramatically affects NC properties,[22-28] and it is now a common practice to replace the native ligands with new ligands that impart desirable properties. For example, by replacing the native dodecanethiol ligands with metal chalcogenide complexes, the electrical conductivity of Au NC solids was increased by 10 orders of magnitudes.[26] In another example, the optical absorption of PbS NCs was increased by a factor of 3 through the use of short conjugated ligands.[27] In addition to these intended effects on electrical and optical properties, it is important to understand how ligand choice affects thermal transport.

Thermal transport in NC solids was first experimentally studied by Ong *et al*.[59] They found very low thermal conductivities and that NC diameter had the biggest impact on this property. They also conducted limited experiments on ligand-exchanged NC solids and found moderate thermal conductivity increases of ~ 50%. A couple of molecular dynamics studies have since confirmed the importance of NC diameter on thermal transport and also identified the NC core-ligand interface as an important parameter.[60, 61] While these studies are important landmarks in the study of thermal transport in NC solids, important questions regarding the effect of surface chemistry remain. How does the ligand’s binding group and backbone length affect thermal transport in NC solids? Can ligand exchange increase NC solid thermal conductivity beyond the moderate 50% demonstrated by Ong *et al.*? How is the impact of surface chemistry on thermal transport affected by NC diameter?

To address these questions, we study thermal transport in PbS NC solids and systematically vary NC diameter and ligand structure. Our choice of PbS as a model system is motivated by the technological importance of PbS NC solids to optoelectronic applications, such as photodetectors[6, 62] and photovoltaics.[18, 24, 63] In addition, PbS is among the most well understood colloidal NCs and there is a wide body of literature detailing its structure,[64, 65] properties,[66, 67] and behavior.[68, 69] The native ligands on the PbS NCs in this study are oleic acid (OA) and we exchange these with ligands of varying backbone length (ethanedithiol, butanedithiol, hexanedithiol and octanedithiol) and different binding groups (thiols, amines, and halides). Our experiments reveals several findings: (i) The choice of ligand can increase the thermal conductivity of NC solids by up to ~ 150%. (ii) The ligand binding strength to the NC core does not significantly impact thermal conductivity. (iii) Reducing the ligand length can decrease the interparticle distance, which increases thermal conductivity. (iv) Increasing the NC diameter increases thermal conductivity. (v) The effect of surface chemistry can exceed the effect of NC diameter and becomes more pronounced as NC diameter decreases. By combining these trends, we demonstrate that the thermal conductivity of NC solids can be varied by an overall factor of 4, from ~ 0.1-0.4 W/m-K. We complement these thermal transport findings with effective medium approximation (EMA) modeling and identify thermal transport in the ligand matrix as the rate-limiting factor for heat transfer. By combining our experimental observations with these modeling results, we conclude that future efforts to increase thermal conductivity in NC solids should focus on the ligand-ligand interactions between neighboring NCs.

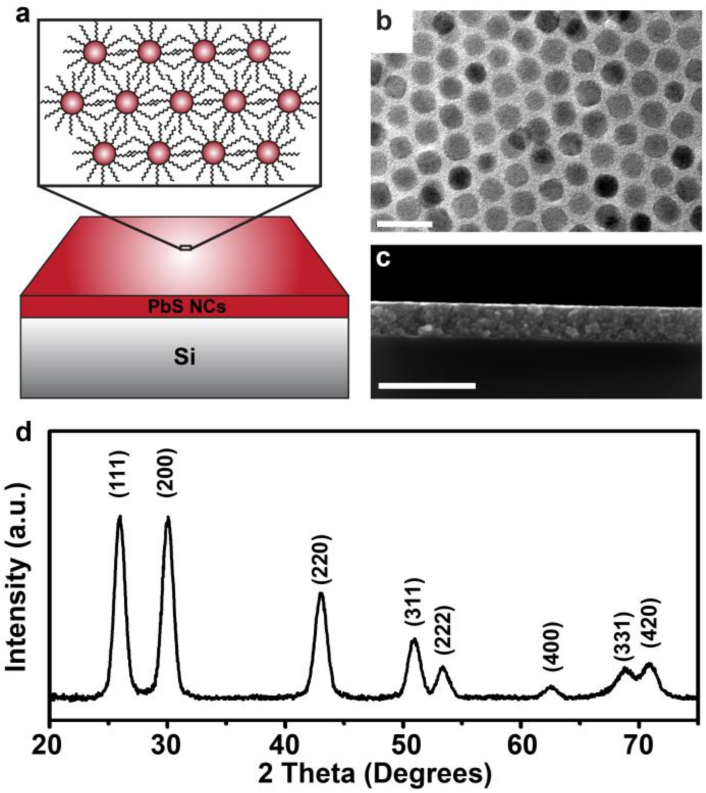

Figure 2.1 (a) Schematic of a PbS nanocrystal solid thin film on a silicon substrate. (b) A transmission electron microscopy image of 8.2 ± 0.7 nm PbS nanocrystals with native oleic acid ligands (the scale bar is 20 nm). (c) Cross-sectional scanning electron microscopy image showing a nanocrystal solid thin film that consists of 8.2 nm PbS nanocrystals with I^- ligands (the scale bar is 500 nm). (d) X-ray diffraction pattern of 8.2 nm PbS nanocrystal solid thin film with oleic acid ligands.

Results and discussion

We synthesized PbS NCs with OA ligands using the hot-injection method described by Hines *et al*.[70] Figure 2.1b shows a representative transmission electron microscopy image of the PbS NCs made using this approach and x-ray diffraction confirms the crystalline structure of the PbS core (Figure 2.1d). Varying the reaction conditions enabled NC diameter control from 3.3 to 8.2 nm. After synthesis, the PbS NCs were spin-coated onto silicon substrates to yield a NC solid thin film (Figures 2.1a and 2.1c). The native OA ligands were then replaced with new ligands using a solid-state process. Seven different surface treatments were performed in this study: 1,2-ethanedithiol (EDT), 1,4-butanedithiol (BDT), 1,6-hexanedithiol (HDT), 1,8-octanedithiol (ODT), ethylenediamine (EDA), tetrabutylammonium iodide (TBAI), and cetrimonium bromide (CTAB). The structures of these molecules are illustrated in Figure 2.2b. We note that treating PbS NCs with TBAI and CTAB results in an NC surface that is terminated with I^- and Br^-, respectively (i.e. the bulky organic component of these molecules washes away during the ligand exchange process).[18, 24, 71] For simplicity purposes, we refer to these as I^- and Br^- ligands throughout this paper. Fourier transform infrared spectroscopy measurements confirm the success of these ligand exchanges (Figure 2.2a). The absence of the native OA ligands is indicated by the lack of COO^- and C = C absorptions, which are at 1500-1700 cm^{-1}, in all ligand exchanged samples.

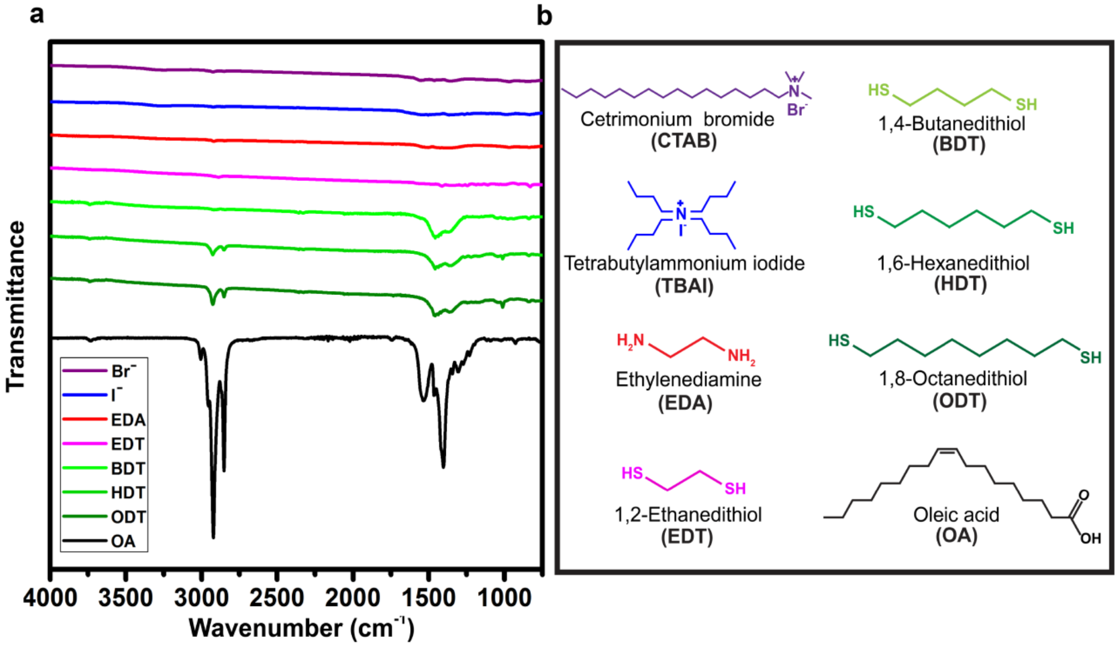

Figure 2.2. (a) Fourier transform infrared spectra of PbS nanocrystal solids with various ligands. (b) The chemical structure of the molecules used during ligand exchange. Note that treating PbS nanocrystals with tetrabutylammonium iodide (TBAI) and cetrimonium bromide (CTAB) results in nanocrystal surface terminations of I^- and Br^-, respectively [References 17 and 71].

To prepare high-quality film for thermal conductivity measurements, we carried out the solid-state ligand exchange process using a layer-by-layer (LBL) approach (Figure 2.3a).[69, 72, 73] Each layer was prepared in three steps: a) Depositing a thin layer of PbS NCs with OA ligands via spin coating; b) Immersing the NC solid film in a solution containing the desired ligand (typically 30 s) and spinning dry; c) Removing unbound ligand molecules by repeatedly flooding the NC solid film with pure solvent and spinning dry. Depending on the NC diameter and ligand choice, each layer deposition resulted in a NC solid thin film of 10-25 nm. This deposition process was then repeated 6-10 times to yield thicker films (100-180 nm) that are appropriate for thermal conductivity measurements. Films prepared by this approach exhibited excellent film quality with minimal porosity/cracking (Figure 2.3b). In contrast, NC solid films prepared via one-time solid-state ligand exchange on thick films exhibited extensive/deep cracking that made them unsuitable for transport measurements.

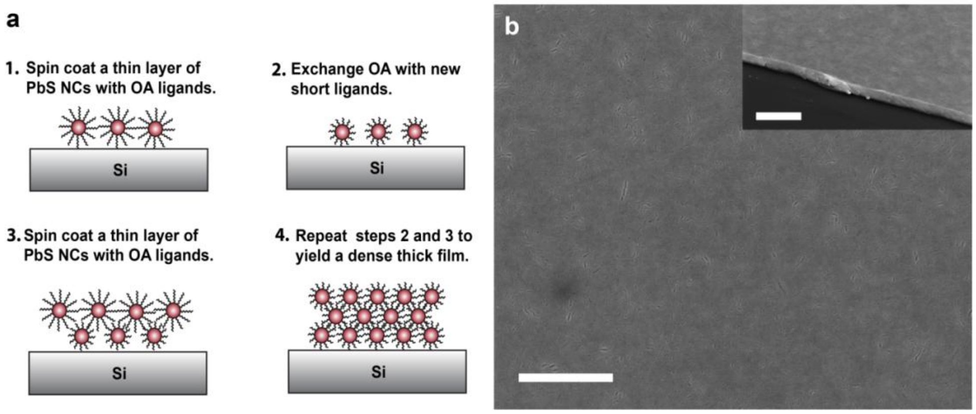

Figure 2.3. (a) Schematic illustrating the solid-state, layer-by-layer ligand exchange technique used to prepare nanocrystal (NC) solid films. This layer-by-layer technique minimizes film cracking during exchange of the long oleic acid (OA) ligands with new short ligands. (b) Scanning electron microscopy image of a 3.3 nm PbS NC solid with ethanedithiol ligands. The inset in part (b) shows an angled view of the NC solid film that confirms dense NC packing throughout the film thickness. The scale bar in both images is 1 μm.

We first investigate the effect of the ligand's binding group on the NC solid thermal conductivity (Figure 2.4). This is motivated by past thermal transport studies on a closely related cousin to colloidal NCs, self-assembled monolayer (SAM) junctions.[74, 75] SAMs are molecular monolayers adsorbed onto planar solid surfaces[76] and prior work has shown an increasing thermal interface conductance as the binding strength between the SAM molecules and solid surface increases.[74, 75] In effect, we ask ourselves whether this correlation between binding strength and thermal transport can be realized in the more complex structure of NC solids. To investigate this, we compare the thermal conductivity of 3.3 nm diameter PbS NC solids with EDA and EDT ligands. These two ligands have identical backbones, but different binding groups: amine groups for EDA and thiol groups for EDT. Both of these groups form covalent bonds to PbS NCs, although it is known that the thiol group forms a stronger bond.[77] Interestingly, we find that PbS NC solids with EDA ligands have a higher thermal conductivity than with EDT ligands (Figure 2.4). This contrasts with data on SAM junctions, in which the thermal conductance through strong thiol-Au bonds is notably larger than the thermal conductance through weaker amine-Au bonds.[74] To expand upon this binding group motif, we also prepared PbS NC solids with halide ligands (Br^- and I^-). These ligands form ionic bonds to the NC surface, of which the PbS - Br^- bond is known to be the stronger of the two.[69] We find that the thermal conductivity of NC solids with these two ligands are essentially equivalent and do not reflect the prediction based on bond strength as well. Based on these experimental observations, we conclude that the thermal conductance of the NC core-ligand interface (*i.e.* the binding strength between the NC core and ligand) does not dominate thermal transport in NC solids. As based upon our EMA modeling (see below), we hypothesize that the ligand-ligand interface between neighboring NCs is the critical interface for thermal transport in NC solids.

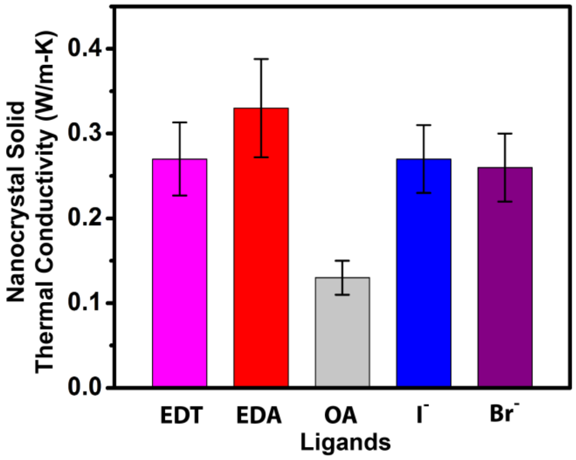

Figure 2.4. Thermal conductivity of 3.3 nm PbS nanocrystal solids with ethanedithiol (EDT), ethylenediamine (EDA), oleic acid (OA), I^-, and Br^- ligands.

We next study the effect of ligand length by using a series of alkanedithiol ligands with 2, 4, 6, and 8 carbon atoms (*i.e.* EDT, BDT, HDT, and ODT, respectively) on 3.3 nm PbS NC solids. As the ligand backbone decreased from 8 carbon atoms to 4 carbon atoms, the NC solid thermal conductivity increased from 0.20 W/m-K to 0.27 W/m-K (Figure 2.5a). We attribute this trend to a reduction of interparticle distance, which increases the NC core volume fraction in the solids. It is not surprising that this increases the thermal conductivity of the NC solid because the thermal conductivity of PbS is an order of magnitude higher than hydrocarbons.[78, 79] We also used x-ray reflectivity (XRR) to determine the mass densities of the NC solids with varying ligands, and then converted these values into interparticle distances using geometric. We found that our interparticle distance measurements agree to within experimental uncertainty with much more sophisticated synchrotron x-ray scattering measurements.[64] Our interparticle distance trend shows an inverse correlation with our measured thermal conductivities (Figures

2.5a and 2.5b), which supports our conclusion that interparticle distance is an important parameter affecting the thermal conductivity of NC solids. Interestingly, our results show no thermal conductivity increase as the ligand backbone is further reduced from 4 to 2 carbon atoms (BDT and EDT, respectively). While counterintuitive, we find that this thermal conductivity result still mirrors our findings on interparticle distance, which reveal approximately equivalent interparticle distances for BDT and EDT. We hypothesize that this change in trend for interparticle distance and thermal conductivity originates from a change in chemical binding motifs (Figure 2.5c). Similar property trend changes for varying alkanedithiol lengths have been observed in other works as well.[64, 72] Past studies have suggested that dithiol ligands preferentially bridge neighboring NCs (part i in Figure 2.5c).[9, 64, 80] Since our measured interparticle distances for NC solids with ODT, HDT, and BDT are comparable to that of the corresponding molecular lengths,[64] we hypothesize that NC bridging occurs in these cases. However, in the case of EDT, the interparticle distance is notably longer than the molecular length. This implies an alternative chemical binding motif; both bidentate binding[64, 72, 73] and dimerized binding[81, 82] (parts ii and iii, respectively, in Figure 2.5c) have been identified as possible binding arrangements for EDT in NC solids. We also performed XRR measurements on NC solids with EDA ligands and found very short interparticle distances (*i.e.* ~ 0.7 nm). This result suggests that EDA likely bridges NCs and provides an explanation as to why EDA ligands yield a higher NC solid thermal conductivity than EDT (Figure 2.4).

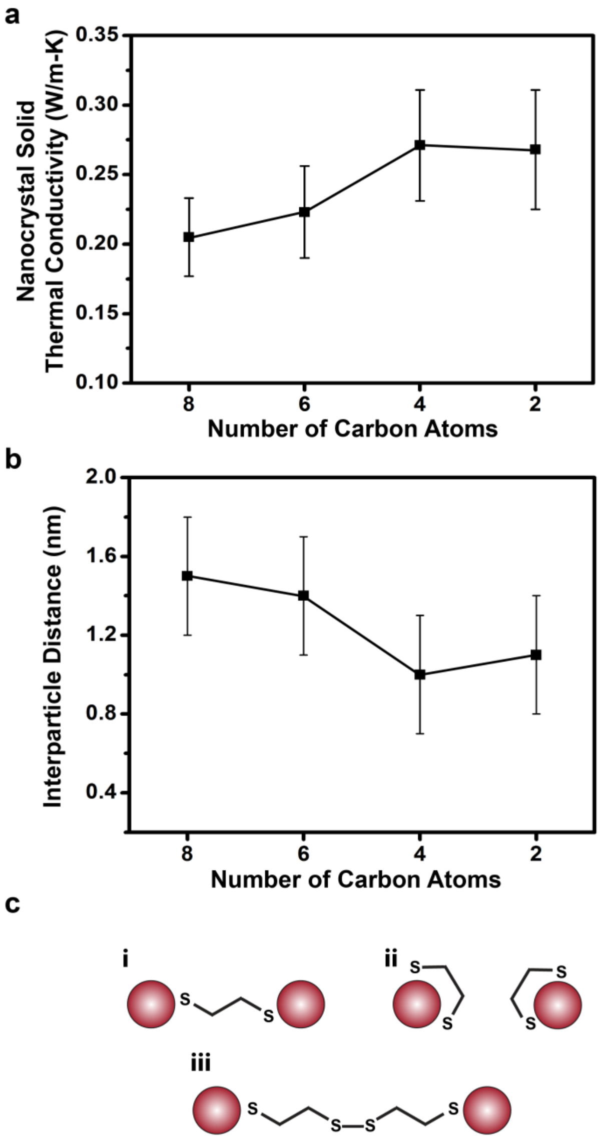

Figure 2.5. (a) Thermal conductivity of 3.3 nm PbS nanocrystal solids with alkanedithiol ligands of varying backbone length. (b) Interparticle distance of 3.3 nm PbS nanocrystal solids with alkanedithiol ligands of varying backbone length. (c) Schematic of various binding possibilities for ethanedithiol in nanocrystal solids: i. bridging, ii. bidentate, iii. dimerized.

We next study the relative impact of surface chemistry on the thermal conductivity of NC solids with varying NC diameter. As a baseline, we first measure the thermal conductivity of PbS NC solids with their native OA ligands. We find that as the NC diameter increases from 3.3 to 8.2 nm, the thermal conductivity increases from 0.13 to 0.27 W/m-K, which agrees with measurements by Ong *et al.*[59] We next prepare each of these NC solids with I^- and EDA ligands and find that the thermal conductivity increases for all diameters (Figure 2.6a). This is consistent with the relationship between thermal conductivity and interparticle distance that we identified earlier. It is also possible that these ligand choices lead to higher effective thermal conductivities in the ligand matrix. In addition, we find that the relative thermal conductivity increase (k/k_{OA}) is greater for smaller diameter NC solids than for larger diameters ones (Figure 2.6b). This trend is consistent with the fact that the ligands make up a greater volume fraction of the NC solid as the NC diameter decreases, and should therefore have a more substantial effect for smaller diameters. We achieve relative thermal conductivity increases of up to 150%, which improves upon the 50% increase demonstrated in prior work.[59] While data in prior work suggests that NC diameter is the parameter that most effects NC solid thermal conductivity,[59-61] our findings demonstrate that surface chemistry can have an even larger impact. For example, consider the case of a 3.3 nm PbS NC solid with OA ligands, which has a thermal conductivity of 0.13 W/m-K. Increasing the NC diameter to 8.2 nm and keeping the native OA ligands leads to a thermal conductivity of 0.27 W/m-K. In contrast, keeping the same 3.3 nm diameter, but exchanging the OA with EDA leads to an even higher thermal conductivity of 0.33 W/m-K. Naturally, the effect of NC diameter and surface chemistry can be combined; we achieve our lowest thermal conductivity in

3.3 nm PbS with OA ligands and our highest thermal conductivity in 8.2 nm PbS with EDA ligands. Overall, we find that within our size range (~ 3-8 nm), the thermal conductivity of NC solids can be varied from approximately 0.1-0.4 W/m-K, which demonstrates a moderately larger range of possibilities than prior work.[59]

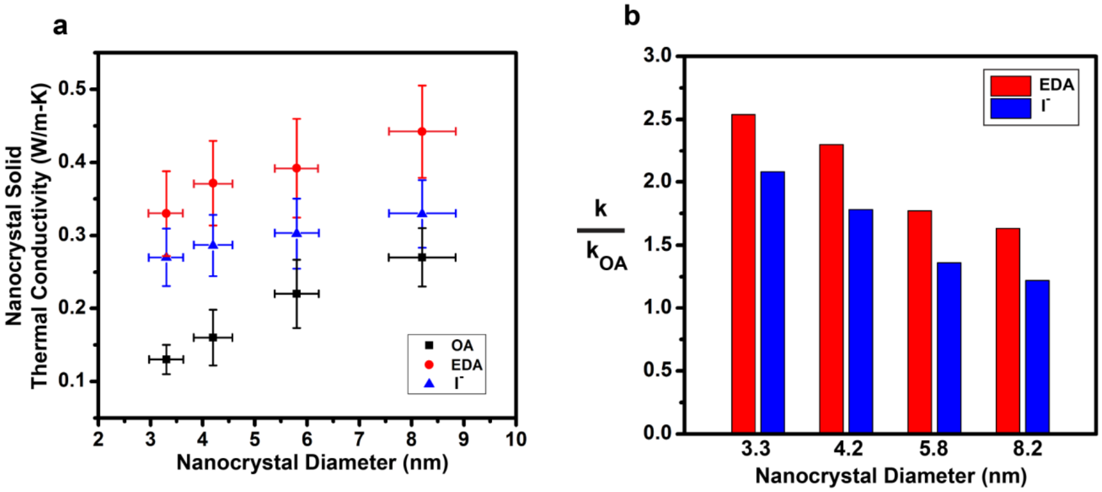

Figure 2.6. (a) Thermal conductivity of PbS nanocrystal solids with varying diameter and ligands; (b) The relative increase of thermal conductivity (k/k_{OA}) in nanocrystal solids with ethylenediamine (EDA) and I^- ligands and varying nanocrystal diameter.

To gauge how this range of NC solid thermal conductivities can be further expanded, we use an EMA model to fit our data on PbS NCs with OA ligands and then perform a sensitivity analysis on the various model input parameters. Since thermal interface conductances significantly impact the thermal conductivity of nanocomposites, we incorporate this factor by using the EMA model proposed by Hasselman and Johnson.[83] This EMA model calculates the thermal conductivity of a composite by accounting for the constituent volume fractions, constituent thermal conductivities, and thermal interface conductance between the constituents. To apply the EMA model to our NC solid, we consider a nanocomposite consisting of NC cores in a ligand matrix. Figure 2.7a shows the EMA model fit to our PbS NC solids with OA ligands and varying diameter, which shows good agreement. In this fit we use 2 W/m-K, 0.13 W/m-K, 2.5 nm, and 220 MW/m^2-K for the NC core thermal conductivity (k_{NC}), ligand matrix thermal conductivity (k_m), interparticle distance, and NC core-ligand thermal interface conductance (G), respectively. Our choice of these input parameters for the model is based upon results in the literature.[59, 64, 74, 84]

To study the relative impact of each parameter (k_{NC}, G, and k_m) on NC solid thermal conductivity, we independently vary each parameter while holding the other two constant (Figure 2.7b). We find that k_m has the largest impact, G has a moderate impact, and k_{NC} has a small impact. As k_m, G, and k_{NC} are each varied by a factor of 5, we calculate changes in NC solid thermal conductivity of 386%, 27%, and 4%, respectively. The insensitivity to k_{NC} is not surprising given that it is an order of magnitude larger than k_m and the core-ligand interfaces further restrict this thermal pathway. Prior experimental work has also found that NC solid thermal conductivity is largely independent of k_{NC}.[59] The fact that the NC solid thermal conductivity sensitivity is much greater to k_m than G means the thermal conductance of the ligand matrix is more important than the thermal conductance of the NC core-ligand interface. This possibly explains why we did not experimentally observe an increase in NC solid thermal conductivity as we increased the NC core-ligand binding strength (which, according to literature on solid-SAM junctions, should have increased the NC core-ligand thermal interface conductance). It is also worth noting that the thermal interface conductance of an individual solid-SAM interface only changes by about a factor of 4 as the solid-SAM bond is changed from van der Waals to covalent.[74, 84] According to our EMA model, this would correspond to an ~ 20% change in NC thermal conductivity. Given that the NC core-ligand bond strength is varied in a much narrower range during our experiments, any thermal conductivity changes arising from NC core-ligand bond strength were likely small, which explains why our measurements did not detect significant changes.

Since k_m affects NC solid thermal conductivity the most, determining ways to increase or decrease k_m is a promising route to achieve an expanded thermal conductivity range beyond that demonstrated in the present work. It is notable that the maximum thermal conductivity for the matrix used in our EMA sensitivity analysis is only 0.5 W/m-K, which is representative of good thermal insulators. Consequently, there should be room to increase the thermal conductivity of the ligand matrix, and by extension, increase the thermal conductivity of the NC solid. This finding inspires us to hypothesize why thermal transport in the ligand matrix is poor to begin with. If we consider heat flow between two neighboring NCs, there are three interfaces: a NC core-ligand interface, a ligand-ligand interface, and then another NC core-ligand interface. Whereas the NC core-ligand interfaces are generally strong covalent or ionic bonds, the ligand-ligand interface is characterized by weak van der Waals forces. Several studies on polymers,[85] molecular crystals,[86] and carbon nanotube – polymer composites[87] have identified weak van der Waals interactions as rate-limiters for heat transfer. We hypothesize that this is also true for thermal transport in NC solids. We note that there is no analogous ligand-ligand interface in solid-SAM-solid structures, which may explain why the solid-molecule binding strength plays a significant thermal transport role in SAMs, but not necessarily in NC solids.

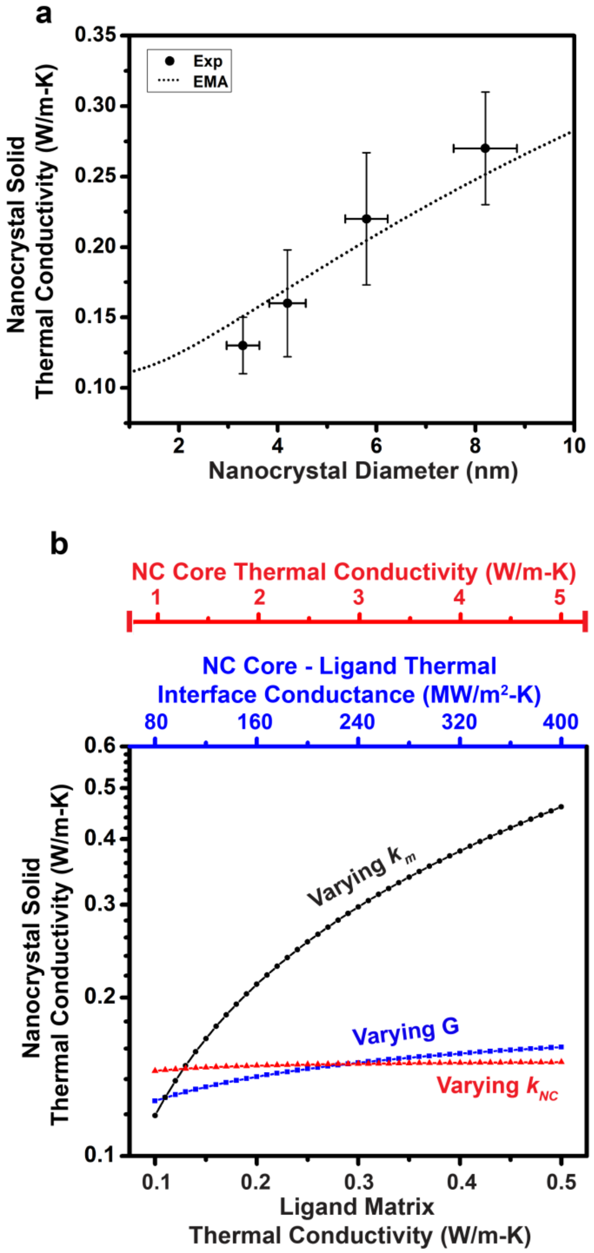

Figure 2.7. (a) Effective medium approximation model results and corresponding experimental data for the thermal conductivity of PbS nanocrystal (NC) solids with oleic acid ligands and varying diameter. (b) Sensitivity analysis on the effective medium approximation model for 3.3 nm PbS NC solids with three independent parameters: NC

core thermal conductivity (k_{NC}, red triangles), NC core-ligand interface thermal conductance (G, blue rectangles), and ligand matrix thermal conductivity (k_m, black spheres)

We hypothesize that two possible ways to increase the thermal conductivity of NC solids are (i) chemically crosslinking the NC ligands to strengthen the ligand-ligand interaction, (ii) eliminating the ligand-ligand interaction by bridging neighboring NCs with bidentate ligands. The first concept has been demonstrated in a recent study on amorphous polymer blends; by introducing appropriately engineered crosslinkers, the thermal conductivity of the polymer blend was increased by a factor of 7.[88] The second approach has been highly sought after in studies to improve charge transport in NC solids,[80, 89, 90] and motivated our choice of bidentate ligands (dithiols and diamine) in this study. However, this approach will likely prove complex because NC surfaces are highly curved, which leads to non-uniform distances between neighboring NCs. This curvature limits the surface area upon which ligand bridging can occur and may explain why we only observed moderately higher thermal conductivities with bridging ligands (e.g. EDA) relative to non-bridging ligands (e.g. EDT and I^-). Using colloidal nanocrystals with flat surfaces (e.g. cubes) and/or more sophisticated ligand chemistries that can achieve bridging throughout the entire NC surface could prove interesting.

Conclusion

We have systematically explored the effect of ligand length, ligand binding group, and NC diameter on thermal transport in colloidal PbS NC solids. The primary effect of decreasing ligand length and/or increasing NC diameter is to increase the NC solid thermal conductivity by decreasing the volume fraction of the thermally insulating ligand matrix. Varying the ligand binding strength to the NC core does lead to significant effects on thermal transport, which contrasts with literature on solid-SAM-solid junctions. We find that the choice of ligands can affect the thermal conductivity by up to a factor of 2.5 and that the thermal conductivity of NC solids can be varied by an overall factor of 4, from ~ 0.1 to 0.4 W/m-K. By combining our experimental observations with EMA modeling, we identified the ligand-ligand interface between neighboring NCs as a critical interface for heat transfer. We then suggested ways to modify this interface and possibly increase NC solid thermal conductivity. Identifying ways to increase thermal conductivity will be beneficial to NC solid applications in electronics and optoelectronics, for which heat dissipation is important to device performance and lifetime. On the other hand, the naturally low thermal conductivities of NC solids bode well for NC solid-based thermoelectrics.

Materials and Methods

Materials and Equipment: Lead oxide (99.999%), bis(trimethylsilyl)sulfide (TMS, synthesis grade), oleic acid (OA, 90%), 1-octadecene (ODE, 90%), tetrabutylammonium iodide (TBAI, 98%+), cetrimonium bromide (CTAB, 99%), 1,2- ethanedithiol (EDT, 98%+), 1,4-butanedithiol (BDT, 97%+), 1,6-hexanedithiol (HDT, 96%+), 1,8-octanedithiol (ODT, 97%+), ethylenediamine (EDA, 99%), methanol (anhydrous 99.8%), acetonitrile (anhydrous 99.8%), octane (98%), were purchased from Sigma Aldrich and used as received. Sample imaging was done with transmission electron microscopy (TEM, Tecnai F20) and scanning electron microscopy (SEM, Nova 200 NanoLab FEI). The X-ray diffraction was taken on high resolution x-ray diffractometer (XRD, PANALYTICAL X'PERT PRO), with CuKα X-ray source operating at 40 kV and 40 mA. Fourier transform infra-red spectroscopy measurements were done using a Thermo Nicolet 6700 system equipped with Smart SAGA accessory. Thickness measurements were carried out using atomic force microscopy (Digital Instrument Dimension 3000) and profilometry (Dektek II surface profilometer). For thermal conductivity measurements, a Keithley 6221 was used as the current source and a Stanford Research Systems SR830 lock-in amplifier was used to measure the 1st and 3rd harmonic voltage signals.

Nanocrystal Synthesis: PbS colloidal NCs were synthesized by employing the hot injection technique reported by Hines et al.[70] with minor modifications. In a typical synthesis of 3 nm PbS NCs, 0.45 g of lead oxide was dissolved in a solvent mixture of 2 mL OA and 18 mL ODE, and degassed by heating under vacuum at 100 °C for 2 hours. After all of the solid dissolved and the solution turned transparent, the temperature was increased to 145 °C, at which point a mixture of 10 mL ODE and 210 uL TMS was injected. The heating mantle was removed from the reaction flask right after the TMS injection, and then replaced when the temperature dropped to 100 °C. The reaction mixture was slowly cooled to ~ 30 °C with the heating mantle in place and turned off. PbS NCs were then separated from the reaction mixture by precipitating with ethanol and resuspending with hexane. This precipitation/suspension process was carried out 3 times in total. To vary NC diameter, the ratio of OA:ODE was varied; higher OA concentration led to larger diameters. The diameters of the PbS NCs used in this study were 3.3 ± 0.3 nm, 4.2 ± 0.4 nm, 5.8 ± 0.4 nm and 8.2 ± 0.7 nm.

Layer-by-Layer (LBL) Ligand Exchange: Ligand exchange in all NC solid films were done using a solid-state ligand exchange process in a LBL fashion. Prior to film deposition, all NCs were precipitated and resuspended an additional 3 times. The NC were suspended in octane with a concentration of 10 - 15 mg/mL for the film deposition. For each layer deposition, ~ 70 μL PbS NC suspension was dispensed onto a 20 mm x 20 mm silicon substrate and spin coated at a speed of 3000 rpm for 1 min. Then, ~ 200 μL of the ligand solution was dispensed onto the NC solid thin film, allowed to rest for 30 s, and then removed by spin drying. The NC solid film was then flooded by ~ 200 μL of pure solvent and then spun dry to remove unbound ligands. The NC solid was then flooded with solvent and spun dry an additional 2 times. Depending on NC size and ligand, each layer deposition resulted in a thin film between 10 - 25 nm. Typically, 6 - 10 layers of NC solid were deposited to yield an appropriate film thickness for thermal conductivity measurements (~ 100 - 180 nm). The ligand solution are prepared as suggested by previous studies:[69, 72] CTAB and TBAI, 30 mM in methanol; EDA, 1 M in methanol; EDT, 1.7 mM in acetonitrile; BDT, 2.5 mM in acetonitrile; HDT, 4 mM in acetonitrile; and ODT, 8 mM in acetonitrile.

Film Thickness Measurement: Thickness measurements on all ligand exchanged NC solid samples were determined by profilometry measurements. NC films were scratched using tweezers and the film thickness measured at the scratch location. The film thickness was determined by averaging measured thicknesses from 3 scans at different locations. The typical thickness variation of a film was found within 10 nm. NC solids with OA ligands were too soft to have their thickness measured with profilometry and were instead measured with atomic force microscopy.

Thermal Conductivity Measurement: Thermal conductivity measurements were performed using the differential 3ω method, which is a widely used technique for thin film geometries.[35, 91] To prepare samples for measurement, NC solid films were first coated with a ~ 150 nm Al_2O_3 dielectric layer. Al metal lines, which function as combined heaters and thermometers, were then deposited on the samples using a shadow mask. The line dimensions in all samples were 45 μm wide, 2.6 mm long, and 150 nm thick. An AC current was run through the Al line to operate it as a heat source and the third harmonic of the voltage response was measured to operate the Al line as a thermometer. In accordance with the differential technique, a reference sample with only dielectric layer and silicon substrate was identically prepared. The thermal response of the NC solid thin film was obtained by subtracting the thermal response of the reference sample from the experimental sample. To convert 3ω electrical signals into thermal responses, the temperature coefficient of resistance (TCR) of 3ω lines were measured using a home-built thermal stage. In this measurement, the resistances of the 3ω lines were measured at 5 different temperature points between 15°C and 30°C, and a linear fit was used to determine the slope.

X-Ray Reflectivity Measurements to Determine Mass Density and Interparticle Distance: X-ray reflectivity (XRR) measurements were carried out using a PANalytical X-ray diffractometer, fitted with an x-ray mirror using a 1/32° slit and a parallel plate collimator. XRR measures the electron density of the sample and can be converted into mass density using the vendor software by providing the sample's elemental ratio (i.e. Pb and S for the nanocrystal core and C, N, S, H, O, I, and Br for the ligands). We determined the number of Pb and S atoms in the nanocrystal (NC) core by comparing the volume of a nanocrystal core, V_{NC}, to the volume of PbS crystal unit cell, $V_{unit\text{-}cell}$. Since each PbS unit cell has four Pb atoms and four S atoms, the number of Pb and S atoms in the NC core ($N_{Pb,\ \mathrm{core}}$ and $N_{S,\ \mathrm{core}}$) can be expressed as:

$$\mathrm{N_{Pb,\ core} = N_{S,\ core} = 4V_{NC}/V_{unit\text{-}cell} = 16/3\pi r^3/a^3} \quad (2.1)$$

where r is the radius of nanocrystal and a is the PbS lattice constant (a = 5.96 Å). We used data in the literature[92, 93] on ligand packing density, n^{-1}, to estimate the number of ligand molecules on a nanocrystal core, N_{ligand}:

$$\mathrm{N_{ligand} = 4\pi r^2 n^{-1}} \qquad (2.2)$$

Equations 2.1 and 2.2 were used to determine $N_{Pb,\ \mathrm{core}}$, $N_{S,\ \mathrm{core}}$, and N_{ligand}. These values were then converted into an overall elemental ratio in the sample via the molecular formula of a given ligand.

We estimated the interparticle distance in our samples using the mass density calculated above, the geometric model shown in Figure S1, and the following equation:

$$\frac{4}{3}\pi\left(r+\frac{d}{2}\right)^3\rho_{NCsolid}/\eta = \frac{4}{3}\pi r^3\rho_{PbS} + m_{ligand} \quad (2.3)$$

The only unknown in the above equation is the interparticle distance, d. The other parameters are known: r is the nanocrystal radius, η is the volume fraction of close-packed spheres in a face-centered cubic lattice (0.74), $\rho_{NCsolid}$ is the mass density of NC solid measured from XRR measurements, ρ_{PbS} is the mass density for bulk PbS, and m_{ligand} is the mass of the ligand shells. We directly estimate the mass of ligand shell by using the ligand molecular weight, M_w, and literature values[92, 93] for the ligand packing density, n^{-1}.

The overall interparticle distance uncertainty primarily originates from the ligand packing density uncertainty. The ligand packing density uncertainty effects the interparticle distance uncertainty in two ways: (i) via the elemental ratio used to determine the mass density of the NC solid (*i.e.* first paragraph in this section) and (ii) via the ligand shell mass used to convert the NC solid mass density into interparticle distance (*i.e.* second paragraph in this section). We varied the ligand packing density by ± 50% in our calculations to gauge how much uncertainty this causes. Varying the ligand packing density by ± 50% led to a $\rho_{NCsolid}$ uncertainty of ~ 10 - 15 % that in turn affects the interparticle distance uncertainty via Equation S3. Varying the ligand packing density by ± 50% also leads to variations in m_{ligand} that introduce an additional ~ 10% uncertainty to the interparticle distance via Equation 2.3. Table 1 summarizes the density and interparticle distance data for our 3.3 nm NC solid samples.

Table 2.1. Densities and interparticle distances of 3.3 nm PbS nanocrystal solids with various ligands.

Nanocrystal Ligand	Density (g/cm^3)	Interparticle Distance (nm)
Oleic Acid (OA)	2.2 ± 0.2	2.2 ± 0.4
Ethanedithiol (EDT)	4.0 ± 0.5	1.1 ± 0.3
Butanedithiol (BDT)	4.2 ± 0.5	1.0 ± 0.3
Hexanedithiol (HDT)	3.4 ± 0.4	1.4 ± 0.3
Octanedithiol (ODT)	3.2 ± 0.4	1.5 ± 0.3
Ethylenediamine (EDA)	4.8 ± 0.5	0.7 ± 0.2

CHAPTER 3

SIZE-DEPENDENT MELTING BEHAVIOR OF COLLOIDAL IN, SN, AND BI NANOCRYSTALS

ABSTRACT

Colloidal nanocrystals are a technologically important class of nanostructures whose phase change properties have been largely unexplored. Here we report on the melting behavior of In, Sn, and Bi nanocrystals dispersed in a polymer matrix. This polymer matrix prevents the nanocrystals from coalescing with one another and enables previously unaccessed observations on the melting behavior of colloidal nanocrystals. We measure the melting temperature, melting enthalpy, and melting entropy of colloidal nanocrystals with diameters of approximately 10 to 20 nm. All of these properties decrease as nanocrystal size decreases, although the depression rate for melting temperature is comparatively slower than that of melting enthalpy and melting entropy. We also observe an elevated melting temperature during the initial melt-freeze cycle that we attribute to surface stabilization from the organic ligands on the nanocrystal surface. Broad endothermic melting valleys and very large supercoolings in our calorimetry data suggest that colloidal nanocrystals exhibit a significant amount of surface pre-melting and low heterogeneous nucleation probabilities during freezing.

Introduction

Colloidal nanocrystals are made via solution-phase chemistry and consist of an inorganic core with organic ligands bound to its surface. Rapid progress in the field of colloidal nanocrystal synthesis[94, 95] has led to their use in numerous applications such as LEDs,[15, 16] optoelectronics,[17, 18] electronics,[19, 20] thermal storage,[55, 56] and thermoelectrics.[57, 58] One potential concern for using colloidal nanocrystals in these applications is that their lower melting temperatures may be incompatible with elevated temperatures during device operation and/or fabrication. It is well known that the melting temperature of nanoparticles decrease as their characteristic size decreases and this phenomenon is commonly referred to as melting point depression.[45, 96-104] However, the vast majority of melting point depression studies focus on a sub-monolayer of nanoparticles prepared by dewetting of a thin film. Nanoparticles prepared via other methods such as ball milling and/or colloidal synthesis are more commonly used and could exhibit different behavior due to variations in structure-property-processing relations. In addition, nanoparticles are often embedded in matrices, which remove the free surface of dewetted nanoparticles and also changes melting behavior.

In this study, we focus on the melting behavior of colloidal nanocrystals whose phase change properties have been largely unexplored. Goldstein *et al.*[98] used transmission electron microscopy (TEM) to measure colloidal nanocrystal melting temperature, but did not measure melting enthalpy. Calorimetry measurements can determine both melting temperature and melting enthalpy, and a few other researchers have used this approach to investigate colloidal nanocrystal melting.[105-108] Unfortunately, extracting size-dependent melting behavior from these experiments is problematic because the colloidal nanocrystals were poorly isolated from one another.[106, 108] This led to nanocrystal coalescence during the calorimetry measurements and manifested itself as a melting temperature that drifted toward bulk values during thermal cycling.[107] In some cases, the nanoscale dimensions of the nanocrystals degraded so fast that bulk melting temperatures were observed during the first melting cycle.[105, 106]

We demonstrate that this nanocrystal coalescence problem can be completely mitigated by isolating the colloidal nanocrystals from one another via dispersion within a polymer matrix. Since colloidal nanocrystals and polymers have similar solubility and are easily mixed in a variety of solvents, this preparation of embedded nanocrystals requires little additional effort. We use polyimide resin (PI resin) for the polymer matrix because it has a glass transition temperature above 305°C. This makes it a suitable matrix for studying the low melting temperature metals in this work. Specifically, we focus on the melting behavior of In, Sn, and Bi nanocrystals whose bulk melting temperatures are 157, 232, and 271°C, respectively. The use of the stabilizing PI resin matrix allows us to observe highly repeatable melting behavior throughout numerous melt-freeze cycles. We show that the colloidal nanocrystal melting temperatures, melting enthalpies, and melting entropies are all size-dependent and decrease as nanocrystal diameter decreases. We also observe an elevated melting temperature during the initial melt-freeze cycle that we attribute to surface stabilization from the nanocrystal's organic ligands. Lastly we observe signatures of surface pre-melting and low heterogeneous nucleation probabilities in our samples that manifest themselves as broad endothermic melting valleys and very large supercooling in the calorimetry data.

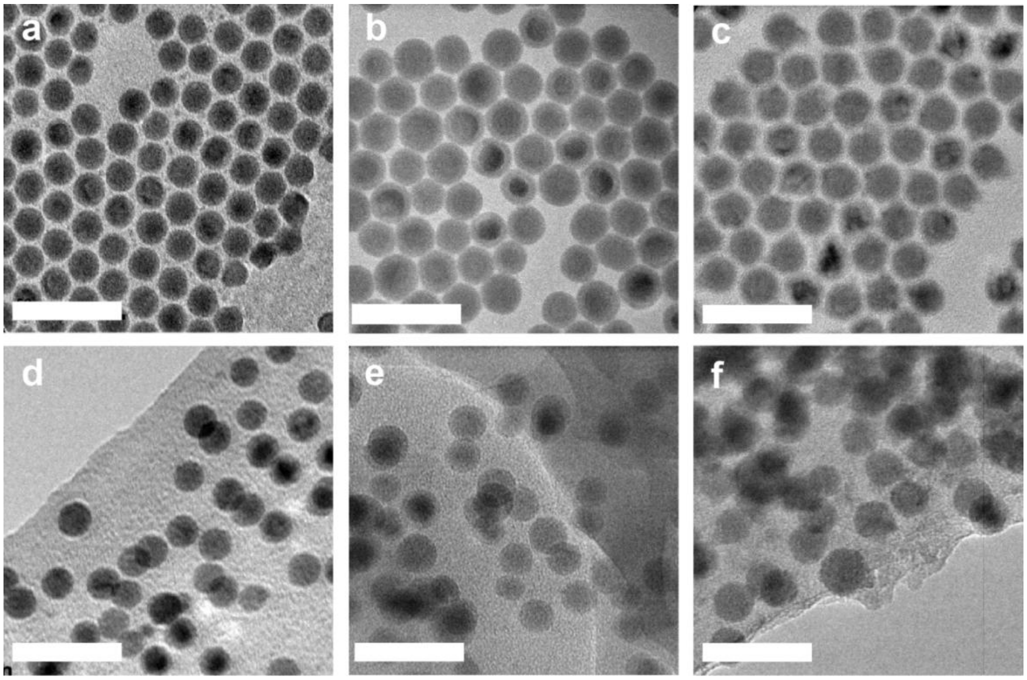

Figure 3.1. Transmission electron microscopy images of (a) 14.9 ± 0.7 nm Bi nanocrystals, (b) 17.0 ± 1.1 nm Sn nanocrystals, and (c) 17.0 ± 1.1 nm In nanocrystals. Corresponding images of the (d) Bi, (e) Sn, and (f) In nanocrystals after dispersion into the polyimide resin matrix illustrate that the size and shape of the nanocrystals are preserved during sample preparation (the scale bar is 50 nm).

Results and Discussion

Melting Temperatures

We prepared our samples by synthesizing colloidal nanocrystals and then dissolving them with PI resin in a shared solvent. We then drop-cast the solution and removed the solvent *via* heating. We synthesized our colloidal nanocrystals using hot-injection techniques reported by Yarema *et al.*,[109-112] and controlled the nanocrystal diameter between ~ 10 and 20 nm by varying the reaction temperature and time. The transmission electron microscope (TEM) images in Figures 3.1a to 1c show the excellent shape and size uniformity of the nanocrystals prepared using this approach. The images in Figures 1d to 1f illustrate that the nanocrystal size and shape are preserved when embedded in the PI resin matrix.

The typical melting behavior of a colloidal nanocrystal sample dispersed in a PI resin matrix is illustrated in Figure 3.2a. This figure shows a DSC measurement on 17 nm Sn nanocrystals that have gone through multiple melt-freeze cycles. An endothermic valley is observed at ~ 200 °C during heating and an exothermic peak is observed at ~ 20 °C during cooling. We attribute the endothermic valley to Sn nanocrystal melting and the exothermic peak to Sn nanocrystal freezing. These assignments are corroborated with a control DSC measurement on pure PI resin, which show no discernable features throughout the entire temperature range. Note that bulk Sn melts at 232°C and so our observed nanocrystal melting temperature is consistent with melting point depression.

We observe an elevated melting temperature during the first melt-freeze cycle and attribute this to surface chemistry effects in colloidal nanocrystals (Figure 3.2b). For example, 17 nm Sn nanocrystals melt at 214 °C during the first cycle and then melt at 204 °C during subsequent cycles. It is well known that melting typically initiates at the surface of a solid, and we postulate that the strongly bound surface ligands of colloidal nanocrystals inhibit melting by stabilizing the surface. Similar surface stabilization behavior has been observed in Pb nanoparticles in Al matrices[113] and Ag nanoparticles in Ni matrices.[114] The lower melting temperatures in subsequent cycles suggest that the ligands detach from the nanocrystal surface during the first cycle and remain detached in subsequent cycles. This increase in initial melting temperature was observed for all of our nanocrystal compositions (In, Sn, and Bi) and diameters (10 – 20 nm), which suggests that this is a widespread characteristic of colloidal nanocrystals.

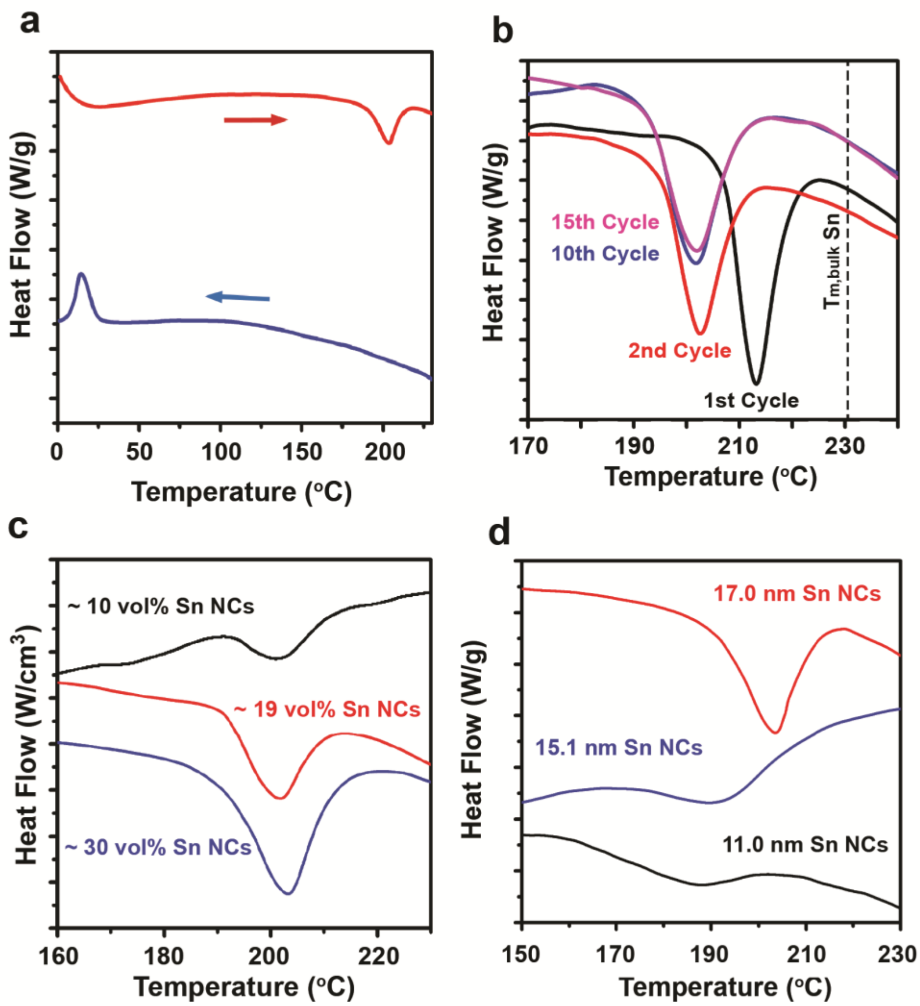

Figure 3.2. (a) A typical heating (red curve) and cooling (blue curve) in a melt-freeze cycle during differential scanning calorimetry (DSC) measurements. This specific sample consists of 17 nm Sn nanocrystals (NCs) dispersed in a polyimide resin matrix. Note that the feature located in the 0 – 25 °C range of the heating curve is a measurement artifact that occurs when the DSC switches from cooling to heating. (b) The endothermic valley

of 17 nm Sn nanocrystals during several different melt-freeze cycles. After the initial melting cycle, a stable and repeatable melting temperature and melting enthalpy are observed. We attribute the elevated melting temperature during the initial cycle to surface stabilization from the organic ligands on the nanocrystal surface. (c) The endothermic valley of 17 nm Sn nanocrystals prepared at varying nanocrystal volume fractions within the polyimide resin matrix. As the nanocrystal volume fraction is changed, the melting enthalpy signature increases proportionately and the melting temperature remains unchanged. (d) The endothermic melting valley for Sn nanocrystals of varying diameters that are embedded in a polyimide resin matrix. As the nanocrystal diameter decreases, both the melting temperature and melting enthalpy decrease. The full-width at half-maximum of the melting valley also increases for smaller nanocrystals.

Our use of a PI resin matrix to isolate nanocrystals from one another prevents nanocrystal coalescence and leads to a repeatable and stable melting temperature after the initial melting cycle (Figure 2b). Prior colloidal nanocrystal calorimetry studies have been prone to nanocrystal coalescence problems due to unsuitable matrices or the absence of matrices.[105-108] Consequently the observed melting temperatures drifted toward the bulk melting temperature during thermal cycling. In some cases, bulk melting temperatures could be observed during the first melting cycle.[105, 106] This transient behavior makes measurements of size-dependent melting in colloidal nanocrystals problematic. This problem is further compounded by the increase in melting temperature observed during the first thermal cycle as described above. In our nanocrystal-PI resin samples, we are able to observe repeatable melting temperatures during thermal cycling up to a nanocrystal volume fraction of ~ 30% (Figure 3.2c). We designate this repeatable temperature as the melting temperature of our nanocrystal samples throughout this paper.

The melting temperature of colloidal Sn, In, and Bi nanocrystals all decrease as nanocrystal diameter decreases (Figure 3.3). In addition to melting temperature data collected with PI resin matrices, this figure also includes melting temperature data from our prior work on Bi nanocrystals in Ag matrices.[55] The melting point depression in the Ag matrix is notably weaker than in the PI resin matrix and highlights the importance of both size and surrounding environment. The melting model proposed by Shi[115] takes into account the effects of both size and matrix on melting and provides an excellent fit to our data. At the heart of Shi's model is the Lindemann criterion,[116] which states that melting occurs when the average root mean square displacement (MSD) of the atoms in a particle exceeds a critical value. Keeping in mind that surface atoms typically have a larger MSD than interior atoms, this criterion readily explains the qualitative size dependence of melting temperature. As the nanocrystal size shrinks, the number of surface atoms increases and therefore the average MSD increases. This increase in average MSD then causes the critical root MSD (i.e. melting) to be reached at lower temperatures.

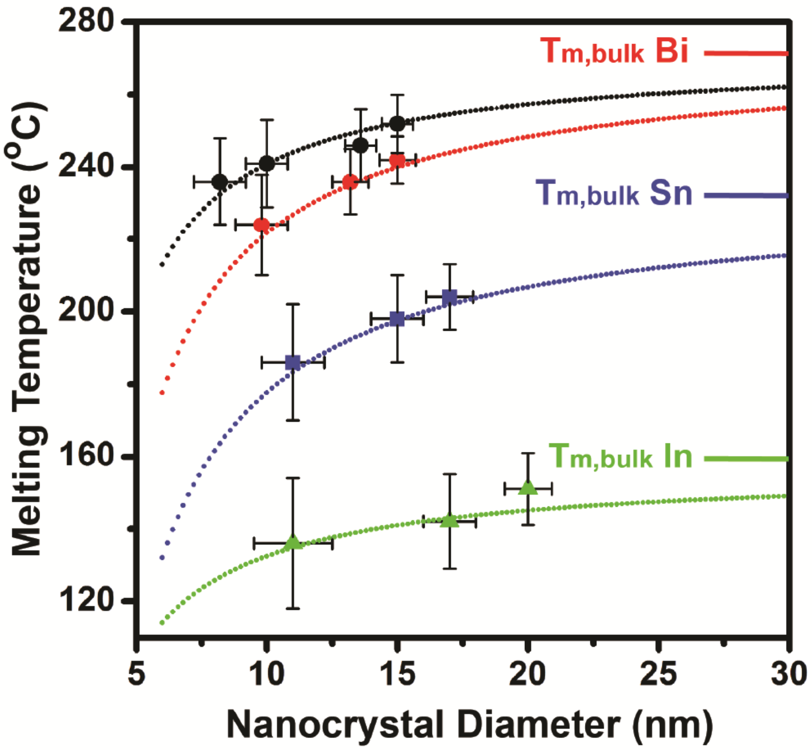

Figure 3.3 The melting temperature of colloidal In, Sn, and Bi nanocrystals as a function of nanocrystal diameter. In addition to data for In, Sn, and Bi in polyimide resin matrices (green triangles, blue squares, and red circles, respectively), this figure also contains data from our prior work on Bi nanocrystals in an Ag matrix (black circles, Reference 55). The melting temperature and melting uncertainty in this figure represent the endothermic valley minimum and endothermic valley full width at half maximum in the DSC data, respectively. The dotted curves are experimental data fits using Shi's melting temperature model that accounts for both nanoparticle size effects and matrix effects [Reference 114].

Shi's melting temperature model[115] expands upon the Lindemann criterion by including matrix effects on the atom MSD and fits our experimental data very well. This matrix effect is captured in Shi's model via the parameter, α, which is the ratio of surface atom MSD to interior atom MSD. The presence of a matrix predominantly affects the MSD of surface atoms and leaves the MSD of interior atoms largely unchanged. Shi's model predicts a size dependent melting temperature, $T_m(r)$, that depends upon particle radius, r, and α:

$$T_m(r) = T_{m,bulk} \exp\left[-(\alpha - 1)\left(\frac{r}{3h} - 1\right)^{-1}\right], \qquad (1)$$

In this expression, h is a characteristic length representing the height of an atomic monolayer on a bulk surface and is estimated from the crystal lattice constant. We obtained reasonable fits to our experimental data on both Sn and In nanocrystals in PI resin with an α value of 1.54. It is intuitive that the same α value can be used to fit both sets of data because their matrices are the same and because Sn and In have the same crystal structure. The α value for Bi nanocrystals in PI resin was 1.42 and differed slightly from Sn and In. We speculate that this slight difference may arise from a difference in crystal structure, and hence a change in the value for h in Equation 1. The α value for Bi nanocrystals in an Ag matrix was 1.2 and indicates that the rigid Ag matrix suppresses MSD comparatively more than the soft PI resin matrix.

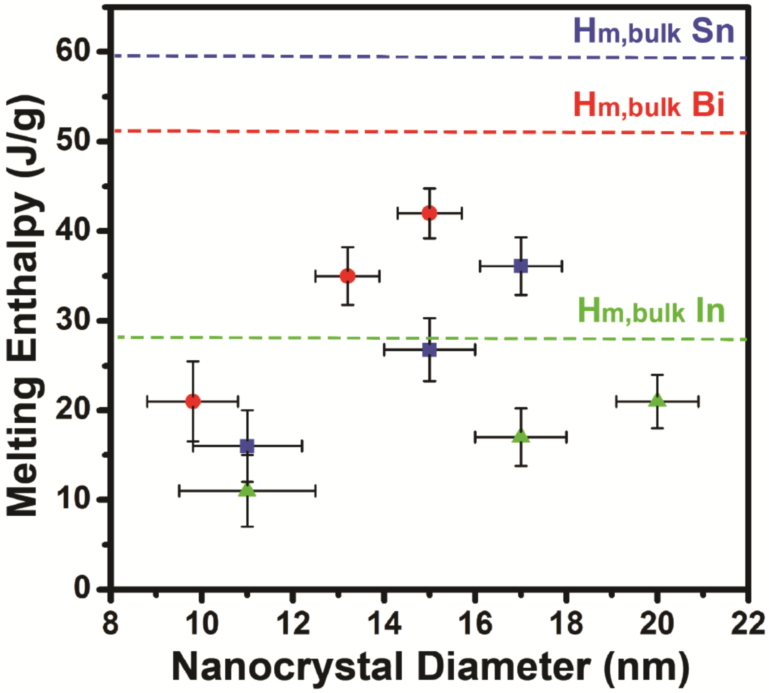

Figure 3.4. The melting enthalpy of colloidal In (green triangles), Sn (blue squares), and Bi (red circles) as a function of nanocrystal diameter. This size-dependent melting enthalpy is a consequence of size- dependence in both melting temperature and melting entropy.

Melting Enthalpies and Entropies

While reports on size-dependent melting temperature are widespread, reports on size-dependent melting enthalpy are relatively limited.[99, 101, 117] One of the primary challenges in measuring size-dependent melting enthalpy stems from the preparation of the experimental sample. Samples for size-dependent melting studies are typically prepared by vapor depositing a thin film on a substrate that subsequently dewets and forms a sub-monolayer of nanoparticles. These samples produce small thermal energy signals during phase change and require sophisticated microfabricated nanocalorimeters to determine their melting enthalpy. [17,19,102]

Our sample preparation embeds a large ensemble of nanoparticles into the PI resin matrix and therefore produces a large thermal signal that can be easily detected using standard calorimeters. However, measuring the mass of our nanoparticles requires additional care due to the structure of colloidal nanocrystals. A direct measurement of colloidal nanocrystal mass would contain mass contributions from both the nanoparticle (i.e. the nanocrystal core) and the surface ligands. To circumvent this problem, we used cyclic DSC measurements to determine the mass ratio of the nanocrystal cores to the nanocrystal ligands. Let us consider the case of colloidal Sn nanocrystals for illustrative purposes. We first prepared a DSC sample consisting of colloidal Sn nanocrystals without a PI resin matrix. We then subjected this sample to multiple melt-freeze cycles, during which the absence of a protective matrix leads to nanocrystal coalescence into a bulk material. Upon observing the bulk melting temperature of Sn, we determined the true mass of Sn in our colloidal nanocrystals by comparing our measured melting enthalpy to the bulk Sn melting enthalpy (59 J/g). We did this measurement for all nanocrystal compositions and sizes because the core:ligand mass ratio depends on both of these parameters.

The melting enthalpy of colloidal Sn, In, and Bi nanocrystals decrease away from their respective bulk values as nanocrystal size is decreased (Figure 3.4). Melting enthalpy, H_m, can be expressed as the product of melting temperature, T_m, and melting entropy, S_m:

$$H_m = T_m S_m \,, \quad (2)$$

Since melting temperature decreases as nanocrystal diameter decreases, a corresponding depression in melting enthalpy is also expected. However, we find that melting entropy also plays a key role as indicated by the fact that the depression rate of melting enthalpy is much faster than that of melting temperature. This trend is revealed in a plot of normalized melting enthalpy depressions, $\mathrm{H_{m,NC}/H_{m,bulk}}$, and normalized melting point depressions, $\mathrm{T_{m,NC}/T_{m,bulk}}$, versus the nanocrystal size (Figure 3.5). For example, nanocrystals with ~ 10 nm diameters have melting temperatures and melting enthalpies that are ~ 90% and ~ 30% of their bulk values.

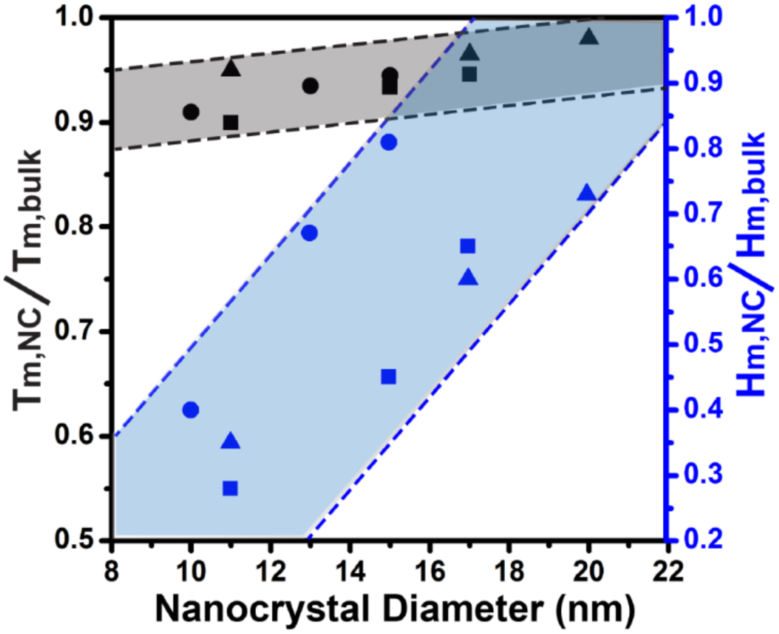

Figure 3.5. The normalized depression in melting temperature (black) and melting enthalpy (blue) as a function of nanocrystal diameter for In (triangles), Sn (squares), and Bi (circles) nanocrystals (NCs). The depression rate for melting enthalpy is significantly faster than the depression rate for melting temperature.

The significant difference in depression rates for melting temperature and melting enthalpy means that melting entropy is also size-dependent and decreases with nanocrystal size. Melting entropy represents the difference between the solid state entropy and liquid state entropy. The entropy of a solid increases as nanoparticle diameter decreases due to the growing fraction of surface atoms, which have larger MSD.[118, 119] This brings the entropy of solid nanoparticles closer to the liquid state entropy and leads to decreasing melting entropy as nanocrystal diameter is reduced. Figure S4 illustrates the entropy size dependence for our colloidal In, Sn, and Bi nanocrystals.

Surface Pre-Melting and Supercooling

Unlike melting in bulk materials, melting in colloidal nanocrystals occurs over a wide finite temperature range (i.e. the melting valley has a large full-width at half-maximum, FWHM). Furthermore, the FWHM increases as nanocrystal diameter decreases (Figure 3.2d). For example, the FWHM of the melting valley for Sn nanocrystals changes from 17 to 30 °C as the nanocrystal diameter shrinks from 17 nm to 11 nm. We also observe similar behavior for Bi and In nanocrystals (Figure S2c and S2d). This behavior is consistent with a phenomenon known as surface pre-melting, during which a thin liquid layer forms on the solid surface at a temperature below the conventionally recognized melting temperature.[99] While this phenomenon has been observed in bulk materials,[120-122] it has little effect on the overall melting behavior because of the extremely small fraction of surface atoms in bulk material. In contrast, nanoparticles have a significant fraction of surface atoms that can produce a much larger surface pre-melting signature. Furthermore, surface curvature enhances surface pre-melting[104, 123, 124] and is another reason that our samples produce large pre-melting signals. To capture the effect of surface pre-melting in the reporting of our size-dependent melting data (Figure 3), we have used the endothermic valley minimum and valley FWHM for the melting temperature and melting temperature uncertainty, respectively.

Another notable feature in the melting of colloidal nanocrystals is that they exhibit a very large amount of supercooling. For example, our 17 nm Sn nanocrystals supercooled by ~180 °C, which is approximately 40% of its melting temperature (204 °C = 477 K). Classical nucleation theory explains supercooling as resulting from the energy barrier associated with the formation of a solid-liquid interface.[125] Supercooling is typically minimized because of energetically favorable heterogeneous nucleation occurs at pre-existing interfaces and/or impurity sites. A large supercooling is regarded as evidence of homogeneous nucleation, and prior experimental efforts to maximize supercooling have found an empirical upper limit of ~ 0.2 – 0.3 T_m.[126-129] One exception to this empirical upper limit is a relatively recent work on Ga nanoparticles.[130] While our In and Bi nanocrystal data exhibited supercoolings of ~ 0.2 – 0.3 T_m, our data on Sn nanocrystals (~ 0.4 T_m) represents a second exception to this empirical upper limit. We believe that the very large supercoolings observed during freezing of our samples are due to a decreased probability of heterogeneous nucleation. The probability for heterogeneous nucleation in our samples is low because colloidal nanocrystals are known to be highly defect- and impurity-free. In fact, the intentionally introduction of impurities (i.e. doping) has been an ongoing challenge for the colloidal nanocrystal community.[131] These large supercooling values also suggest that the amorphous polymer matrix provides a poor heterogeneous nucleation site for crystalline metal.

Conclusion

This systematic study on colloidal nanocrystal melting behavior provides guidance on the phase stability of these materials as they are incorporated into devices that experience elevated temperatures during operation and/or fabrication. Specifically, we have reported the melting temperatures, melting enthalpies, and melting entropies of colloidal In, Sn, and Bi nanocrystals with diameters ranging from 10 – 20 nm. All of these properties decreases as nanocrystal size decreases, although the depression rate for melting temperature is comparatively slower than that of melting enthalpy and melting entropy. We also observed an elevated melting temperature during the initial melting of colloidal nanocrystals and we attribute this to surface stabilization from the nanocrystal's ligands. Broad endothermic melting valleys and very large supercooling in the calorimetry data suggest a significant amount of surface pre-melting and low heterogeneous nucleation probabilities during freezing. These observations on colloidal nanocrystal melting behavior were enabled by our new calorimetry sample preparation technique that prevents nanocrystal coalescence during melt-freeze cycles.

Methods

Sn Nanocrystal Synthesis: Sn nanocrystals were synthesized following the procedure reported by Kravchyk *et al*.[109] In a typical synthesis of 17 nm Sn nanocrystals, 20 g of oleylamine (OLA) was loaded into a three-neck flask and degassed at 140 °C for 2 hours. The flask was then heated to 210 °C, at which point 3 solutions were sequentially injected. The first injection was 0.5 mmol $Sn[N(SiMe_3)_2]_2$ dissolved in 1 mL octadecane. The second injection was 3.6 mmol $LiN(SiMe_3)_2$ dissolved in 2 mL of toluene and was injected immediately after the first injection. After 10 s, 0.6 mL of 1 M lithium triethylborohydride in tetrahydrofuan (THF) was injected, and the solution immediately turned dark. The reaction temperature was then maintained for 1 hour and then quickly cooled to room temperature using an ice bath. This reaction yields Sn nanocrystals with OLA ligands. The OLA ligands were then exchanged with oleic acid (OA) to improve nanocrystal stability. Adjusting injection temperature and growth time allows control over the nanocrystal diameter. The Sn nanocrystals were isolated from the reaction mixture by precipitating in ethanol and redispersing in a nonpolar solvent. This isolation process was repeated two additional times and the nanocrystals were dispersed in THF after the final precipitation.

In Precursor Synthesis and In Nanocrystal Synthesis: In nanocrystals were synthesized using the procedure reported by Yarema *et al.*[111] The first step in this synthesis is to create the In precursor, which is $In[N(SiMe_3)_2]_3$. To synthesize $In[N(SiMe_3)_2]_3$, 6.6 mmol of $InCl_3$ and 20 mmol of $LiN(SiMe_3)_2$ were reacted in 120 mL diethyl ether at 60 °C for 24 hours.[111] The reaction mixture was filtered through a PTFE filter and then dried under vacuum to yield a pale yellow powder. The $In[N(SiMe_3)_2]_3$ powder was then dissolved in 15 mL of pentane, filtered, and dried again under vacuum. For In nanocrystal synthesis, 20 g of hexadecylamine (HDA) was degassed at 100 °C for 2 hours and then heated to 200 °C. Once the temperature stabilized at 200 °C, a solution of 0.26 g $In[N(SiMe_3)_2]_3$ and 0.728 g $LiN(SiMe_3)_2$ dissolved in 8 mL toluene was injected. The reaction temperature was then cooled to ~ 155 °C, at which point 0.1 mL of 1 M lithium triethylborohydride in THF was injected. Depending on the desired nanocrystal diameter, the reaction temperature was maintained for an additional 1 – 5 minutes. The reaction mixture was then cooled using a water bath. 20 mL of toluene was added to the mixture during the cooling process to prevent the solidification of HDA. This synthesis results in In nanocrystals with HDA ligands. We exchanged these HDA ligands with OA right after synthesis to promote stability of the nanocrystal solution. The In nanocrystals were isolated from the reaction mixture using precipitation techniques in a similar manner to the Sn nanocrystals.

Bi Precursor Synthesis and Bi Nanocrystal Synthesis: $Bi[N(SiMe_3)_2]_3$ was used as the nanocrystal precursor for Bi nanocrystals. This precursor was synthesized via a metathesis reaction between $BiCl_3$ and $LiN(SiMe_3)_2$ as reported by Yarema et al.[110] In a typical synthesis, 6.6 mmol $BiCl_3$ and 20 mmol $LiN(SiMe_3)_2$ were dissolved in 80 mL diethyl ether and 10 mL THF. This reaction was vigorously stirred and maintained at 0 °C for 2 hours. Upon reaction completion, white precipitates of LiCl were filtered from the mixture by a PTFE filter and the resulting solution was dried under vacuum. The resulting $Bi[N(SiMe_3)_2]_3$ powder was then dissolved in 15 mL pentane, filtered, and again dried under vacuum. In a typical Bi nanocrystal synthesis, 20 g of HDA was degassed at 100 °C for 2 hours and then heated to 130 °C. 0.1 mL lithium triethylborohydride in THF was then injected. After 15 s, a solution of co-dissolved 0.14 g $Bi[N(SiMe_3)_2]_3$ and 0.17 g $Li[N(SiMe_3)_2]$ in 2 mL toluene was injected. After 15 s, the reaction was then stopped by cooling in a water bath. 20 mL of toluene was typically added during cooling to prevent the HDA from solidifying. This synthesis results in Bi nanocrystals with HDA ligands. We exchanged these HDA ligands with OA right after synthesis to promote stability of the nanocrystal solution. Adjusting injection temperature allows control over the nanocrystal diameter. The Bi nanocrystals were isolated from the reaction mixture using precipitation techniques in a similar manner to the Sn nanocrystals.

Nanocrystal – PI Resin Sample Preparation: The dispersion of nanocrystals was completed using a three-step approach. First, the nanocrystals were synthesized as described above. In parallel, PI resin was dissolved in THF in a separate vial by stirring for 30 minutes. Then, an appropriate amount of nanocrystal solution and PI resin were mixed and stirred for 2 hours. The samples were then made by drop-casting the combined solution onto appropriate substrates. The nanocrystal composition and size were controlled at the nanocrystal synthesis step and nanocrystal volume fraction was controlled at the mixing step.

Transmission Electron Microscopy (*TEM*)*:* To characterize the morphology of the nanocrystal samples, TEM (FEI Tecnai F20) was used and operated at 200 kV. The nanocrystal samples were made by drop-casting a dilute nanocrystal dispersion onto a carbon film coated copper TEM grid. The diameter of the nanocrystals was determined by statistical analysis of TEM images containing ~ 100 nanocrystals using ImageJ. The standard deviation of the nanocrystal diameters was used for the diameter uncertainties. The TEM samples of the nanocrystals dispersed in PI resin were prepared by drop-casting dilute combined solutions onto SiN_X window.

Differential Scanning Calorimetry (*DSC*)*:* DSC measurements were carried out using a standard differential scanning calorimeter (TA Q20). To prepare samples for DSC measurements, we drop-cast the combined solution into an aluminum DSC pan, and then heated it at 50 °C and 100 °C sequentially to remove the solvent. DSC measurements were carried out by cyclic heating and cooling at a rate of 10 °C/min. We also conducted control experiments at varying temperature scan rates of 2 – 10 °C/min and observed no effects of this parameter on the DSC signal (Figure S5). The temperature cycling range was 0 to 250 °C for Sn, 0 to 300 °C for Bi, and 0 to 200 °C for In. During these measurements, a nitrogen atmosphere was maintained using a flow rate of 50 mL/min. The DSC data was analyzed using the software provided by TA instruments.

CHAPTER 4

PHASE CHANGE NANOCOMPOSITES WITH TUNABLE MELTING TEMPERATURE AND THERMAL ENERGY DENSITY

ABSTRACT

Size-dependent melting decouples melting temperature from chemical composition and provides a new design variable for phase change material applications. To demonstrate this potential, we create nanocomposites that consist of a monodisperse ensemble of Bi nanoparticles (NPs) embedded in a polyimide (PI) resin matrix. In this composite, the Bi NPs operate as the phase change component whereas the PI resin matrix prevents nanoparticle coalescence during melting. Benefits from the matrix, our experimental results have shown that the Bi NPs are preserved after 60 melt-freeze cycles. By varying nanoparticle diameters, we successfully tuned the composite's melting temperature from 218 to 240 °C. Hence it is possible to leverage size effects to tune phase change temperature and energy density in phase change materials.

The origins of size-dependent melting arise from the increasing surface to volume ratio as a material's characteristic length decreases.[44, 45, 132-135] This size effect has been studied for over a century, starting with the theoretical work by Pawlow[42] and the experimental observation done by Takagi.[47] Buffet and Borel later used scanning electron diffraction to demonstrate that the melting temperature of gold can be varied by as much as ~ 500 °C.[96] Their data and thermodynamic model indicate that the melting temperature of nanoparticles depends inversely on nanoparticle diameter. This size-dependent melting phenomenon has since become known as melting point depression. Several other models and simulation results have since been conducted[44, 45, 115, 136, 137] and many other experimental observations have been reported: particles have been melted on substrate surfaces,[103, 138, 139] inside crystalline materials[114, 140, 141] and inside amorphous materials.[142-146] Lai *et al.*[99] used nanocalorimetry measurements to show that a decrease in enthalpy of fusion also accompanies melting point depression.

While numerous efforts have been devoted to fundamentally understanding nanoparticle's melting, its application side is absent. There are two challenges to leverage this size effect to applications. First, the majority of research on melting point depression largely focuses on nanoparticles formed via dewetting of vapor-deposited metals on substrates. While this production approach is sufficient for fundamental studies, it has limited value for practical applications. Technological applications that leverage melting point depression will simultaneously require scalable nanoparticle synthesis, particle size distribution control, and particle stability. Scalable nanoparticle syntheses such as ball milling[147], melt spinning[142, 146, 148, 149] and ion implantation[141, 143] have been used, but yield broad particle size distributions and consequently poor control over melting characteristics. Secondly, it is important to isolate the particles from one another to prevent coalescence and preserve size-effects over numerous melt-freeze cycles. Lacking a matrix possessed a greater thermal stability, the nanoparticles will coalescence and turn into a bulk material during melting.

To demonstrate a new approach to these challenges, we use solution-phase chemistry to create nanocomposites consisting of monodisperse Bi NPs dispersed in a PI resin matrix.

Solution-phase synthesis of colloidal NPs presents a scalable production approach that exhibits excellent control over NP size, shape, and composition.[150-152] The PI resin matrix was chosen to prevent NP coalescence during melt-freeze cycles because it is a thermoplastic polymer with a glass transition temperature above the Bi melting temperature. The nanocomposites were made using a simple three-step approach: (a) synthesis of colloidal Bi NPs, (b) co-dissolution of Bi NPs and PI resin into a shared solvent, and (c) drop-casting onto an appropriate substrate. Adjusting the reaction conditions of the NP synthesis enabled control over NP size. Varying the ratio of NPs to PI resin in the shared solvent allows control over the composite's NP volume fraction. The monodisperse NPs produced by this approach can be seen in Figures 4.1a and 4.1c, which show a transmission electron microscope (TEM) image and x-ray diffraction (XRD) pattern of typical Bi NPs. Figure 4.1b is a TEM image of the nanocomposite formed by combining the Bi NPs with PI resin. This modular sample preparation approach enables melting-point depression studies in 3-dimensional composites with carefully controlled nanoparticle size, shape, and composition. This approach also has the practical advantage of producing sample quantities large enough to be studied with a standard differential scanning calorimeter (DSC). This circumvents the necessity of highly sophisticated *in situ* electron microscopy melting and microfabricated nanocalorimeter methods, which have been the standard melting point depression research tools.[45, 97, 99, 135, 138, 139, 143]

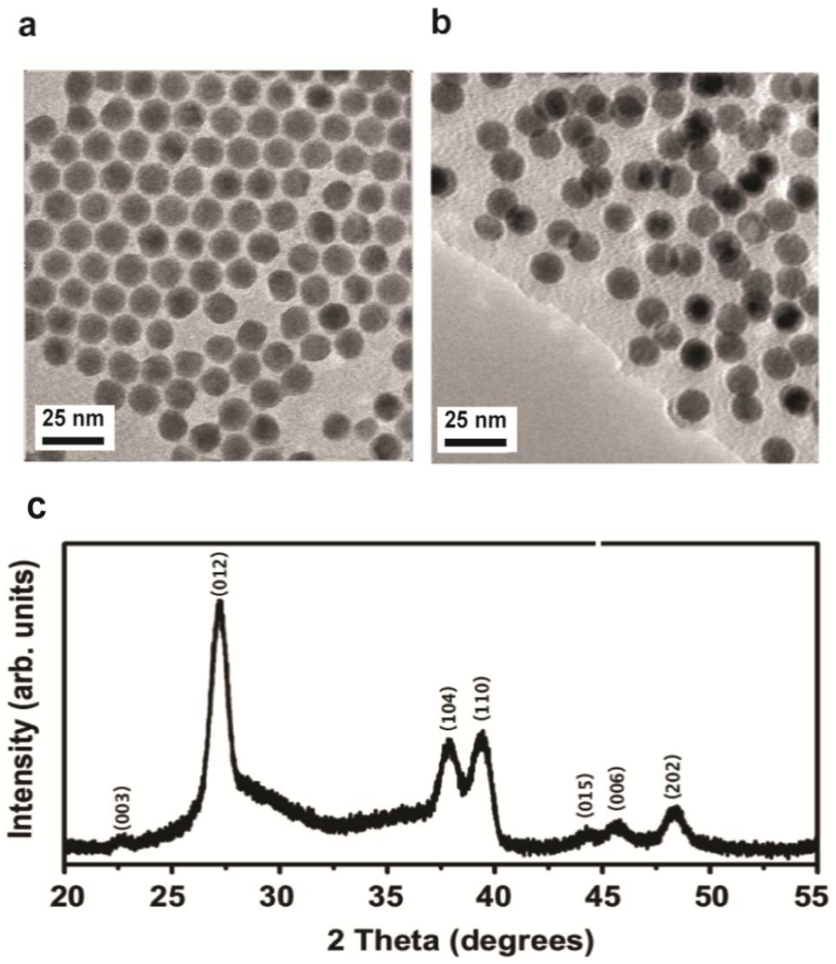

Figure 4.1. (a) TEM image of Bi NPs with 14.5 nm diameter. (b) TEM image of a nanocomposite consisting of a PI resin matrix with embedded 14.5 nm diameter Bi NPs. The backgrounds in the top-right and bottom-left of the image correspond to PI resin and vacuum, respectively. (c) XRD pattern of 14.7 nm Bi NPs.

The Bi NPs were prepared by reducing $Bi[N(SiMe_3)_2]_3$ with hexadecylamine in the presence of $Li[N(SiMe_3)_2]$ and $Li(Et_3BH)$ as described by Yarema et al.[153] Varying the reaction temperature and amount of $Li(Et_3BH)$ allowed control over NP size. The NPs were cleaned by precipitating in ethanol several times and then dissolved in tetrahydrofuran (THF). The NPs produced in this synthesis consist of a Bi core with organic ligands that bind to the surface and act as a surfactant. To measure the true Bi-content of the NP solution (as opposed to the combined content of the Bi and ligands), we used a DSC method. In brief, a sample of NPs were drop-cast into a DSC pan and then subjected to multiple melt-freeze cycles. During this process, the NPs coalesce into a bulk material because the organic ligands are insufficient at isolating the NPs from one another. Consequently a melting valley at the bulk Bi melting temperature (271°C) is observed. The Bi mass was determined by comparing this valley to the enthalpy of fusion for bulk Bi (51.9 J/g). To make the nanocomposite, PI resin was dissolved in THF in a separate container. Appropriate amounts of the NP solution and PI resin solution were then combined and drop-cast into a DSC pan. DSC measurements were carried out by cyclic heating and cooling between 0 °C and 300 °C at a rate 10 °C/min.

Figure 4.2a shows a typical heating and cooling cycle of a nanocomposite containing Bi NPs with 9.6 nm diameters. One endothermic valley and two exothermic peaks are observed during heating and cooling, respectively. We attribute the endothermic valley to NP melting. As expected this occurs well below the bulk melting temperature of Bi, which is 271 °C. The two exothermic peaks during cooling are attributed to two separate freezing events because the total energy released at these temperatures is equivalent to the energy absorbed during melting. These freezing events occur below the melting temperature, which is a common phenomenon known as supercooling. These melting and freezing assignments in the DSC data are corroborated by control measurements on pure PI resin, which showed no discernable features throughout the 0 – 300 °C temperature range.

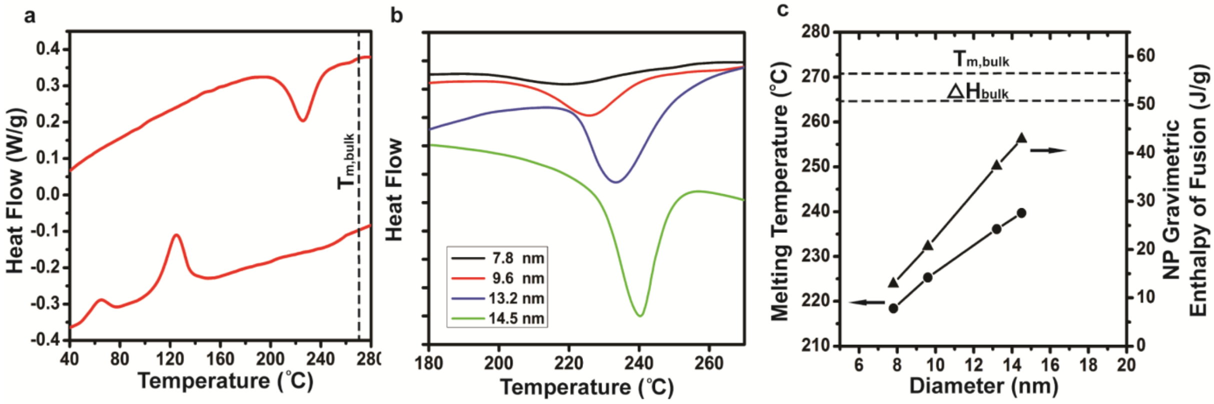

Figure 4.2. (a) A heating and cooling DSC cycle for a composite with Bi NPs of 9.6 nm diameter. (b) The endothermic melting valley during DSC measurements for composites with Bi NPs of four different diameters. For clarity, the data in part (b) has been offset along the vertical axis. Each tick mark represents 0.1 W/g. (c) Size dependent melting temperature (circles) and enthalpy of fusion (triangles) for nanocomposites with Bi NPs of four different diameters.

One major benefit of using nanoparticles for phase change applications is that their melting temperature can be tuned independently of their chemical composition. We demonstrate this by examining composites with Bi volume fractions of ~ 9.0 – 9.5%, but varying NP diameters: 7.8 ± 0.5, 9.6 ± 0.5, 13.2 ± 0.7, and 14.5 ± 0.6 nm. As the NP diameter was varied from 14.5 to 7.8 nm, the melting temperature varied from 239.7 to 218.4 °C (Figure 4.2b,c). Our observations indicate that the NP diameter and melting temperature are inversely proportional, which is in agreement with prior work.[96, 97] Studies by Lai *et al*[99] have previously shown that a decrease in enthalpy of fusion accompanies melting point depression. Due to the small NP signal, their studies required specialized microfabricated nanocalorimeters.[99] Since our NP synthesis approach produces large quantities of monodisperse particles, we are able to make this size-dependent enthalpy of fusion observation using a standard DSC. As the NP diameter varied from 14.5 to 7.8 nm, the NP enthalpy of fusion changed from 42.1 to 12.9 J/g. For clarity we now note that this communication refers to two different enthalpies of fusion throughout its text. The first is the NP gravimetric enthalpy of fusion, which corresponds only to the mass of the composite's Bi component. The second is the composite's volumetric enthalpy of fusion, which corresponds to the combined volume of the Bi and PI resin.

For practical applications, it may be desirable to tune the composite's enthalpy of fusion independently of melting temperature. To demonstrate this capability, we created composites with Bi NPs of 14.7 ± 0.5 nm diameter and varied the Bi volume fraction from 5.3% to 19.8%. As the volume fraction increased, the composite volumetric enthalpy of fusion increased proportionately and no discernable effect on melting temperature is observed (Figure 4.3). This volume fraction design variable enables the composite's melting temperature and enthalpy of fusion to be independently controlled by a simple two-step process. First, the NP size is chosen to yield the desired melting temperature. Second, the Bi volume fraction is chosen to yield the desired composite volumetric enthalpy of fusion. The Bi volume fraction can be successfully increased to ~ 30%, however at ~ 41% bulk melting characteristics developed during thermal cycling. Hence this represents an upper limit on the Bi volume fraction for which the PI resin matrix no longer prevents NP coalescence.

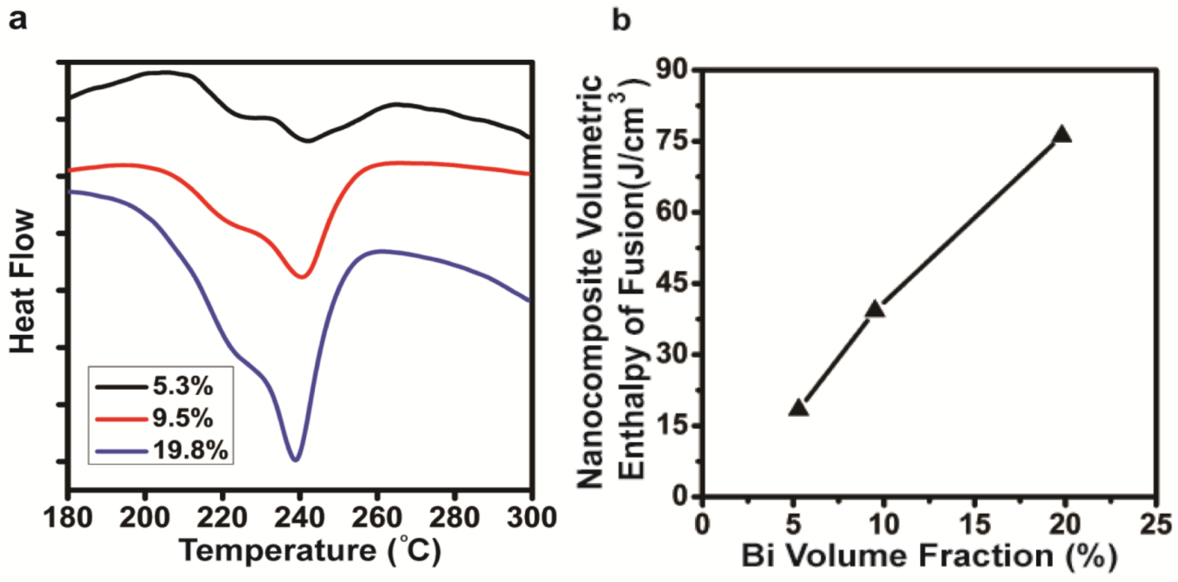

Figure 4.3. (a) The endothermic melting valley during DSC measurements for composites with 14.7 nm diameter NPs and varying Bi volume fraction. For clarity, the data in part (a) has been offset along the vertical axis. Each tick mark represents 0.1 W/cm^3. (b) The composite's volumetric enthalpy of fusion for varying Bi volume fractions.

Numerous melt-freeze cycles conducted on the nanocomposites demonstrate that the PI resin matrix is effective at preventing nanoparticle coalescence, which indicates that this approach could be used for technological applications. Despite subjecting the nanocomposite to 60 melt-freeze cycles, no notable changes in melting temperature or enthalpy of fusion were observed (Figure 4.4). This is in stark contrast to previous literature results in which bulk-like behavior can even be observed during the first thermal cycle.[105, 154] We note that while the PI resin matrix was sufficient at preventing nanoparticle coalescence, it was not sufficient at preventing oxidation. The Bi NPs in the nanocomposite slowly oxidized over a period of weeks under ambient conditions. This can be addressed by choosing alternative matrix materials. Unlike previous experiments that use composites with polydisperse nanoparticles and ill-defined melting temperatures, these experiments demonstrate the feasibility of creating composites with monodisperse nanoparticles and well-defined melting temperature.

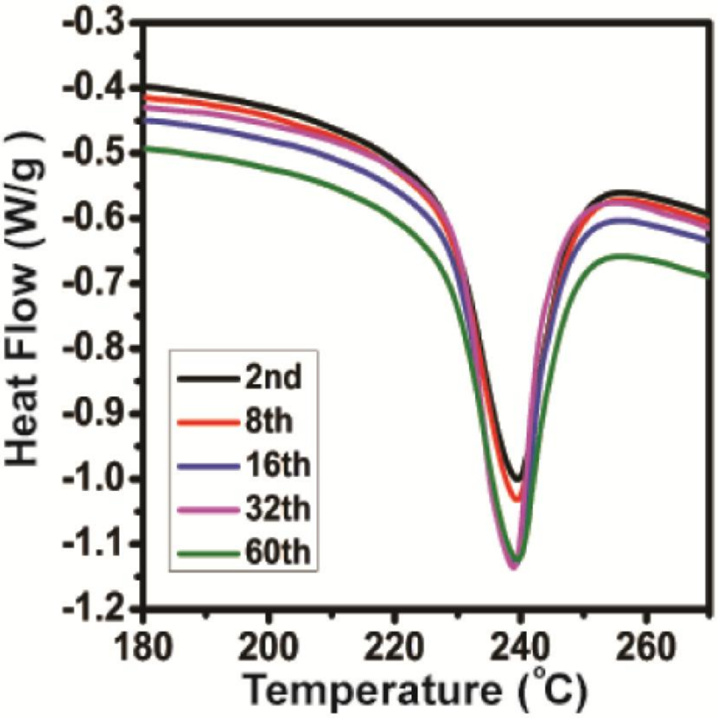

Figure 4.4. Several representative heating cycles during cyclic DSC measurements on a composite with 14.5 nm Bi NPs.

One application where these nanocomposites could excel is as a phase change material for thermal energy storage and thermal management. Latent heat is commonly used to store thermal energy because enthalpies of fusion are typically on the order of 10^2 °C of sensible heat. In the low temperature regime (< 80 °C), paraffin is commonly used for latent heat storage. One of paraffin's attractive qualities is that its melting temperature can be tuned, which is typically difficult with conventional materials. As the length of the paraffin's carbon chain is decreased, its melting temperature decreases. In this respect, the Bi NP diameter plays a similar role to paraffin length. Furthermore, melting point depression is a general phenomenon and we see no reason why this nanocomposite approach cannot be generalized to other NP compositions. Hence NPs can provide thermal storage functionality and flexibility at temperatures above 80 °C where paraffin is not a viable option. In addition to accessing a temperature regime unattainable to paraffin, these composites also benefit from high volumetric enthalpies of fusion. For example, the nanocomposite with a 19.8% volume fraction of 14.7 nm NPs has a volumetric enthalpy of fusion that is ~100% greater than a typical paraffin such as RT60 (76 J/cm^3 vs. 37 J/cm^3).[155]

Conclusion

To conclude, this work demonstrates that polymer matrices can stabilize cyclic melting of NP ensembles and enable melting point depression studies in composites with carefully controlled nanoparticle size. This stabilized melting point depression also creates possibilities for applications in phase change materials. For example, engineered thermal storage materials should be possible because melting temperature can be tuned by varying nanoparticle size.

CHAPTER 5

METAL MATRIX – METAL NANOPARTICLE COMPOSITES WITH TUNABLE MELTING TEMPERATURE AND HIGH THERMAL CONDUCTIVITY FOR PHASE CHANGE THERMAL STORAGE

ABSTRACT

Phase change materials (PCMs) are of broad interest for thermal storage and management applications. For energy dense storage with fast thermal charging/discharging rates, a PCM should have a suitable melting temperature, large enthalpy of fusion, and high thermal conductivity. To simultaneously accomplish these traits, we custom design nanocomposites consisting of phase change Bi nanoparticles embedded in an Ag matrix. We precisely control nanoparticle size, shape, and volume fraction in the composite by separating the nanoparticle synthesis and nanocomposite formation steps. We demonstrate a 50 – 100% thermal energy density improvement relative to common organic PCMs with equivalent volume fraction. We also tune melting temperature from 236 – 252°C by varying nanoparticle diameter from 8.1 – 14.9 nm. Importantly, the silver matrix successfully prevents nanoparticle coalescence and no melting changes are observed during 100 melt-freeze cycles. The nanocomposite's Ag matrix also leads to very high thermal conductivities. For example, the thermal conductivity of a composite with a 10% volume fraction of 13 nm Bi nanoparticles is 128 ± 23 W/m-K, which is several orders of magnitude higher than typical thermal storage materials. We complement these measurements with calculations using a modified effective medium

approximation for nanoscale thermal transport. These calculations predict that the thermal conductivity of composite's with 13 nm Bi nanoparticles varies from 142 to 47 W/m-K as the nanoparticle volume fraction changes from 10 to 35%. Larger nanoparticle diameters and/or smaller nanoparticle volume fractions lead to larger thermal conductivities.

Latent heat thermal storage systems utilize the solid-liquid transition of phase change materials (PCMs) to store thermal energy. This results in much higher energy densities than commonly used sensible heat thermal storage systems and in turn leads to both material and space savings.[156-158] For instance, the latent heat of ice is equivalent to 80 degrees of sensible heat in water. Nevertheless, challenges exist for employing PCMs for effective latent heat thermal storage in varying environmental conditions. Commercially used PCMs are mostly organics and salt hydrates, which are limited to applications from 10 °C – 120 °C.[159] This is suitable for thermal management of buildings[160] and typical electronics,[161] but is mismatched for higher temperature applications such as industrial process heat,[162] power electronics thermal management,[163] and concentrated solar thermal power plants.[164] Latent heat storage at elevated temperatures has been generally restricted to phase change salts in lab settings,[165] whereas industrial practice instead focuses on molten salts for sensible heat storage.[164, 166] However, salts are prone to corrosion problems and also suffer from low thermal conductivity, which in turn leads to slow thermal charging/discharging rates. In fact, this issue of low thermal conductivity is common to thermal storage materials in general.[167-169] The thermal conductivities of organic PCMs and salt hydrates range from ~ 0.1 – 1 W/m-K,[159] and the thermal conductivity of salts range from ~ 0.5 – 5 W/m-K.[165]

Previous efforts to improve the thermal conductivity of PCMs have focused on the use of thermally conductive filler materials (*e.g.* graphite,[170] metallic nanoparticles,[171] and carbon nanotubes[172]) or foams (*e.g.* graphite and metal). While fillers are easy to implement, thermal conductivity enhancements are unfortunately limited because the fillers do not form a continuous structure and the thermal interface resistance between the PCM and fillers is non-negligible. To overcome this problem, many researchers infiltrate PCM into thermally conductive foams (*i.e.* metal foam[173] and graphite foam[174]), which have a continuous structure and leads to better thermal conductivity improvements. For example, a recent study using a graphite foam – paraffin wax composite demonstrated a thermal conductivity of 3.6 W/m-K, which is a 18-fold improvement over paraffin.[167] The use of foams has been demonstrated for many low melting temperature organic PCMs, however this technique is problematic for high melting temperature PCMs (*e.g.* salt) due to difficulties with the infiltration process and corrosivity.[175]

To find a PCM that has high thermal conductivity, high melting temperature, and large enthalpy of fusion, we turned our focus to metallic materials. Metals have excellent thermal conductivities ranging from ~ 10 – 400 W/m-K and a broad range of melting temperatures ranging from -40 °C to over 3000 °C. Relative to other PCMs, metals have received little attention primarily due to their weight (*i.e.* poor gravimetric energy density).[156, 169] While gravimetric energy density is important for mobile applications, many thermal storage applications are stationary, and in these cases volumetric energy density is of more importance. Hence metallic PCMs could find applications in buildings thermal management, industrial process heat, and concentrated solar thermal power plants.

In this paper, we propose the use of composites that consist of phase change metallic inclusions distributed in a metal matrix. The phase change inclusions provide the desired melting temperature and high volumetric energy density, whereas the matrix provides excellent thermal transport and mechanical strength when the inclusions melt. Furthermore, we explore the use of phase change nanoparticle inclusions as opposed to phase change macroparticle inclusions. The choice of nanoparticles is motivated by the use of size-dependent melting as a new PCM design tool. Size-dependent melting is a commonly-observed phenomenon in nanostructures and was first predicted by Pawlow.[176] Substantial theoretical and experimental efforts have since been devoted to explaining the relation between nanoparticle diameter and melting temperature.[96, 98, 103, 106, 177-179] These fundamental studies inspired us to develop nanoparticle-based PCMs for application purposes.

We demonstrate this nanoparticle-based PCM concept by creating composites consisting of phase change Bi nanoparticles embedded in an Ag matrix. We first present a solution-phase approach to embed high-quality colloidal Bi nanoparticles into a bulk Ag matrix. This approach separates the nanoparticle synthesis and composite formation steps, thereby enabling excellent control over nanoparticle morphology and volume fraction. This in turn permits control over the composite's melting temperature and energy density. We investigate the composite's thermal storage performance by using cyclic differential scanning calorimetry (DSC). Our composite's energy density is 50 – 100% better than composites containing an equivalent volume fraction of typical organic PCMs. Furthermore, varying the Bi nanoparticle diameter tunes the nanocomposite's melting temperature from 236 – 252 °C. Importantly, these DSC measurements also demonstrate that the silver matrix offers effective protection against coalescence of the Bi nanoparticles during melt-freeze cycles. The Ag matrix also greatly improves thermal transport in the nanocomposite. Thermal conductivity measurements using the Wiedemann-Franz law[180] demonstrate that our nanocomposite's thermal conductivity is several orders of magnitude better than typical thermal storage materials. We also employ a modified effective medium approximation (EMA) for nanoscale thermal transport to calculate the composite thermal conductivity over a broad range of nanoparticle diameters and volume fractions.

Results and discussion

Metal Matrix – Metal Nanoparticle Composite Synthesis

The nanocomposite was prepared by a simple three-step approach: (a) synthesis of colloidal Bi nanoparticles, (b) co-dissolution of Bi nanoparticles and Ag precursor in a solvent mixture, and (c) heating to thermally decompose the Ag precursor into an Ag matrix. This three-step nanocomposite approach enables independent control of nanoparticle size, shape, and volume fraction by using a modular technique that separates nanoparticle synthesis from nanocomposite formation. Nanoparticle size and shape are controlled by step (a) whereas nanoparticle volume fraction is controlled by step (b). The formation of the metal matrix - metal nanoparticle composite occurs in the last step, during which the Ag precursor thermally decomposes into an Ag matrix that encapsulates the Bi nanoparticles.

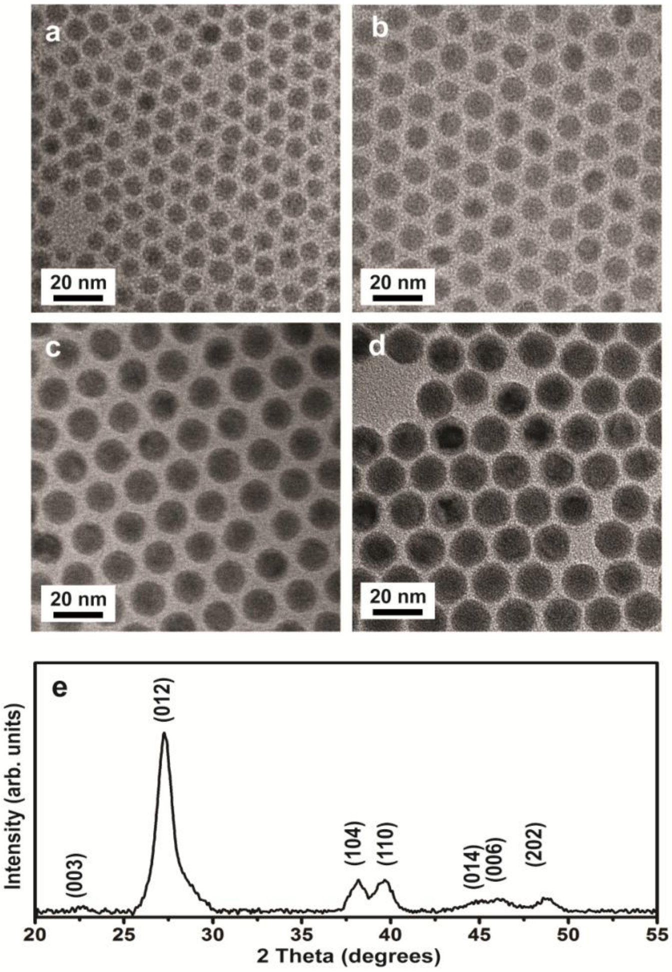

Figure 5.1. Transmission electron microscopy images of the Bi nanoparticles used to create the Ag matrix – Bi nanoparticle composites. The nanoparticle diameters are (a) 8.1±1.0 nm, (b) 9.8 ± 0.8 nm, (c) 13.2 ± 0.6 nm and (d) 14.9 ± 0.6 nm. (e) X-ray diffraction pattern of Bi nanoparticles with 13.6 nm diameter.

The Bi nanoparticles were prepared by a hot injection technique reported by Yarema *et al.*[110] In brief, Bi[N(SiMe$_3$)$_2$]$_3$ was used as a Bi precursor and reduced by hexadecylamine at a elevated temperature. Size variation was achieved by varying the reaction temperature from 115 to 140 °C. This synthesis yields Bi nanoparticles with surface-bound hexadecylamine ligands. In order to improve colloidal nanoparticle stability, the hexadecylamine ligands were exchanged with oleic acid ligands post-synthesis. Figure 5.1 illustrates the high quality Bi nanoparticles prepared by this approach, which exhibit spherical shape, excellent size control, and narrow size distribution.

We used silver benzoate as the precursor to create the nanocomposite's Ag matrix. Silver benzoate is an organic silver salt with good solubility in amine solvents and is a well-known silver precursor.[181, 182] Thermogravimetric analysis was employed to identify appropriate conditions for decomposing this precursor. A temperature ramp of 2 °C/min was performed from room temperature to 300 °C, where the sample was kept isothermal for 2 hours and then resumed up to 350 °C. As Figure 2a shows, after the isotherm process at 300 °C, the mass reached its final value of ~ 47% and no further decrease in mass was observed. This mass ratio indicates that the final product is Ag and this conclusion is further corroborated by x-ray diffraction measurements (Figure 5.2b). Together, these results indicate that 300 °C is sufficient to fully decompose the silver benzoate.

Prior to nanocomposite formation, the Bi nanoparticles and silver benzoate were mixed in an appropriate ratio to yield the desired nanoparticle volume fraction. We note that this step is sensitive to solvent choice because the Bi nanoparticles prefer nonpolar solvents whereas the silver benzoate prefers mildly polar solvents. We addressed this issue by choosing a miscible solvent pair and controlling the concentration of Bi nanoparticles and silver benzoate. Prior to mixing, the Bi nanoparticles were suspended in toluene at ~ 1 mg/mL and the silver benzoate was dissolved in pyridine at ~ 2 mg/mL. The Bi nanoparticle suspension and silver benzoate solution were then combined, stirred for 2 hours, and used promptly. If not used promptly, partial precipitation could be observed the following day. We also chose toluene and pyridine as the miscible solvent pair because of their similar boiling temperatures, which should help prevent phase segregation as the solvent evaporates during the nanocomposite formation step. We note that since pyridine is a known ligand for colloidial nanocrystals,[183, 184] a potential for ligand exchange between oleic acid and pyridine exists during this step. However, we do not believe ligand exchange occurs because the Bi nanoparticles with oleic acid ligands are insoluble in pyridine. Had a ligand exchange occurred, the Bi nanoparticles should be soluble in pyridine and our use of a pyridine-toluene solvent pair would be unnecessary.

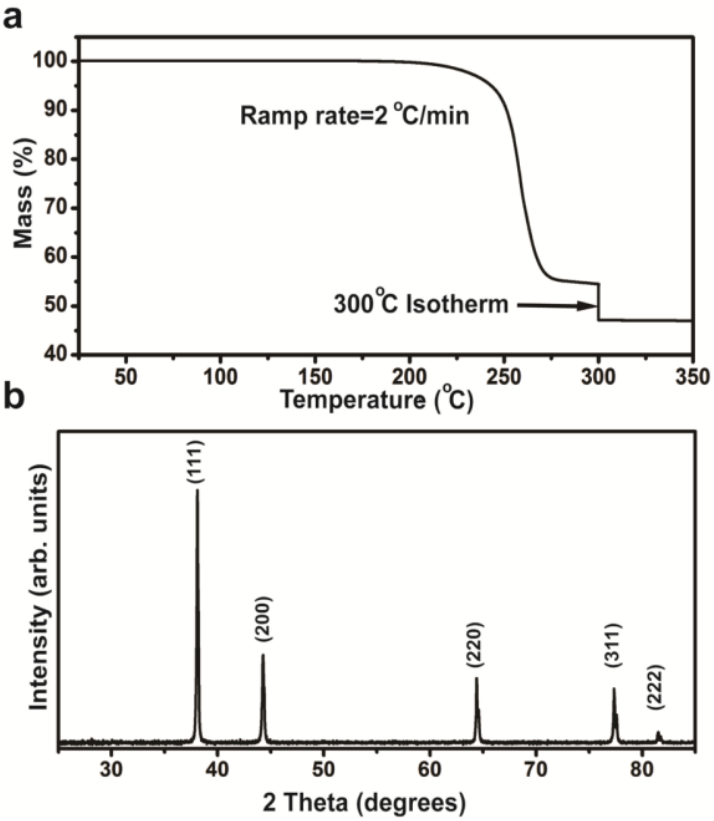

Figure 5.2. (a) Thermogravimetric analysis on silver benzoate. The temperature ramp rate was 2°C/min and a 2 hr isotherm was applied at 300°C. (b) X-ray diffraction pattern of silver made *via* the thermal decomposition of silver benzoate.

Composites used for phase change studies were prepared by drop-casting the combined Bi nanoparticle – silver benzoate solution, solvent removal at 100°C, and then silver benzoate thermal decomposition at 300°C for 2 hours. The results of this nanocomposite formation process are shown in Figure 3. The size and shape preservation of the Bi nanoparticles during this process is most clearly seen in Figure 3a, which has a low Bi volume fraction. Figure 3b shows a composite with a large volume fraction of Bi nanoparticles, which is more representative of the composites used for phase change studies (*i.e.* Figures 4 and 5). To confirm the homogeneous dispersion of the Bi nanoparticles throughout the matrix, we imaged a composite over a large area and collected chemical composition maps using energy dispersive x-ray spectroscopy.

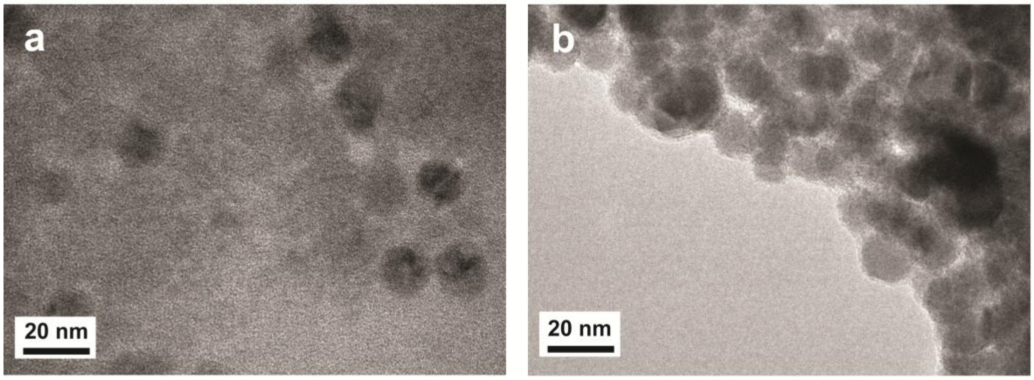

Figure 5.3. (a) TEM image of a Bi-Ag nanocomposite with a low Bi nanoparticle volume fraction. (b) TEM image of a Bi-Ag nanocomposite with a high Bi nanoparticle volume fraction.

Despite the decomposition temperature of the silver benzoate being above the melting temperature of the Bi, we do not observe any alloying between the Bi nanoparticles and Ag matrix. This is primarily because the phase behavior of Ag-Bi is such that no compounds form between these elements.[185] In addition, the solubility of Ag in Bi is negligibly small and the solubility of Bi in Ag is only 0.83 at% at 262°C.[185] We also believe the oleic acid ligands protect the Bi nanoparticles during silver benzoate decomposition. In our past work on Bi nanoparticle melting inside polymer matrices,[185] Bi nanoparticle melting was only observed after an initial "break-in" period at elevated temperature (*e.g.* 1 hour at 300°C). We presume this is due to the oleic acid ligands stabilizing the Bi surface and temporarily inhibiting melting. Similar surface stabilization effects have been observed in other literature such as Pb nanoparticles in Al matrices[186] and Ag nanoparticles in Ni matrices.[187]

Unlike typical *in situ* metal nanocomposite formation techniques (*i.e.* ball milling,[147, 188] melt spinning,[146, 189] and ion implantation[179, 190]), our metal matrix - metal nanoparticle composite formation technique enables excellent control over particle size, shape, and composition. By separating the steps of nanoparticle synthesis and nanocomposite formation, we have enabled independent quality control over nanoparticle morphology and facile control over nanoparticle volume fraction. This concept of separating nanoparticle synthesis and nanocomposite formation has been previously demonstrated to produce nanocomposites with organic matrices[56, 191, 192], oxide matrices [53, 193] and semiconductor matrices.[26, 194, 195] Herein, we have applied this concept to metal matrix nanocomposites. We do note that identifying appropriate metal precursors is not trivial because many precursors decompose into metal-oxide instead of metal. This was another reason for our choice of a silver matrix; in addition to its favorable phase behavior with bismuth and its very high thermal conductivity, it is energetically favorable to form silver over silver oxide due to silver's high reduction potential. By judicious selection of solvents, nanoparticles, and metal precursors, we believe this approach can be generalized to other metal nanocomposite chemical compositions. Soluble metal precursors that decompose into copper,[196, 197] silver,[198, 199] gold,[200] palladium[201], cobalt,[202] and rhodium[202] have been identified in the literature.

Nanocomposite Melting Temperature and Thermal Energy Storage Density

To investigate the melting characteristics of our Ag matrix – Bi nanoparticle composites, differential scanning calorimetry (DSC) measurements were performed. A representative heating and cooling cycle of a nanocomposite containing 13.2 nm Bi nanoparticles is shown in Figure 5.4a. One endothermic valley was observed at 246 °C during heating and we attribute this to nanoparticle melting. In accordance with size-dependent melting, this melting occurs well below the melting temperature of bulk Bi, 271 °C. During cooling, three exothermic peaks were observed. The first peak was broad and appeared around 224 °C, where as the second and third peak appeared around 137 °C and 93 °C, respectively. We attribute these peaks to three separate nanoparticle freezing events because the total energy released is equivalent to the energy absorbed during nanoparticle melting; this data suggests that three different nucleation mechanisms are present within our nanocomposite. The Bi nanoparticles also exhibit a significant amount of supercooling, which could likely be mitigated *via* surface chemistry modification on the nanoparticles.[203] The melting and freezing assignments in our nanocomposite were corroborated by a control DSC measurement on silver prepared *via* silver benzoate thermal decomposition. No discernible features in the control measurement are observed throughout the whole temperature range. In addition to facilitating fast thermal transport, the composite’s Ag matrix is also intended to function as a nanoparticle isolation barrier that prevents nanoparticle coalescence during melt-freeze cycles. To examine the matrix’s effectiveness, we subjected a composite to 100 melt-freeze cycles. As shown in Figure 4b, no notable changes in melting temperature or enthalpy of fusion were observed throughout the cycles. Note that in Figure 5.4 we have used the endothermic valley minimum and full width half maximum for the melting temperature and melting temperature uncertainty, respectively.

One benefit of employing nanoparticles as PCM is that the melting temperature can be tuned *via* particle diameter. This design variable provides additional flexibility when engineering the working temperature of a PCM. To demonstrate this capability, we prepared twelve composites containing 8.1 ± 1.0, 9.8 ± 0.8, 13.2 ± 0.6 and 14.9 ± 0.6 nm Bi nanoparticles. As the nanoparticle diameter varied from 8.1 – 14.9 nm, the melting temperature varied from 236 – 252°C (Figure 5.4c-d). We also observe a size-dependent enthalpy of fusion that accompanies the size-dependent melting temperature; the nanoparticle enthalpy of fusion varied from 20.1 – 37.6 J/g_{Bi} over our range of nanoparticle diameters (Figure 5.4c-d). Our prior work on Bi nanoparticles in polymer matrices showed different ranges of melting temperature and enthalpy of fusion in similarly-sized nanoparticles (218 – 240°C and 12.9 – 42.1 J/g_{Bi}).[56] This indicates that the melting temperature and enthalpy of fusion of nanoparticles is a function of both size and surrounding environment. Past observations of size-dependent enthalpy of fusion required the use of sophisticated nanocalorimetry techniques.[99] It is notable that we are able to extract size-dependent enthalpies of fusion using widely available standard benchtop DSC measurements. This is possible because our nanocomposite formation technique yields large sample sizes of monodisperse nanoparticles, accurate Bi volume fraction control, and protection against nanoparticle coalescence. We now note that this paper discusses two different types of enthalpy of fusion. The first one is the gravimetric enthalpy of fusion of the nanoparticle component in the composite, which is the enthalpy of fusion discussed above and in Figure 5.4. In the following discussion and Figure 5.5, we focus on the nanocomposite's effective volumetric enthalpy of fusion. We note that we use nanocomposite mass to deduce nanocomposite volume, and hence the volumetric enthalpy of fusions below do not account for porosity effects.

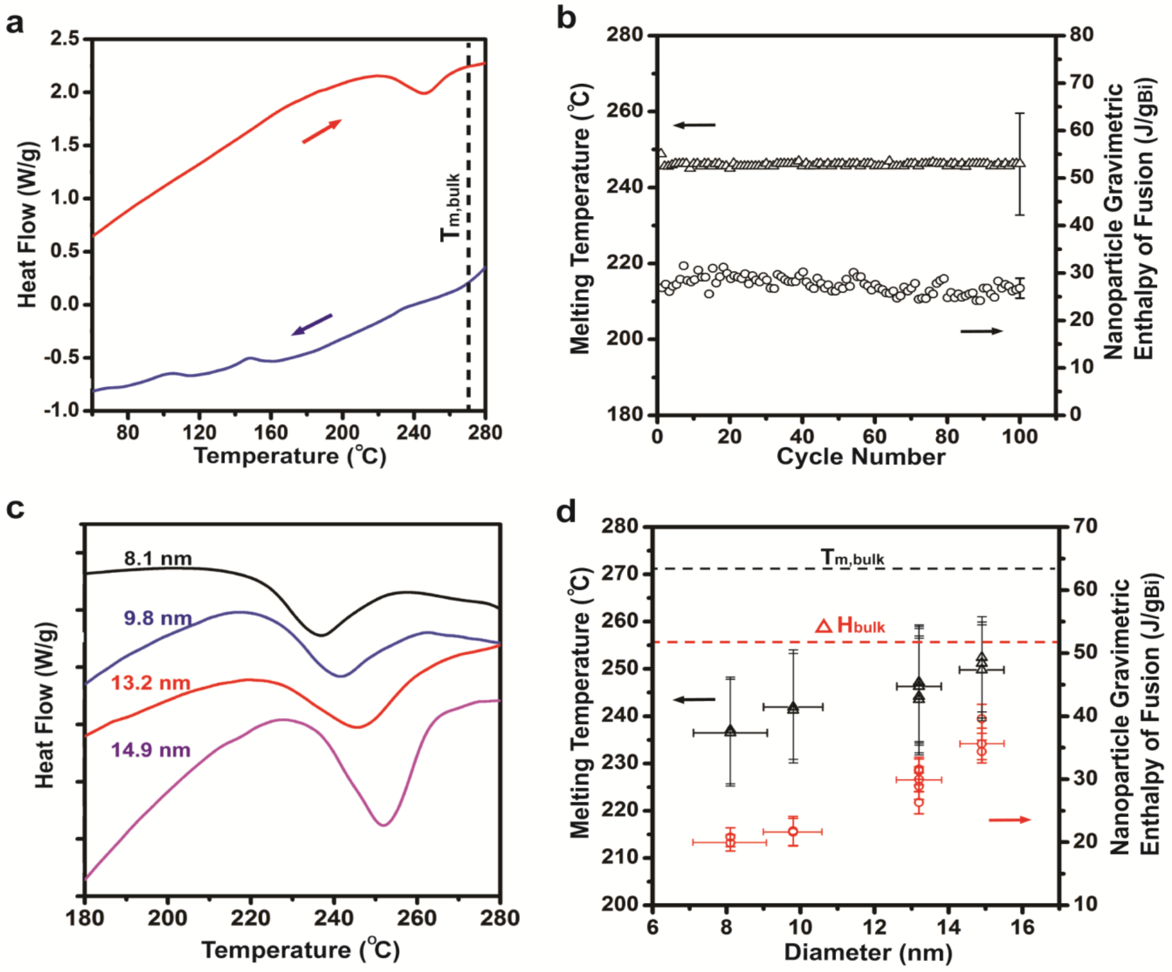

Figure 5.4. (a) A heating and cooling DSC cycle for a composite with Bi nanoparticles (NPs) of 13.2 nm diameter. (b) Melting characteristics of a composite with 13.2 nm Bi nanoparticles throughout 100 thermal cycles. (c) The endothermic melting valley during DSC measurements on composites with different Bi nanoparticle diameters. For clarity, the data in part (c) has been offset along the vertical axis; each tick mark represents 0.2 W/g. (d) Size-dependent melting temperature (triangles) and enthalpy of fusion (circles)

for the Bi nanoparticles. All nanocomposites in part (a), (b), (c), and (d) have a similar nanoparticle volume fraction of approximately 0.20 – 0.25. We note that the large error bars for melting temperature in (b) and (d) arise from our use of the endothermic valley's full width half maximum for the measurement uncertainty. We use the endothermic valley location as the melting temperature, and these variations were insignificant as seen in part (b).

The thermal energy storage density of the composite can be controlled independently of melting temperature by varying the nanoparticle volume fraction. As shown in Figure 5a, the composite exhibits an increase in volumetric enthalpy of fusion as the volume fraction of Bi nanoparticles is increased. This enables a simple two-step process for PCM design. First, the nanoparticle size is chosen to yield the desired melting temperature. Second, the Bi content is varied to yield the desired composite volumetric enthalpy of fusion. We successfully increased the Bi nanoparticles volume fraction to ~34% without observing detrimental effects on melting temperature (*i.e.* nanoparticle coalescence during melt-freeze cycling), which indicates that the Ag matrix effectively protects to this level of nanoparticle loading (Figure 5.5a). The Bi volume fraction in the nanocomposite was determined by using the relative concentrations of the bismuth nanoparticle and silver benzoate solutions. Since the Bi nanoparticle solution contains both the nanoparticles and surface ligands, we used a procedure described in our prior work[56] to determine the nanoparticle solution’s true Bi content. In brief, this procedure works by doing cyclic DSC measurements on the Bi nanoparticles in the absence of Ag matrix. During this procedure, the nanoparticles coalesce into bulk and melting is observed at the bulk Bi melting temperature, 271°C. The Bi mass is then determined by comparing the absorbed energy during melting to the bulk Bi enthalpy of fusion (51.9 J/g). Our nanocomposites achieve a ~ 50 – 100% enhancement in volumetric energy density relative to composites with an equivalent volume fraction of typical organic PCMs (Figure 5.5b).[204] [205] However, due to nanoparticle coalescence at high nanoparticle volume fractions, the maximum PCM volume fraction in our composites is lower than that achievable with organic PCM composites.

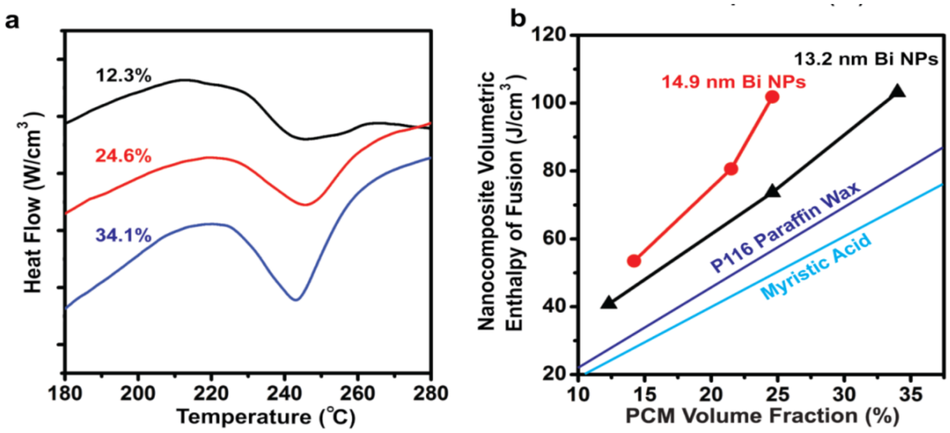

Figure 5.5. (a) The endothermic melting valley during DSC measurements on composites with 13.2 nm diameter Bi nanoparticles and varying Bi volume fraction. For clarity, the data in part (a) has been offset along the vertical axis; each tick mark represents 0.5 W/cm^3. (b) The effective volumetric energy density for composites containing 13.2 and 14.9 nm Bi nanoparticles with varying Bi nanoparticle volume fractions. For comparison, two common organic phase change materials, P116 paraffin wax and myristic acid, are also shown.

Nanocomposite Thermal Transport

Another objective of this nanocomposite design is to facilitate fast thermal charging/discharging. Conventional thermal storage materials such as paraffins, salt hydrates, and inorganic salts have poor thermal conductivities on the order of $10^{-1} – 10^{0}$ W/m-K, which lead to poor thermal charging/discharging rates. In contrast, metals have thermal conductivities ranging from $10^{1} – 10^{2}$ W/m-K, which suggests our metal nanocomposite should have superior thermal transport performance. To validate this conjecture, we measured the thermal conductivity of our nanocomposites using the Wiedemann-Franz law.[180]

The Wiedemann-Franz law states that the thermal conductivity, k, of metallic materials can be related to the electrical conductivity, σ, *via* the Lorenz number, L, and absolute temperature, T.

$$\frac{k}{\sigma} = LT$$

For most metals, the Sommerfeld value for the Lorenz number, L_0, is a reasonable approximation:[206, 207]

$$L_0 = \frac{\pi^2 k_B^2}{3e^2} = 2.44 \times 10^{-8}\ \mathrm{W\Omega K^{-2}}$$

where k_B, and e are the Boltzmann constant and elementary charge, respectively. In general, both electrons and phonons conduct heat in solids, and so it should be noted that thermal conductivity measurements obtained using the Wiedemann-Franz law approach only contain electron contributions.[30, 180] However, since the phonon contribution to thermal conductivity in metals is negligible, this approach effectively measures the total thermal conductivity in our nanocomposites.[30] We prepared thin film nanocomposite samples by spin-coating and then measured their corresponding electrical conductivity using the Van der Pauw method. The thermal conductivity was then obtained using the Sommerfeld value for the Lorenz number in the Wiedemann-Franz law.

We measured the thermal conductivity of nanocomposites containing 13 nm Bi nanoparticles with volume fractions ranging from 0 – 10% (Figure 5.6). The nanocomposite thermal conductivity varied from 270 ± 61 W/m-K to 128 ± 23 W/m-K over this range and larger Bi nanoparticle volume fractions resulted in lower thermal conductivities. Notably, these thermal conductivity values are significantly greater than typical thermal storage materials by several orders of magnitude. The thermal conductivity of our nanocomposite with 0% Bi nanoparticles corresponds to silver prepared *via* thermal decomposition of silver benzoate and is approximately 40% less than literature values for bulk silver. Given that our Ag samples exhibit porosity and are nanocrystalline with grain sizes on the order of 100 nm, this moderate decrease in thermal conductivity is reasonable. The uncertainty in nanocomposite thermal conductivity was dominated by film thickness uncertainty caused by roughness. Samples with Bi nanoparticle fractions greater than 10 vol% were not experimentally measured due to poor film quality. We also note that our use of the Sommerfeld value for the Lorenz number assumes that the nanocomposite's electron gas is degenerate and that the electron mean free path is the same for both electrical conductivity and thermal conductivity.[206, 207] Since Lorenz number deviations of up to ~50% from the Sommerfeld value have been reported in the literature,[208, 209] our use of this value introduces additional uncertainty. Nonetheless, this uncertainty is relatively small given the several orders of magnitude improvement in thermal conductivity of our nanocomposites.

The nanocomposite thermal conductivity decreases from 215 ± 51 W/m-K to 128 ± 23 W/m-K as the volume fraction of 13 nm Bi nanoparticles increases from 2% - 10%. This thermal conductivity trend arises due to two different effects. The first effect is that increasing nanoparticle volume fraction decreases the thermal conductivity of the Ag matrix itself. This arises because the nanocomposite's interface density is commensurate with the mean free path of the thermal energy carriers in the Ag phase (*i.e.* ~ 33 nm, see Supporting Information). These interfaces act as scattering sites, which leads to smaller effective mean free paths in the Ag and lower Ag thermal conductivities. The second effect causing this thermal conductivity trend is that the volume fraction of the highly-conductive Ag component decreases as the nanoparticle volume increases. It should also be noted that due to the finite thermal interface conductance between the Ag and Bi, the Bi nanoparticles contribute a negligible amount to the overall nanocomposite thermal conductivity. Based on experimental data for similar interfaces,[74, 210] we estimate that the thermal interface conductance between the Bi nanoparticles and the Ag matrix is 34 MW/m^2-K (this value is lower than typical metal-metal interface conductances[211] due to the presence of organic ligands at the Bi-Ag interface). For reference purposes, an interface conductance can be converted into an equivalent film thickness by dividing the film's thermal conductivity by its thickness. In the case of our nanocomposite, the interface conductance between the Bi nanoparticles and Ag matrix is equivalent to a 7.9 μm thick Ag film. Consequently, the nanocomposite's thermal conductivity is dominated by the thermal conductivity of the monolithic Ag matrix and smaller Ag matrix volume fractions directly lead to small thermal conductivities.

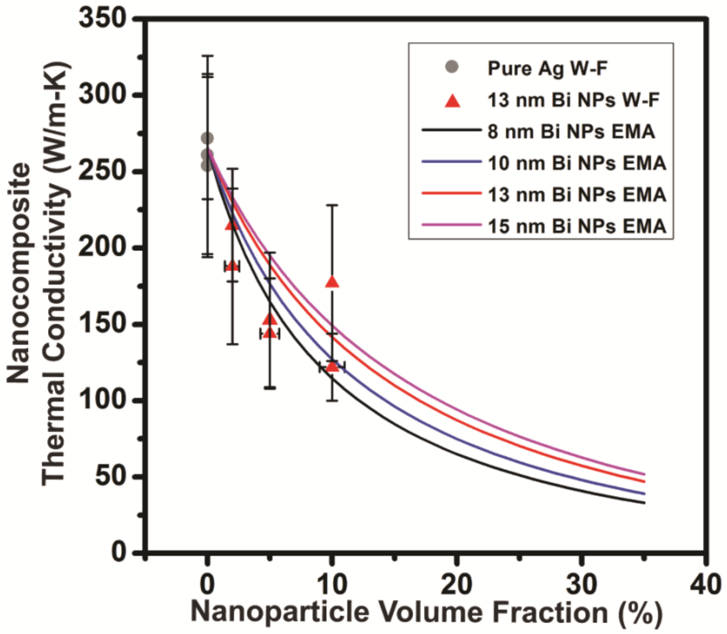

Figure 5.6. Nanocomposite thermal conductivity measurements using the Wiedemann-Franz (W-F) law and thermal conductivity calculations using the modified effective medium approximation (EMA) for varying nanoparticle (NP) diameter and volume fraction.

To further explore the effects of nanoparticle size and volume fraction on the nanocomposite thermal conductivity, we utilize a modified effective medium approximation (EMA) that accounts for nanoscale thermal transport effects. The conventional EMA approach is invalid for nanostructured materials because large interface densities lead to enhanced scattering of thermal energy carriers. This scattering leads to thermal conductivity changes in the nanocomposite as well as the individual nanocomposite constituents themselves. The modified EMA approach suggested by Minnich and Chen[212] addresses this issue by accounting for interface density when estimating the mean free path of thermal energy carriers. Using their modified EMA approach, they obtained good agreement with more sophisticated Monte Carlo calculations on nanocomposite thermal conductivity. Recently, Ong *et al.*[59] successfully applied this approach to fit experimental thermal conductivity data on nanocrystal arrays comprised of nanoparticles with similar structure to the nanoparticles in our work. Consequently, we believe this modified EMA method should provide reasonable predictions for the thermal conductivity of our nanocomposites. Note that the original work by Minnich and Chen[212] focused on thermal transport *via* phonons. Since our nanocomposites are metallic, the predominant heat carriers are free electrons instead of phonons and we have adapted our calculations to account for this. We neglect the phonon contribution to thermal conductivity because it is typically three orders of magnitude smaller than the electron contribution in metals. Additional calculation details can be found in Supporting Information.

Figure 6 directly compares our modified EMA calculations with our experimental measurements. Given our measurement uncertainty, these results are in reasonable agreement. These calculations indicate that our nanocomposites with ~35 vol% Bi (*i.e.* the highest volume fraction for which melting point depression could be maintained) have a thermal conductivity of approximately 33 to 52 W/m-K for nanoparticle diameters from 8 to 15 nm. Changing the Ag-Bi thermal interface conductance and/or the Bi nanoparticle thermal conductivity by several orders of magnitude in the EMA calculations had negligible effects on the nanocomposite thermal conductivity (see Supporting Information). This supports our above assertions that the dominant factors causing the nanocomposite thermal conductivity trend for increasing Bi nanoparticle volume fraction are decreases in Ag thermal conductivity and Ag volume fraction. These modified EMA calculations also indicate that smaller Bi nanoparticle diameters lead to smaller nanocomposite thermal conductivities. This can be understood by realizing that for equivalent volume fractions, the Ag-Bi interface density increases as the Bi nanoparticle diameter decreases. This increased interface density causes the effective mean free path in the Ag matrix to decrease and consequently the thermal conductivity of the Ag matrix itself decreases as nanoparticle diameter decreases. Overall, our combined thermal conductivity calculations and modified EMA calculations indicate that our nanocomposite thermal conductivity is on the order of $10^1 – 10^2$ W/m-K, which is several orders of magnitude better than typical thermal storage materials (*e.g.* $10^{-1} – 10^0$).[159, 165] This increased thermal conductivity improves thermal energy storage performance *via* significantly faster thermal charging/discharging times.

Conclusion

We have created nanocomposites that consist of phase change Bi nanoparticles embedded in an Ag matrix. Our nanocomposite formation approach enables excellent control over nanoparticle size, shape, and volume fraction, and can likely be generalized to other metal matrix – metal nanoparticle compositions. Using these Ag matrix – Bi nanoparticle composites, we have experimentally demonstrated PCMs with tunable melting temperatures and large thermal energy densities. The Ag matrix preserves the nanocomposite structure during melt-freeze cycles and enables excellent thermal conductivities. Thermal conductivity measurements and modified EMA calculations indicate that our nanocomposite thermal conductivity is on the order of $10^1 – 10^2$ W/m-K, which is several orders of magnitude better than typical thermal storage materials.

Overall, this metal matrix – metal nanoparticle composites represents a new paradigm for PCMs that can be used for thermal storage and management applications.

Materials and Methods

Materials and Equipment: All reagents and solvents were purchased from Sigma Aldrich. Sample imaging was done with transmission electron microscopy (TEM, Tecnai F20) and scanning electron microscopy (SEM, Nova 200 NanoLab FEI). The X-ray diffraction was taken on high resolution x-ray diffractometer (XRD, PANALYTICAL X'PERT PRO), with CuKα X-ray source operating at 40 kV and 40 mA. The thermogravimetric analysis and differential scanning calorimetry were performed using a TA Instruments Q500 TGA and TA Instruments Q20 DSC. Elemental analysis was carried out by energy dispersive spectroscopy (EDS, EDAX). The masses of nanoparticles and nanocomposites were determined using a Mettler Toledo UMX2 Ultra-Microbalance. Thin film conductivity measurements were performed with a Keithley 2400 sourcemeter and film thicknesses were determined by profilometry (Dektak XT stylus profilometer). Unless otherwise indicated, all samples were prepared and stored in an air-free environment. Samples were exposed to air for brief periods when using the above instruments.

Bi Precursor Synthesis: $Bi[N(SiMe_3)_2]_3$ is a metal silylamide and was used as the Bi precursor in this work. This precursor was prepared by reacting $BiCl_3$ and $Li[N(SiMe_3)_2]$ at 0 °C for 2 hours.[110] In a typical synthesis, two solutions were prepared in a nitrogen filled glovebox: 1) 3.34 g of $Li[N(SiMe_3)_2]$ dissolved in 40 mL diethyl ether, and 2) 2.10 g $BiCl_3$ dissolved in a mixture of 40 mL diethyl ether and 10 mL tetrahydrofuran (THF).

Solution 1 was firstly added into the flask and cooled down to 0 °C with an ice bath. Solution 2 was then added drop-wise to the flask and reacted for 2 hours. After 2 hours, the reaction mixture was a non-transparent yellow color and was then filtered through a PTFE filter (pore size 200 nm). The resulting bright yellow solution was dried under vacuum for 1 hour, and then redissolved in 15 mL of anhydrous pentane. The solution was again filtered and dried under vacuum for another 2 hours. The final product $Bi[N(SiMe_3)_2]_3$ was a yellow powder and stored in a nitrogen-filled glovebox for future use.

Bi Nanoparticle Synthesis: In a typical 13 nm Bi nanoparticle synthesis, 20 g of hexdecylamine (HDA) was loaded into a three-neck flask and degassed before heating to 130 °C. At this temperature, two solutions were injected into the flask with a time interval of 15 seconds between injections. The first solution was 100 μL of 1 M $Li(Et_3BH)$ in THF and the second was 0.14 g $Bi[N(SiMe_3)_2]_3$ and 0.17 g $Li[N(SiMe_3)_2]$ co-dissolved in 2 mL of toluene. 15 seconds after the 2nd injection, the flask was swiftly removed from the heating mantle and cooled using a water bath. During cooling, 20 mL toluene was injected into the reaction mixture to prevent the HDA from solidifying. Once the temperature dropped to 40 °C, the flask was disconnected from the schlenk line and the cleaning process was done in air. The Bi nanoparticles were isolated from the mixture by precipitating with a 1:1 addition of ethanol and centrifuging at 3000 rpm for 5 minutes. It should be noted that this synthesis yields Bi nanoparticles with surface-bound HDA ligands. We switched these HDA ligands for oleic acid ligands immediately after the first precipitation, which led to improved colloidal nanoparticle solution stability. The

Bi nanoparticles were further cleaned three times by precipitating with ethanol and finally suspended in toluene.

Nanocomposite Formation: The nanocomposites were prepared in three steps. First, the Bi nanoparticles were synthesized as described above. The nanoparticles were further cleaned by additional precipitations with ethanol and then dissolved in toluene with a concentration of ~ 1 mg/mL. A fresh silver precursor solution was prepared by dissolving silver benzoate using pyridine and stirring overnight. The concentration of silver benzoate solution was ~ 2 mg/mL. Second, an appropriate amount of Bi nanoparticle suspension and silver benzoate solution were combined to yield the desired Bi nanoparticle volume fraction and this combined solution was stirred for an additional 2 hours. This combined solution was then filtered through a PTFE filter and drop-cast on appropriate substrates (*e.g.* DSC pan or TEM silicon nitride window). Finally, the cast film was thermally annealed in two steps: 100 °C for 1 hour and then 300 °C for 2 hours in a nitrogen atmosphere.

DSC Measurements: All DSC samples were prepared by drop-casting an appropriate amount of Bi nanoparticle – silver benzoate combined solution into an aluminum DSC pan. The sample was then subjected to a two-step thermal anneal in a nitrogen atmosphere as described above. During DSC experiments, all samples were heated and cooled between 0 °C to 300 °C at a rate of 10 °C/min for at least 15 cycles.

Thermal Conductivity Measurements: The thermal conductivity measurements were carried out by first measuring electrical conductivity using the Van der Pauw method and then converting this electrical conductivity into a thermal conductivity using the Wiedemann-Franz law.[180] Samples for thermal conductivity measurements were prepared on silicon substrates by spin coating 100 μL of solution at 1500 rpm. The film was then heated sequentially at 100 °C and 350 °C. In some instances this deposition process was repeated to yield an appropriate film thickness. Final film thicknesses were typically 200 - 600 nm.

TEM sample preparation and particle size determination: All Bi nanoparticle TEM samples were prepared by drop-casting 50 μL of a dilute nanoparticle suspension onto a carbon film supported copper TEM grid. The nanoparticle diameter was determined with ImageJ by analyzing a representative TEM image containing 100 - 200 Bi nanoparticles. The diameter uncertainties in manuscript represent the standard deviation of the nanoparticle diameters. The nanocomposite TEM samples were prepared by drop-casting a dilute combined solution of Bi nanoparticles and silver benzoate onto a Si_3N_4 window and then annealed as described in the nanocomposite formation section above.

REFERENCES

1. L. E. Brus, Electron ‒ Electron and Electron ‐ Hole Interactions in Small Semiconductor Crystallites: The Size Dependence of the Lowest Excited Electronic State, *J. Chem. Phys.* 80, 4403-4409 (1984).

2. R. Rossetti, S. Nakahara and L. E. Brus, Quantum Size Effects in the Redox Potentials, Resonance Raman Spectra, and Electronic Spectra of Cds Crystallites in Aqueous Solution, *J. Chem. Phys.* 79, 1086-1088 (1983).

3. C. Burda, X. B. Chen, R. Narayanan and M. A. El-Sayed, Chemistry and Properties of Nanocrystals of Different Shapes, *Chem. Rev.* 105, 1025-1102 (2005).

4. H. Colfen and M. Antonietti, Mesocrystals: Inorganic Superstructures Made by Highly Parallel Crystallization and Controlled Alignment, *Angew. Chem., Int. Ed.* 44, 5576-5591 (2005).

5. M. A. El-Sayed, Some Interesting Properties of Metals Confined in Time and Nanometer Space of Different Shapes, *Acc. Chem. Res.* 34, 257-264 (2001).

6. Y. W. Jun, J. S. Choi and J. Cheon, Shape Control of Semiconductor and Metal Oxide Nanocrystals through Nonhydrolytic Colloidal Routes, *Angew. Chem., Int. Ed.* 45, 3414-3439 (2006).

7. S. Link and M. A. El-Sayed, Shape and Size Dependence of Radiative, Non-Radiative and Photothermal Properties of Gold Nanocrystals, *Int. Rev. Phys. Chem.* 19, 409-453 (2000).

8. C. B. Murray, C. R. Kagan and M. G. Bawendi, Synthesis and Characterization of Monodisperse Nanocrystals and Close-Packed Nanocrystal Assemblies, *Annu. Rev. Mater. Sci.* 30, 545-610 (2000).

9. D. V. Talapin, J.-S. Lee, M. V. Kovalenko and E. V. Shevchenko, Prospects of Colloidal Nanocrystals for Electronic and Optoelectronic Applications, *Chem. Rev.* 110, 389-458 (2010).

10. A. R. Tao, S. Habas and P. Yang, Shape Control of Colloidal Metal Nanocrystals, *Small* 4, 310-325 (2008).

11. Y. Xia, Y. Xiong, B. Lim and S. E. Skrabalak, Shape-Controlled Synthesis of Metal Nanocrystals: Simple Chemistry Meets Complex Physics?, *Angew. Chem., Int. Ed.* 48, 60-103 (2009).

12. Y. Yin and A. P. Alivisatos, Colloidal Nanocrystal Synthesis and the Organic-Inorganic Interface, *Nature* 437, 664-670 (2005).

13. J. M. Yuk, J. Park, P. Ercius, K. Kim, D. J. Hellebusch, M. F. Crommie, J. Y. Lee, A. Zettl and A. P. Alivisatos, High-Resolution Em of Colloidal Nanocrystal Growth Using Graphene Liquid Cells, *Science* 336, 61-64 (2012).

14. J. Park, H. Elmlund, P. Ercius, J. M. Yuk, D. T. Limmer, Q. Chen, K. Kim, S. H. Han, D. A. Weitz, A. Zettl, *et al.*, 3d Structure of Individual Nanocrystals in Solution by Electron Microscopy, *Science* 349, 290-295 (2015).

15. X. Dai, Z. Zhang, Y. Jin, Y. Niu, H. Cao, X. Liang, L. Chen, J. Wang and X. Peng, Solution-Processed, High-Performance Light-Emitting Diodes Based on Quantum Dots, *Nature* 515, 96-99 (2014).

16. K. S. Cho, E. K. Lee, W. J. Joo, E. Jang, T. H. Kim, S. J. Lee, S. J. Kwon, J. Y. Han, B. K. Kim, B. L. Choi, *et al.*, High-Performance Crosslinked Colloidal Quantum-Dot Light-Emitting Diodes, *Nat. Photonics* 3, 341-345 (2009).

17. S. A. Mcdonald, G. Konstantatos, S. Zhang, P. W. Cyr, E. J. Klem, L. Levina and E. H. Sargent, Solution-Processed Pbs Quantum Dot Infrared Photodetectors and Photovoltaics, *Nat. Mater.* 4, 138-142 (2005).

18. C.-H. M. Chuang, P. R. Brown, V. Bulović and M. G. Bawendi, Improved Performance and Stability in Quantum Dot Solar Cells through Band Alignment Engineering, *Nat. Mater.* 13, 796-801 (2014).

19. S. J. Oh, Z. Wang, N. E. Berry, J.-H. Choi, T. Zhao, E. A. Gaulding, T. Paik, Y. Lai, C. B. Murray and C. R. Kagan, Engineering Charge Injection and Charge Transport for High Performance Pbse Nanocrystal Thin Film Devices and Circuits, *Nano Lett.* 14, 6210-6216 (2014).

20. M. E. Turk, J.-H. Choi, S. J. Oh, A. T. Fafarman, B. T. Diroll, C. B. Murray, C. R. Kagan and J. M. Kikkawa, Gate-Induced Carrier Delocalization in Quantum Dot Field Effect Transistors, *Nano Lett.* 14, 5948-5952 (2014).

21. A. L. Rogach, D. V. Talapin, E. V. Shevchenko, A. Kornowski, M. Haase and H. Weller, Organization of Matter on Different Size Scales: Monodisperse Nanocrystals and Their Superstructures, *Adv. Funct. Mater.* 12, 653-664 (2002).

22. A. R. Smith, W. Yoon, W. B. Heuer, S. I. M. Baril, J. E. Boercker, J. G. Tischler and E. E. Foos, Effect of Ligand Structure on the Optical and Electronic Properties of Nanocrystalline Pbse Films, *J. Phy. Chem. C* 116, 6031-6037 (2012).

23. J.-S. Lee, M. V. Kovalenko, J. Huang, D. S. Chung and D. V. Talapin, Band-Like Transport, High Electron Mobility and High Photoconductivity in All-Inorganic Nanocrystal Arrays, *Nat. Nanotechnol.* 6, 348-352 (2011).

24. J. Tang, K. W. Kemp, S. Hoogland, K. S. Jeong, H. Liu, L. Levina, M. Furukawa, X. Wang, R. Debnath and D. Cha, Colloidal-Quantum-Dot Photovoltaics Using Atomic-Ligand Passivation, *Nat. Mater.* 10, 765-771 (2011).

25. Y. Sun, H. Fang, L. Pan, M. Han, S. Xu, X. Wang, B. Xu and Y. Wu, Impact of Surface-Bound Small Molecules on the Thermoelectric Property of Self-Assembled Ag2te Nanocrystal Thin Films, *Nano Lett.* 15, 3748-3756 (2015).

26. M. V. Kovalenko, M. Scheele and D. V. Talapin, Colloidal Nanocrystals with Molecular Metal Chalcogenide Surface Ligands., *Science* 324, 1417-1420 (2009).

27. C. Giansante, I. Infante, E. Fabiano, R. Grisorio, G. P. Suranna and G. Gigli, "Darker-Than-Black" Pbs Quantum Dots: Enhancing Optical Absorption of Colloidal Semiconductor Nanocrystals Via Short Conjugated Ligands, *J. Am. Chem. Soc.* 137, 1875-1886 (2015).

28. Y. Gao, M. Aerts, C. S. S. Sandeep, E. Talgorn, T. J. Savenije, S. Kinge, L. D. A. Siebbeles and A. J. Houtepen, Photoconductivity of Pbse Quantum-Dot Solids: Dependence on Ligand Anchor Group and Length, *ACS Nano* 6, 9606-9614 (2012).

29. M. V. Kovalenko, M. Scheele and D. V. Talapin, Colloidal Nanocrystals with Molecular Metal Chalcogenide Surface Ligands, *Science* 324, 1417-1420 (2009).

30. G. Chen, *Nanoscale Energy Transport and Conversion: A Parallel Treatment of Electrons, Molecules, Phonons, and Photons.* (New York: Oxford University Press, 2005; pp 249-253).

31. R. Y.-S. Wang, *Energy Transport and Conversion in Nanostructured Materials*. (ProQuest, 2008).

32. D. G. Cahill, Thermal Conductivity Measurement from 30 to 750 K: The 3ω Method, *Rev. Sci. Instrum.* 61, 802-808 (1990).

33. J. P. Feser, E. M. Chan, A. Majumdar, R. A. Segalman and J. J. Urban, Ultralow Thermal Conductivity in Polycrystalline Cdse Thin Films with Controlled Grain Size, *Nano Lett.* 13, 2122-2127 (2013).

34. C. Dames and G. Chen, 1ω,2ω, and 3ω Methods for Measurements of Thermal Properties, *Rev. Sci. Instrum.* 76, 124902 (2005).

35. T. Borca-Tasciuc, A. R. Kumar and G. Chen, Data Reduction in 3ω Method for Thin-Film Thermal Conductivity Determination, *Rev. Sci. Instrum.* 72, 2139-2147 (2001).

36. H. R. Shanks, P. D. Maycock, P. H. Sidles and G. C. Danielson, Thermal Conductivity of Silicon from 300 to 1400k, *Physical Review* 130, 1743-1748 (1963).

37. I. M. Abdulagatov, S. N. Emirov, T. A. Tsomaeva, K. A. Gairbekov, S. Y. Askerov and N. A. Magomedova, Thermal Conductivity of Fused Quartz and Quartz Ceramic at High Temperatures and High Pressures, *J. Phys. Chem. Solids* 61, 779-787 (2000).

38. J. S. Blakemore, Semiconducting and Other Major Properties of Gallium Arsenide, *J. Appl. Phys.* 53, R123-R181 (1982).

39. I. Stark, M. Stordeur and F. Syrowatka, Thermal Conductivity of Thin Amorphous Alumina Films, *Thin Solid Films* 226, 185-190 (1993).

40. K. E. Goodson, M. I. Flik, L. T. Su and D. A. Antoniadis, Prediction and Measurement of the Thermal Conductivity of Amorphous Dielectric Layers, *J. Heat Transfer* 116, 317-324 (1994).

41. J. Liu, S. Ju, Y. Ding and R. Yang, Size Effect on the Thermal Conductivity of Ultrathin Polystyrene Films, *Appl. Phys. Lett.* 104, 153110 (2014).

42. P. Pawlow, The Dependency of the Melting Point on the Surface Energy of a Solid Body. (Supplement.), *Z. Phys. Chem., Stoechiom. Verwandtschaftsl.* 65, 545-548 (1909).

43. P. Buffat and J. P. Borel, Size Effect on Melting Temperature of Gold Particles, *Physical Review A* 13, 2287-2298 (1976).

44. P. R. Couchman and W. A. Jesser, Thermodynamic Theory of Size Dependence of Melting Temperature in Metals, *Nature* 269, 481-483 (1977).

45. C. R. M. Wronski, Size Dependence of Melting Point of Small Particles of Tin, *Br. J. Appl. Phys.* 18, 1731-1737 (1967).

46. K. K. Nanda, Size-Dependent Melting of Nanoparticles: Hundred Years of Thermodynamic Model, *Pramana-Journal of Physics* 72, 617-628 (2009).

47. M. Takagi, Electron-Diffraction Study of Liquid-Solid Transition of Thin Metal Films, *J. Phys. Soc. Jpn.* 9, 359-363 (1954).

48. S. L. Lai, J. Y. Guo, V. Petrova, G. Ramanath and L. H. Allen, Size-Dependent Melting Properties of Small Tin Particles: Nanocalorimetric Measurements, *Physical Review Letters* 77, 99-102 (1996).

49. A. Sharma, V. V. Tyagi, C. R. Chen and D. Buddhi, Review on Thermal Energy Storage with Phase Change Materials and Applications, *Renewable Sustainable Energy Rev.* 13, 318-345 (2009).

50. B. Zalba, J. M. Marin, L. F. Cabeza and H. Mehling, Review on Thermal Energy Storage with Phase Change: Materials, Heat Transfer Analysis and Applications, *Appl. Therm. Eng.* 23, 251-283 (2003).

51. M. M. Kenisarin, High-Temperature Phase Change Materials for Thermal Energy Storage, *Renewable Sustainable Energy Rev.* 14, 955-970 (2010).

52. M. Kenisarin and K. Mahkamov, Solar Energy Storage Using Phase Change Materials, *Renewable Sustainable Energy Rev.* 11, 1913-1965 (2007).

53. A. Llordes, G. Garcia, J. Gazquez and D. J. Milliron, Tunable near-Infrared and Visible-Light Transmittance in Nanocrystal-in-Glass Composites., *Nature* 500, 323-326 (2013).

54. R. Y. Wang, J. P. Feser, J.-S. Lee, D. V. Talapin, R. Segalman and A. Majumdar, Enhanced Thermopower in Pbse Nanocrystal Quantum Dot Superlattices, *Nano Lett.* 8, 2283-2288 (2008).

55. M. Liu, Y. Ma, H. Wu and R. Y. Wang, Metal Matrix-Metal Nanoparticle Composites with Tunable Melting Temperature and High Thermal Conductivity for Phase-Change Thermal Storage, *ACS Nano* 9, 1341-1351 (2015).

56. M. Liu and R. Y. Wang, Phase Change Nanocomposites with Tunable Melting Temperature and Thermal Energy Storage Density., *Nanoscale* 5, 7234-7237 (2013).

57. F.-J. Fan, B. Yu, Y.-X. Wang, Y.-L. Zhu, X.-J. Liu, S.-H. Yu and Z. Ren, Colloidal Synthesis of Cu2cdsnse4 Nanocrystals and Hot-Pressing to Enhance the Thermoelectric Figure-of-Merit, *J. Am. Chem. Soc.* 133, 15910-15913 (2011).

58. F.-J. Fan, Y.-X. Wang, X.-J. Liu, L. Wu and S.-H. Yu, Large-Scale Colloidal Synthesis of Non-Stoichiometric Cu2znsnse4 Nanocrystals for Thermoelectric Applications, *Adv. Mater.* 24, 6158-6163 (2012).

59. W.-L. Ong, S. M. Rupich, D. V. Talapin, A. J. H. McGaughey and J. A. Malen, Surface Chemistry Mediates Thermal Transport in Three-Dimensional Nanocrystal Arrays, *Nat. Mater.* 12, 410-415 (2013).

60. M. B. Zanjani and J. R. Lukes, Phonon Dispersion and Thermal Conductivity of Nanocrystal Superlattices Using Three-Dimensional Atomistic Models, *J. Appl. Phys.* 115, 143515 (2014).

61. W.-L. Ong, S. Majumdar, J. A. Malen and A. J. H. McGaughey, Coupling of Organic and Inorganic Vibrational States and Their Thermal Transport in Nanocrystal Arrays, *J. Phy. Chem. C* 118, 7288-7295 (2014).

62. K. Szendrei, F. Cordella, M. V. Kovalenko, M. Böberl, G. Hesser, M. Yarema, D. Jarzab, O. V. Mikhnenko, A. Gocalinska, M. Saba, *et al.*, Solution-Processable near-Ir Photodetectors Based on Electron Transfer from Pbs Nanocrystals to Fullerene Derivatives, *Adv. Mater.* 21, 683-687 (2009).

63. J. Gao, C. L. Perkins, J. M. Luther, M. C. Hanna, H.-Y. Chen, O. E. Semonin, A. J. Nozik, R. J. Ellingson and M. C. Beard, N-Type Transition Metal Oxide as a Hole Extraction Layer in Pbs Quantum Dot Solar Cells, *Nano Lett.* 11, 3263-3266 (2011).

64. M. C. Weidman, K. G. Yager and W. A. Tisdale, Interparticle Spacing and Structural Ordering in Superlattice Pbs Nanocrystal Solids Undergoing Ligand Exchange, *Chem. Mater.* 27, 474-482 (2015).

65. D. Zherebetskyy, M. Scheele, Y. Zhang, N. Bronstein, C. Thompson, D. Britt, M. Salmeron, P. Alivisatos and L.-W. Wang, Hydroxylation of the Surface of Pbs Nanocrystals Passivated with Oleic Acid, *Science* 344, 1380-1384 (2014).

66. P. Podsiadlo, G. Krylova, B. Lee, K. Critchley, D. J. Gosztola, D. V. Talapin, P. D. Ashby and E. V. Shevchenko, The Role of Order, Nanocrystal Size, and Capping Ligands in the Collective Mechanical Response of Three-Dimensional Nanocrystal Solids, *J. Am. Chem. Soc.* 132, 8953-8960 (2010).

67. L. Cademartiri, E. Montanari, G. Calestani, A. Migliori, A. Guagliardi and G. A. Ozin, Size-Dependent Extinction Coefficients of Pbs Quantum Dots, *J. Am. Chem. Soc.* 128, 10337-10346 (2006).

68. G. Konstantatos, I. Howard, A. Fischer, S. Hoogland, J. Clifford, E. Klem, L. Levina and E. H. Sargent, Ultrasensitive Solution-Cast Quantum Dot Photodetectors, *Nature* 442, 180-183 (2006).

69. P. R. Brown, D. Kim, R. R. Lunt, N. Zhao, M. G. Bawendi, J. C. Grossman and V. Bulović, Energy Level Modification in Lead Sulfide Quantum Dot Thin Films through Ligand Exchange, *ACS Nano* 8, 5863-5872 (2014).

70. M. A. Hines and G. D. Scholes, Colloidal Pbs Nanocrystals with Size-Tunable near-Infrared Emission: Observation of Post-Synthesis Self-Narrowing of the Particle Size Distribution, *Adv. Mater.* 15, 1844-1849 (2003).

71. Z. Ning, O. Voznyy, J. Pan, S. Hoogland, V. Adinolfi, J. Xu, M. Li, A. R. Kirmani, J.-P. Sun, J. Minor, *et al.*, Air-Stable N-Type Colloidal Quantum Dot Solids, *Nat. Mater.* 13, 822-828 (2014).

72. J. Lynch, M. Kotiuga, V. V. T. Doan-Nguyen, W. L. Queen, J. D. Forster, R. A. Schlitz, C. B. Murray, J. B. Neaton, M. L. Chabinyc and J. J. Urban, Ligand Coupling Symmetry Correlates with Thermopower Enhancement in Small-Molecule/Nanocrystal Hybrid Materials, *ACS Nano* 8, 10528-10536 (2014).

73. J. M. Luther, M. Law, Q. Song, C. L. Perkins, M. C. Beard and A. J. Nozik, Structural, Optical, and Electrical Properties of Self-Assembled Films of Pbse Nanocrystals Treated with 1,2-Ethanedithiol, *ACS Nano* 2, 271-280 (2008).

74. M. D. Losego, M. E. Grady, N. R. Sottos, D. G. Cahill and P. V. Braun, Effects of Chemical Bonding on Heat Transport across Interfaces., *Nat. Mater.* 11, 502-506 (2012).

75. P. J. O'Brien, S. Shenogin, J. Liu, P. K. Chow, D. Laurencin, P. H. Mutin, M. Yamaguchi, P. Keblinski and G. Ramanath, Bonding-Induced Thermal Conductance Enhancement at Inorganic Heterointerfaces Using nanomolecular Monolayers, *Nat. Mater.* 12, 118-122 (2013).

76. J. C. Love, L. A. Estroff, J. K. Kriebel, R. G. Nuzzo and G. M. Whitesides, Self-Assembled Monolayers of Thiolates on Metals as a Form of Nanotechnology, *Chem. Rev.* 105, 1103-1170 (2005).

77. S.-M. Lee, Y.-W. Jun, S.-N. Cho and J. Cheon, Single-Crystalline Star-Shaped Nanocrystals and Their Evolution: Programming the Geometry of Nano-Building Blocks, *J. Am. Chem. Soc.* 124, 11244-11245 (2002).

78. *Handbook of Thermal Conductivity*, edited by L. Y. Carl (Gulf Professional Publishing, 1995), Vol. Volume 3, pp. 1-363.

79. J. M. Skelton, S. C. Parker, A. Togo, I. Tanaka and A. Walsh, Thermal Physics of the Lead Chalcogenides Pbs, Pbse, and Pbte from First Principles, *Phys. Rev. B* 89, 205203 (2014).

80. G. I. Koleilat, L. Levina, H. Shukla, S. H. Myrskog, S. Hinds, A. G. Pattantyus-Abraham and E. H. Sargent, Efficient, Stable Infrared Photovoltaics Based on Solution-Cast Colloidal Quantum Dots, *ACS Nano* 2, 833-840 (2008).

81. S. W. Joo, S. W. Han and K. Kim, Multilayer Formation of 1,2-Ethanedithiol on Gold: Surface-Enhanced Raman Scattering and Ellipsometry Study, *Langmuir* 16, 5391-5396 (2000).

82. D. Qu, B.-C. Kim, C.-W. J. Lee and K. Uosaki, 1, N-Alkanedithiol (N= 2, 4, 6, 8, 10) Self-Assembled Monolayers on Au (111): Electrochemical and Theoretical Approach, *Bull. Korean Chem. Soc.* 30, 2549-2554 (2009).

83. D. Hasselman and L. F. Johnson, Effective Thermal Conductivity of Composites with Interfacial Thermal Barrier Resistance, *J. Compos. Mater.* 21, 508-515 (1987).

84. Z. Wang, J. A. Carter, A. Lagutchev, Y. K. Koh, N.-H. Seong, D. G. Cahill and D. D. Dlott, Ultrafast Flash Thermal Conductance of Molecular Chains, *Science* 317, 787-790 (2007).

85. S. Shen, A. Henry, J. Tong, R. Zheng and G. Chen, Polyethylene Nanofibres with Very High Thermal Conductivities, *Nat. Nanotechnol.* 5, 251-255 (2010).

86. O. Andersson, A. Soldatov and B. Sundqvist, Thermal Conductivity of C60 at Pressures up to 1 Gpa and Temperatures in the 50 to 300 K Range, *Phys. Rev. B* 54, 3093-3100 (1996).

87. A. M. Marconnett, N. Yamamoto, M. A. Panzer, B. L. Wardle and K. E. Goodson, Thermal Conduction in Aligned Carbon Nanotube-Polymer Nanocomposites with High Packing Density, *ACS Nano* 5, 4818-4825 (2011).

88. G.-H. Kim, D. Lee, A. Shanker, L. Shao, M. S. Kwon, D. Gidley, J. Kim and K. P. Pipe, High Thermal Conductivity in Amorphous Polymer Blends by Engineered Interchain Interactions, *Nat. Mater.* 14, 295-300 (2015).

89. D. Yu, C. Wang and P. Guyot-Sionnest, N-Type Conducting Cdse Nanocrystal Solids, *Science* 300, 1277-1280 (2003).

90. K. H. Müller, G. Wei, B. Raguse and J. Myers, Three-Dimensional Percolation Effect on Electrical Conductivity in Films of Metal Nanoparticles Linked by Organic Molecules, *Phys. Rev. B* 68, 155407 (2003).

91. S.-M. Lee and D. G. Cahill, Heat Transport in Thin Dielectric Films, *J. Appl. Phys.* 81, 2590-2595 (1997).

92. N. C. Anderson, M. P. Hendricks, J. J. Choi and J. S. Owen, Ligand Exchange and the Stoichiometry of Metal Chalcogenide Nanocrystals: Spectroscopic Observation of Facile Metal-Carboxylate Displacement and Binding, *J. Am. Chem. Soc.* 135, 18536-18548 (2013).

93. I. Hadar, T. Abir, S. Halivni, A. Faust and U. Banin, Size-Dependent Ligand Layer Dynamics in Semiconductor Nanocrystals Probed by Anisotropy Measurements, *Angew. Chem., Int. Ed.* 54, 12463-12467 (2015).

94. Y. Xia, Y. Xiong, B. Lim and S. E. Skrabalak, Shape-Controlled Synthesis of Metal Nanocrystals: Simple Chemistry Meets Complex Physics?, *Angew. Chem., Int. Ed.* 48, 60-103 (2009).

95. M. V. Kovalenko, L. Manna, A. Cabot, Z. Hens, D. V. Talapin, C. R. Kagan, V. I. Klimov, A. L. Rogach, P. Reiss, D. J. Milliron, *et al.*, Prospects of Nanoscience with Nanocrystals, *ACS Nano* 9, 1012-1057 (2015).

96. P. Buffat and J. P. Borel, Size Effect on Melting Temperature of Gold Particles., *Phys. Rev. A* 13, 2287-2298 (1976).

97. G. L. Allen, R. A. Bayles, W. W. Gile and W. A. Jesser, Small Particle Melting of Pure Metals, *Thin Solid Films* 144, 297-308 (1986).

98. A. N. Goldstein, C. M. Echer and A. P. Alivisatos, Melting in Semiconductor Nanocrystals., *Science* 256, 1425-1427 (1992).

99. S. L. Lai, J. Y. Guo, V. Petrova, G. Ramanath and L. H. Allen, Size-Dependent Melting Properties of Small Tin Particles: Nanocalorimetric Measurements., *Phys. Rev. Lett.* 77, 99-102 (1996).

100. S. L. Lai, J. R. A. Carlsson and L. H. Allen, Melting Point Depression of Al Clusters Generated During the Early Stages of Film Growth: Nanocalorimetry Measurements, *Appl. Phys. Lett.* 72, 1098-1100 (1998).

101. M. Zhang, M. Y. Efremov, F. Schiettekatte, E. A. Olson, A. T. Kwan, S. L. Lai, T. Wisleder, J. E. Greene and L. H. Allen, Size-Dependent Melting Point Depression of Nanostructures: Nanocalorimetric Measurements, *Phys. Rev. B* 62, 10548-10557 (2000).

102. E. A. Olson, M. Y. Efremov, M. Zhang, Z. Zhang and L. H. Allen, Size-Dependent Melting of Bi Nanoparticles, *J. Appl. Phys.* 97, 034304 (2005).

103. J. Hu, Y. Hong, C. Muratore, M. Su and A. A. Voevodin, *In-Situ* Transmission Electron Microscopy of Solid-Liquid Phase Transition of Silica Encapsulated Bismuth Nanoparticles., *Nanoscale* 3, 3700-3704 (2011).

104. R. Kofman, P. Cheyssac, A. Aouaj, Y. Lereah, G. Deutscher, T. Ben-David, J. Penisson and A. Bourret, Surface Melting Enhanced by Curvature Effects, *Sur. Sci.* 303, 231-246 (1994).

105. K. Dick, T. Dhanasekaran, Z. Y. Zhang and D. Meisel, Size-Dependent Melting of Silica-Encapsulated Gold Nanoparticles, *J. Am. Chem. Soc.* 124, 2312-2317 (2002).

106. C. Y. Tang, Y. M. Sung and J. Lee, Nonlinear Size-Dependent Melting of the Silica-Encapsulated Silver Nanoparticles., *Appl. Phys. Lett.* 100, 201903 (2012).

107. Y. H. Jo, I. Jung, C. S. Choi, I. Kim and H. M. Lee, Synthesis and Characterization of Low Temperature Sn Nanoparticles for the Fabrication of Highly Conductive Ink, *Nanotechnology* 22, 225701 (2011).

108. H. Jiang, K.-s. Moon, H. Dong, F. Hua and C. P. Wong, Size-Dependent Melting Properties of Tin Nanoparticles, *Chem. Phys. Lett.* 429, 492-496 (2006).

109. K. Kravchyk, L. Protesescu, M. I. Bodnarchuk, F. Krumeich, M. Yarema, M. Walter, C. Guntlin and M. V. Kovalenko, Monodisperse and Inorganically Capped Sn and Sn/Sno_2 Nanocrystals for High-Performance Li-Ion Battery Anodes, *J. Am. Chem. Soc.* 135, 4199-4202 (2013).

110. M. Yarema, M. V. Kovalenko, G. Hesser, D. V. Talapin and W. Heiss, Highly Monodisperse Bismuth Nanoparticles and Their Three-Dimensional Superlattices., *J. Am. Chem. Soc.* 132, 15158-15159 (2010).

111. M. Yarema, S. Pichler, D. Kriegner, J. Stangl, O. Yarema, R. Kirchschlager, S. Tollabimazraehno, M. Humer, D. Häringer, M. Kohl, *et al.*, From Highly Monodisperse Indium and Indium Tin Colloidal Nanocrystals to Self-Assembled Indium Tin Oxide Nanoelectrodes, *ACS Nano* 6, 4113-4121 (2012).

112. M. Yarema, R. Caputo and M. V. Kovalenko, Precision Synthesis of Colloidal Inorganic Nanocrystals Using Metal and Metalloid Amides, *Nanoscale* 5, 8398-8410 (2013).

113. L. Gråbaek, J. Bohr, E. Johnson, A. Johansen, L. Sarholt-Kristensen and H. H. Andersen, Superheating and Supercooling of Lead Precipitates in Aluminum, *Phys. Rev. Lett.* 64, 934-937 (1990).

114. J. Zhong, L. H. Zhang, Z. H. Jin, M. L. Sui and K. Lu, Superheating of Ag Nanoparticles Embedded in Ni Matrix, *Acta Mater.* 49, 2897-2904 (2001).

115. F. G. Shi, Size-Dependent Thermal Vibrations and Melting in Nanocrystals, *J. Mater. Res.* 9, 1307-1313 (1994).

116. F. A. Lindemann, The Calculation of Molecular Natural Frequencies, *Phys. Z.* 11, 609-612 (1910).

117. J. Sun and S. L. Simon, The Melting Behavior of Aluminum Nanoparticles, *Thermochim. Acta* 463, 32-40 (2007).

118. Q. Jiang and F. G. Shi, Entropy for Solid–Liquid Transition in Nanocrystals, *Mater. Lett.* 37, 79-82 (1998).

119. M. Attarian Shandiz and A. Safaei, Melting Entropy and Enthalpy of Metallic Nanoparticles, *Mater. Lett.* 62, 3954-3956 (2008).

120. J. W. M. Frenken, P. M. J. Marée and J. F. van der Veen, Observation of Surface-Initiated Melting, *Phys. Rev. B* 34, 7506-7516 (1986).

121. A. W. D. van der Gon, R. J. Smith, J. M. Gay, D. J. O'Connor and J. F. van der Veen, Melting of Al Surfaces, *Sur. Sci.* 227, 143-149 (1990).

122. B. Pluis, T. N. Taylor, D. Frenkel and J. F. van der Veen, Role of Long-Range Interactions in the Melting of a Metallic Surface, *Phys. Rev. B* 40, 1353-1356 (1989).

123. Y. Lereah, G. Deutscher, P. Cheyssac and R. Kofman, A Direct Observation of Low-Dimensional Effects on Melting of Small Lead Particles, *Europhys. Lett.* 12, 709 (1990).

124. V. I. Levitas and K. Samani, Size and Mechanics Effects in Surface-Induced Melting of Nanoparticles, *Nat. Commun.* 2, 284 (2011).

125. D. A. Porter, K. E. Easterling and M. Sherif, *Phase Transformations in Metals and Alloys*. (CRC press, 2011).

126. D. Turnbull and R. E. Cech, Microscopic Observation of the Solidification of Small Metal Droplets, *J. Appl. Phys.* 21, 804-810 (1950).

127. W. H. Hofmeister, M. B. Robinson and R. J. Bayuzick, Undercooling of Pure Metals in a Containerless, Microgravity Environment, *Appl. Phys. Lett.* 49, 1342-1344 (1986).

128. Y. Shao and F. Spaepen, Undercooling of Bulk Liquid Silicon in an Oxide Flux, *J. Appl. Phys.* 79, 2981-2985 (1996).

129. H. B. Singh and A. Holz, Stability Limit of Supercooled Liquids, *Solid State Commun.* 45, 985-988 (1983).

130. G. Parravicini, A. Stella, P. Ghigna, G. Spinolo, A. Migliori, F. DAcapito and R. Kofman, Extreme Undercooling (Down to 90 K) of Liquid Metal Nanoparticles, *Appl. Phys. Lett.* 89, 033123 (2006).

131. S. C. Erwin, L. Zu, M. I. Haftel, A. L. Efros, T. A. Kennedy and D. J. Norris, Doping Semiconductor Nanocrystals, *Nature* 436, 91-94 (2005).

132. R. W. Cahn, Melting and the Surface, *Nature* 323, 668-669 (1986).

133. J. W. M. Frenken and J. F. Vanderveen, Observation of Surface Melting, *Physical Review Letters* 54, 134-137 (1985).

134. J. W. M. Frenken, P. M. J. Maree and J. F. Vanderveen, Observation of Surface-Initiated Melting, *Physical Review B* 34, 7506-7516 (1986).

135. R. Kofman, P. Cheyssac, A. Aouaj, Y. Lereah, G. Deutscher, T. Bendavid, J. M. Penisson and A. Bourret, Surface Melting Enhanced by Curvature Effects, *Surface Science* 303, 231-246 (1994).

136. L. H. Liang, J. C. Li and Q. Jiang, Size-Dependent Melting Depression and Lattice Contraction of Bi Nanocrystals, *Physica B* 334, 49-53 (2003).

137. H. M. Lu, P. Y. Li, Z. H. Cao and X. K. Meng, Size-, Shape-, and Dimensionality-Dependent Melting Temperatures of Nanocrystals, *J. Phys. Chem. C* 113, 7598-7602 (2009).

138. A. N. Goldstein, C. M. Echer and A. P. Alivisatos, Melting in Semiconductor Nanocrystals, *Science* 256, 1425-1427 (1992).

139. E. A. Olson, M. Y. Efremov, M. Zhang, Z. Zhang and L. H. Allen, Size-Dependent Melting of Bi Nanoparticles, *J. Appl. Phys.* 97, 034304 (2005).

140. C. J. Rossouw and S. E. Donnelly, Superheating of Small Solid-Argon Bubbles in Aluminum, *Phys. Rev. Lett.* 55, 2960-2963 (1985).

141. N. B. Thoft, J. Bohr, B. Buras, E. Johnson, A. Johansen, H. H. Andersen and L. Sarholtkristensen, Melting and Solidification of Bismuth Inclusions in Aluminum, *Journal of Physics D-Applied Physics* 28, 539-548 (1995).

142. R. Goswami and K. Chattopadhyay, Depression of Melting Point of Multidomained Bismuth in Aluminum Based Metallic Glass Nanocomposites, *Applied Physics Letters* 69, 910-912 (1996).

143. Q. Xu, I. D. Sharp, C. W. Yuan, D. O. Yi, C. Y. Liao, A. M. Glaeser, A. M. Minor, J. W. Beeman, M. C. Ridgway, P. Kluth, *et al.*, Large Melting-Point Hysteresis of Ge Nanocrystals Embedded in Sio2, *Physical Review Letters* 97, 155701 (2006).

144. Q. S. Mei, S. C. Wang, H. T. Cong, Z. H. Jin and K. Lu, Determination of Pressure Effect on the Melting Point Elevation of Al Nanoparticles Encapsulated in Al2o3 without Epitaxial Interface, *Physical Review B* 70, 125421 (2004).

145. F. Banhart, E. Hernandez and M. Terrones, Extreme Superheating and Supercooling of Encapsulated Metals in Fullerenelike Shells, *Physical Review Letters* 90, 185502 (2003).

146. J. Mu, Z. W. Zhu, H. F. Zhang, H. M. Fu, A. M. Wang, H. Li and Z. Q. Hu, Size Dependent Melting Behaviors of Nanocrystalline in Particles Embedded in Amorphous Matrix., *J. Appl. Phys.* 111, 043515 (2012).

147. M. A. Meitl, T. M. Dellinger and P. V. Braun, Bismuth-Ceramic Nanocomposites with Unusual Thermal Stability *Via* High-Energy Ball Milling., *Adv. Funct. Mater.* 13, 795-799 (2003).

148. R. Goswami and K. Chattopadhyay, Melting of Bi Nanoparticles Embedded in a Zn Matrix, *Acta Mater.* 52, 5503-5510 (2004).

149. E. Haro-Poniatowski, M. Jimenez de Castro, J. M. Fernandez Navarro, J. F. Morhange and C. Ricolleau, Melting and Solidification of Bi Nanoparticles in a Germanate Glass, *Nanotechnology* 18, 315703 (2007).

150. J. Park, J. Joo, S. G. Kwon, Y. Jang and T. Hyeon, Synthesis of Monodisperse Spherical Nanocrystals, *Angewandte Chemie-International Edition* 46, 4630-4660 (2007).

151. A. R. Tao, S. Habas and P. D. Yang, Shape Control of Colloidal Metal Nanocrystals, *Small* 4, 310-325 (2008).

152. Y. N. Xia, Y. J. Xiong, B. Lim and S. E. Skrabalak, Shape-Controlled Synthesis of Metal Nanocrystals: Simple Chemistry Meets Complex Physics?, *Angewandte Chemie-International Edition* 48, 60-103 (2009).

153. M. Yarema, M. V. Kovalenko, G. Hesser, D. V. Talapin and W. Heiss, Highly Monodisperse Bismuth Nanoparticles and Their Three-Dimensional Superlattices, *J. Am. Chem. Soc.* 132, 15158-15159 (2010).

154. C. Tang, Y.-M. Sung and J. Lee, Nonlinear Size-Dependent Melting of the Silica-Encapsulated Silver Nanoparticles, *Applied Physics Letters* 100, 201903 (2012).

155. R. Velraj, R. V. Seeniraj, B. Hafner, C. Faber and K. Schwarzer, Heat Transfer Enhancement in a Latent Heat Storage System, *Sol. Energy* 65, 171-180 (1999).

156. D. C. Hyun, N. S. Levinson, U. Jeong and Y. Xia, Emerging Applications of Phase-Change Materials (Pcms): Teaching an Old Dog New Tricks., *Angew. Chem., Int. Ed.* 53, 3780-3795 (2014).

157. C. Liu, F. Li, L. P. Ma and H. M. Cheng, Advanced Materials for Energy Storage., *Adv. Mater.* 22, E28-E62 (2010).

158. A. Sharma, V. V. Tyagi, C. R. Chen and D. Buddhi, Review on Thermal Energy Storage with Phase Change Materials and Applications., *Renewable Sustainable Energy Rev.* 13, 318-345 (2009).

159. M. Kenisarin and K. Mahkamov, Solar Energy Storage Using Phase Change Materials., *Renewable Sustainable Energy Rev.* 11, 1913-1965 (2007).

160. A. Pasupathy, R. Velraj and R. V. Seeniraj, Phase Change Material-Based Building Architecture for Thermal Management in Residential and Commercial Establishments., *Renewable Sustainable Energy Rev.* 12, 39-64 (2008).

161. S. Krishnan and S. V. Garimella, Thermal Management of Transient Power Spikes in Electronics - Phase Change Energy Storage or Copper Heat Sinks?, *J. Electron. Packag.* 126, 308-316 (2004).

162. R. Tamme, T. Bauer, J. Buschle, D. Laing, H. Müller-Steinhagen and W.-D. Steinmann, Latent Heat Storage above 120°C for Applications in the Industrial Process Heat Sector and Solar Power Generation., *Int. J. Energy Res.* 32, 264-271 (2008).

163. T. J. Lu, Thermal Management of High Power Electronics with Phase Change Cooling., *Int. J. Heat Mass Transfer* 43, 2245-2256 (2000).

164. J. Stekli, L. Irwin and R. Pitchumani, Technical Challenges and Opportunities for Concentrating Solar Power with Thermal Energy Storage., *J. Therm. Sci. Eng. Appl.* 5, 021011-021011 (2013).

165. M. M. Kenisarin, High-Temperature Phase Change Materials for Thermal Energy Storage., *Renewable Sustainable Energy Rev.* 14, 955-970 (2010).

166. S. Flueckiger, Z. Yang and S. V. Garimella, An Integrated Thermal and Mechanical Investigation of Molten-Salt Thermocline Energy Storage., *Appl. Energy* 88, 2098-2105 (2011).

167. H. Ji, D. P. Sellan, M. T. Pettes, X. Kong, J. Ji, L. Shi and R. S. Ruoff, Enhanced Thermal Conductivity of Phase Change Materials with Ultrathin-Graphite Foams for Thermal Energy Storage., *Energy Environ. Sci.* 7, 1185-1192 (2014).

168. S. N. Schiffres, S. Harish, S. Maruyama, J. Shiomi and J. A. Malen, Tunable Electrical and Thermal Transport in Ice-Templated Multi Layer Graphene Nanocomposites through Freezing Rate Control., *ACS Nano* 7, 11183-11189 (2013).

169. B. Zalba, J. M. Marin, L. F. Cabeza and H. Mehling, Review on Thermal Energy Storage with Phase Change: Materials, Heat Transfer Analysis and Applications., *Appl. Therm. Eng.* 23, 251-283 (2003).

170. M. Li, A Nano-Graphite/Paraffin Phase Change Material with High Thermal Conductivity., *Appl. Energy* 106, 25-30 (2013).

171. R. Parameshwaran, R. Jayavel and S. Kalaiselvam, Study on Thermal Properties of Organic Ester Phase-Change Material Embedded with Silver Nanoparticles., *J. Therm. Anal. Calorim.* 114, 845-858 (2013).

172. L. Chen, R. Zou, W. Xia, Z. Liu, Y. Shang, J. Zhu, Y. Wang, J. Lin, D. Xia and A. Cao, Electro and Photodriven Phase Change Composites Based on Wax-Infiltrated Carbon Nanotube Sponges., *ACS Nano* 6, 10884-10892 (2012).

173. H. T. Cui, Experimental Investigation on the Heat Charging Process by Paraffin Filled with High Porosity Copper Foam., *Appl. Therm. Eng.* 39, 26-28 (2012).

174. K. Lafdi, O. Mesalhy and A. Elgafy, Graphite Foams Infiltrated with Phase Change Materials as Alternative Materials for Space and Terrestrial Thermal Energy Storage Applications., *Carbon* 46, 159-168 (2008).

175. C. Y. Zhao and Z. G. Wu, Heat Transfer Enhancement of High Temperature Thermal Energy Storage Using Metal Foams and Expanded Graphite., *Sol. Energy Mater. Sol. Cells* 95, 636-643 (2011).

176. P. Pawlow, The Dependency of the Melting Point on the Surface Energy of a Solid Body. (Supplement), *Z. Phys. Chem.* 65, 545-548 (1909).

177. P. R. Couchman and W. A. Jesser, Thermodynamic Theory of Size Dependence of Melting Temperature in Metals., *Nature* 269, 481-483 (1977).

178. L. H. Liang, J. C. Li and Q. Jiang, Size-Dependent Melting Depression and Lattice Contraction of Bi Nanocrystals., *Phys. B* 334, 49-53 (2003).

179. Q. Xu, I. D. Sharp, C. W. Yuan, D. O. Yi, C. Y. Liao, A. M. Glaeser, A. M. Minor, J. W. Beeman, M. C. Ridgway, P. Kluth, *et al.*, Large Melting-Point Hysteresis of Ge Nanocrystals Embedded in Sio_2., *Phys. Rev. Lett.* 97, 155701 (2006).

180. N. D. M. Neil W. Ashcroft, *Solid State Physics.* (New York: Holt, Rinehart and Winston 1976). pp. 33-53.

181. E. Dujardin, C. Peet, G. Stubbs, J. N. Culver and S. Mann, Organization of Metallic Nanoparticles Using Tobacco Mosaic Virus Templates., *Nano Lett.* 3, 413-417 (2003).

182. A. Kumar, P. K. Vemula, P. M. Ajayan and G. John, Silver-Nanoparticle-Embedded Antimicrobial Paints Based on Vegetable Oil., *Nat. Mater.* 7, 236-241 (2008).

183. C. B. Murray, D. J. Norris and M. G. Bawendi, Synthesis and Characterization of Nearly Monodisperse Cde(E=S, Se, Te) Semiconductor Nanocrystallites., *J. Am. Chem. Soc.* 115, 8706-8715 (1993).

184. T. Hanrath, D. Veldman, J. J. Choi, C. G. Christova, M. M. Wienk and R. A. J. Janssen, Pbse Nanocrystal Network Formation During Pyridine Ligand Displacement., *ACS Applied Materials & Interfaces* 1, 244-250 (2009).

185. *Binary Alloy Phase Diagrams 2.2.* (Materials Park, Ohio: The Materials Information Society, 1996;).

186. L. Gråbaek, J. Bohr, E. Johnson, A. Johansen, L. Sarholt-Kristensen and H. Andersen, Superheating and Supercooling of Lead Precipitates in Aluminum., *Physical Review Letters* 64, 934-937 (1990).

187. J. Zhong, L. H. Zhang, Z. H. Jin, M. L. Sui and K. Lu, Superheating of Ag Nanoparticles Embedded in Ni Matrix., *Acta Mater.* 49, 2897-2904 (2001).

188. B. Poudel, Q. Hao, Y. Ma, Y. Lan, A. Minnich, B. Yu, X. Yan, D. Wang, A. Muto, D. Vashaee, *et al.*, High-Thermoelectric Performance of Nanostructured Bismuth Antimony Telluride Bulk Alloys., *Science* 320, 634-638 (2008).

189. E. Haro-Poniatowski, M. Jimenez de Castro, J. M. Fernandez Navarro, J. F. Morhange and C. Ricolleau, Melting and Solidification of Bi Nanoparticles in a Germanate Glass., *Nanotechnology* 18 (2007).

190. I. D. Sharp, D. O. Yi, Q. Xu, C. Y. Liao, J. W. Beeman, Z. Liliental-Weber, K. M. Yu, D. N. Zakharov, J. W. Ager, D. C. Chrzan, *et al.*, Mechanism of Stress Relaxation in Ge Nanocrystals Embedded in Sio2., *Appl. Phys. Lett.* 86, 063107 (2005).

191. M. Bieligmeyer, S. M. Taheri, I. German, C. Boisson, C. Probst, W. Milius, V. Altstadt, J. Breu, H. W. Schmidt, F. D'Agosto, *et al.*, Completely Miscible Polyethylene Nanocomposites., *J. Am. Chem. Soc.* 134, 18157-18160 (2012).

192. K.-J. Jeon, H. R. Moon, A. M. Ruminski, B. Jiang, C. Kisielowski, R. Bardhan and J. J. Urban, Air-Stable Magnesium Nanocomposites Provide Rapid and High-Capacity Hydrogen Storage without Using Heavy-Metal Catalysts., *Nat. Mater.* 10, 286-290 (2011).

193. H. Choi, J. P. Lee, S. J. Ko, J. W. Jung, H. Park, S. Yoo, O. Park, J. R. Jeong, S. Park and J. Y. Kim, Multipositional Silica-Coated Silver Nanoparticles for High-Performance Polymer Solar Cells., *Nano Lett.* 13, 2204-2208 (2013).

194. R. Tangirala, J. L. Baker, A. P. Alivisatos and D. J. Milliron, Modular Inorganic Nanocomposites by Conversion of Nanocrystal Superlattices., *Angew. Chem., Int. Ed.* 49, 2878-2882 (2010).

195. M. V. Kovalenko, B. Spokoyny, J.-S. Lee, M. Scheele, A. Weber, S. Perera, D. Landry and D. V. Talapin, Semiconductor Nanocrystals Functionalized with Antimony Telluride Zintl Ions for Nanostructured Thermoelectrics., *J. Am. Chem. Soc.* 132, 6686-6695 (2010).

196. A. K. Galwey, D. Jamieson and M. E. Brown, Thermal Decomposition of Three Crystalline Modifications of Anhydrous Copper(Ii) Formate., *J. Phys. Chem.* 78, 2664-2670 (1974).

197. A. Gupta and R. Jagannathan, Laser Writing of Copper Lines from Metalorganic Films., *Appl. Phys. Lett.* 51, 2254-2256 (1987).

198. E. K. Fields and S. Meyerson, Thermal and Photochemical Decomposition of Silver Carboxylates., *J. Org. Chem.* 41, 916-920 (1976).

199. V. Logvinenko, O. Polunina, Y. Mikhailov, K. Mikhailov and B. Bokhonov, Study of Thermal Decomposition of Silver Acetate., *J. Therm. Anal. Calorim.* 90, 813-816 (2007).

200. A. A. Bessonov, N. B. Morozova, P. P. Semyannikov, S. V. Trubin, N. V. Gelfond and I. K. Igumenov, Thermal Behaviour of Dimethylgold(Iii) Carboxylates., *J. Therm. Anal. Calorim.* 92, 751-755 (2008).

201. P. K. Gallagher and M. E. Gross, The Thermal Decomposition of Palladium Acetate., *J. Therm. Anal.* 31, 1231-1241 (1986).

202. L. M. Fillman and S. C. Tang, Thermal Decomposition of Metal-Carbonyls - a Thermogravimetry Mass-Spectrometry Study., *Thermochim. Acta* 75, 71-84 (1984).

203. Y. Hong, W. Wu, J. Hu, M. Zhang, A. A. Voevodin, L. Chow and M. Su, Controlling Supercooling of Encapsulated Phase Change Nanoparticles for Enhanced Heat Transfer., *Chem. Phys. Lett.* 504, 180-184 (2011).

204. S. Himran, A. Suwono and G. A. Mansoori, Characterization of Alkanes and Paraffin Waxes for Application as Phase-Change Energy Storage Medium., *Energy Sources* 16, 117-128 (1994).

205. A. Hasan and A. A. Sayigh, Some Fatty Acids as Phase-Change Thermal Energy Storage Materials., *Renewable Energy* 4, 69-76 (1994).

206. G. S. Kumar, G. Prasad and R. O. Pohl, Experimental Determinations of the Lorenz Number. , *J. Mater. Sci.* 28, 4261-4272 (1993).

207. A. Sommerfeld, The Theory of Electrons of Metals., *Naturwissenschaften* 16, 374-381 (1928).

208. H. Yang, J.-H. Bahk, T. Day, A. M. S. Mohammed, B. Min, G. J. Snyder, A. Shakouri and Y. Wu, Composition Modulation of Ag2te Nanowires for Tunable Electrical and Thermal Properties., *Nano Lett.* 14, 5398-5404 (2014).

209. L.-D. Zhao, S.-H. Lo, J. He, H. Li, K. Biswas, J. Androulakis, C.-I. Wu, T. P. Hogan, D.-Y. Chung, V. P. Dravid, *et al.*, High Performance Thermoelectrics from Earth-Abundant Materials: Enhanced Figure of Merit in Pbs by Second Phase Nanostructures., *J. Am. Chem. Soc.* 133, 20476-20487 (2011).

210. R. Y. Wang, R. A. Segalman and A. Majumdar, Room Temperature Thermal Conductance of Alkanedithiol Self-Assembled Monolayers., *Appl. Phys. Lett.* 89, 173113 (2006).

211. B. C. Gundrum, D. G. Cahill and R. S. Averback, Thermal Conductance of Metal-Metal Interfaces., *Phys. Rev. B* 72, 245426 (2005).

212. A. Minnich and G. Chen, Modified Effective Medium Formulation for the Thermal Conductivity of Nanocomposites., *Appl. Phys. Lett.* 91, 073105 (2007).